MONTAN

UNIVERSITAT

LEOBEN

Chair of Materials Physics

Master's Thesis

Influence of microstructure on the R-curve behaviour and fracture toughness of tungsten

Daniel Ernst Firneis, BSc

May 2020

This work has been carried out within the framework of the EUROfusion Consortium and has received funding from the Euroatom Research and Training Programme 2014-2020 under grant agreement No 633053. The views and opinions expressed herein do not necessarily reflect those of the European Commission.

EIDESSTATTLICHE ERKLÄRUNG

Ich erkläre an Eides statt, dass ich diese Arbeit selbständig verfasst, andere als die angegebenen Quellen und Hilfsmittel nicht benutzt, und mich auch sonst keiner unerlaubten Hilfsmittel bedient habe.

Ich erkläre, dass ich die Richtlinien des Senats der Montanuniversität Leoben zu "Gute wissenschaftliche Praxis" gelesen, verstanden und befolgt habe.

Weiters erkläre ich, dass die elektronische und gedruckte Version der eingereichten wissenschaftlichen Abschlussarbeit formal und inhaltlich identisch sind.

Datum 25.05.2020

Unterschrift Verfasser/in
Daniel Ernst, Firneis

Danksagung

Mit diesen Seiten möchte Ich mich bei all den lieben Kollegen, meiner Familie und Freunden bedanken, die mich im Laufe meines etwas länger währenden Studiums der Werkstoffwissenschaften unterstützt haben und mir diese Diplomarbeit/Masterthesis überhaupt erst ermöglicht haben.

Mein besonderer Dank gilt Herrn Univ. Prof. Dr. Reinhard Pippan, der mir diese Diplomarbeit erst ermöglicht hat, der meinen konfusen Ideen und Erklärungen immer spontan ein Ohr geschenkt hat und mir mit gutem Rat und seinem unerschütterlichen Optimismus zur Seite gestanden hat. Jedes Gespräch mit Dir, lieber Reinhard, ist ein weiterer kleinerer oder manchmal sogar größerer Motivationsschub.

Danke Stefan, danke Toni, danke Peter für all die praktische Hilfe, eure Ideen und auch eure Einwände, danke für Unterstützung experimenteller Natur, aber insbesondere auch für die moralische Unterstützung. Danke Stefan, dass du mir immer geduldig zugehört hast, wenn wieder mal etwas nicht funktioniert hat und mir immer mit Rat und Tat und Gummibärchen zur Seite gestanden bist.

Thank you Vladica, for always believing in me in the hours of talks we had (mostly not work-related stuff), keeping me on track with my studies and helping me a tremendous lot with the sample preparation.

Danke Robin und Franz, für die meist richtige Interpretation meiner nicht immer richtigen Konstruktionszeichnungen. Danke für die Diskussionen und die Einwände an meinen nicht immer zu 100% durchdachten Ideen und die Tonnen an unterschiedlichen Proben und Probenhaltern, die Ihr mir die letzten Jahre hindurch immer wieder gefertigt habt.

Danke liebe Silke, für die viele Hilfe bei der Probenpräparation, die netten Gespräche und Serienempfehlungen.

Danke liebe Dani und liebe Sabine, dass ihr keine Fragen gestellt habt, wenn ich mal wieder Unmengen an Klebeband oder Ähnliches von Euch geholt habe, und danke für die lieben Gespräche. Deinen Beitrag zum ersten erfolgreichen R-Kurven Test werde ich nicht vergessen, Dani, die Schokocreme war wirklich lecker.

Danke an dich Jens, für deine ansteckende kindliche Neugier bei allem was Wolfram betrifft, deine freundliche Art und danke dem KIT für das zur Verfügung gestellte und in dieser Thesis getestete Probenmaterial.

Danke Mama, Papa, Claudia und Günther, Tante Heidi und Oma für Eure Geduld, Eure moralische und auch finanzielle Unterstützung und Euren Glauben an mich. Auch wenn Ihr nie so wirklich verstanden habt, was ich in Leoben Komisches mache, habt ihr immer alles getan, um mich zu unterstützen, selbst in den Momenten, in denen ich selbst nicht mehr geglaubt habe, fertig zu werden. Hab euch alle Lieb!

Danke Dir lieber Gerhard, für die ganze Zeit und Mühe, die du dir gemacht hast, um mir dabei zu helfen, dass diese Diplomarbeit lesbar ist und hoffentlich jeder Rechtschreibfehler entdeckt wurde. Danke Gundi, dass du mir den Gerhard geliehen hast.

Auch ein herzlicher Dank an meine Freunde, ohne die ich wohl nie so weit gekommen wäre, insbesondere bei jenen die ich in Leoben kennen gelernt habe. Ich hoffe sehr, dass unsere Freundschaft noch lange über Leoben hinaus hält. Ich meine insbesondere Euch, Christoph, Martin, Belinda, Franz, Mirijam, Kathi, Vladi, Stefan, Thomas und Kathi. Danke lieber Markus, dass du immer noch mein Freund bist, auch wenn die Frequenz, in der wir uns gesehen haben, mit dem Beginn meines Studiums stark abgenommen hat.

Danke an alle die an mich geglaubt haben.

Danke an alle die mir bei meiner Diplomarbeit geholfen haben, sei es jetzt durch neue Ideen, praktische Hilfe oder einfach nur durch ein angenehmes Gespräch.

Table of contents

Index of abbreviations and symbols used

Δa	crack extension
a, a_0	crack length, initial crack length
2λ	distance between the potential measurement leads
B	sample thickness
bcc	body-centred cubic
DBTT	ductile to brittle transition temperature
DCPM	direct current potential drop method
EBSD	electron backscatter diffraction
EDX	energy dispersive X-ray spectroscopy
f(a/W)	geometry factor for calculating K_q and K_{IC}
fcc	face-centred cubic
K_I	stress-intensity factor for mode I
K_{IC}	critical stress-intensity factor / fracture toughness
K_q	conditional fracture toughness
LEFM	linear elastic fracture mechanic
LIMI	light microscope
ND	normal direction
P	load applied on the sample
RD	rolling direction
RT	room temperature
SEM	scanning electron microscope
TD	transversal direction
U, U_0	actual potential, initial potential
ufg	ultra-fine grained
W	sample width / tungsten
W_{pl}	plastic deformation energy
γ	surface energy
σ	tensile stress applied

Kurzfassung

Im Rahmen dieser Arbeit wurden Wolframproben mit unterschiedlicher Mikrostruktur auf ihre Bruchzähigkeit getestet und, wo möglich, eine Risswiderstandskurve (R-Kurve) aufgenommen. Diese unterschiedlichen Mikrostrukturen wurden bei Plansee SE (Reutte, Österreich) durch unterschiedlich hohe Umformgrade und den daraus resultierenden unterschiedlichen Probendicken in der Form von Wolframblechen und –folien verwirklicht. Hierfür wurde bei Plansee ein Wolframbarren durch einen mehrstufigen thermomechanischen Walzprozess geschickt und bei den gewünschten Probendicken von 1 mm, 0.5 mm und 0.2 mm jeweils Probenmaterial entnommen. Durch dieses Vorgehen konnten etwaige Einflüsse von variierender chemischer Zusammensetzung auf die mechanischen Eigenschaften ausgeschlossen werden. Das in dieser Diplomarbeit ebenfalls untersuchte 0.1 mm Material wurde auf der gleichen Prozessroute hergestellt, stammte jedoch aus einer anderen Wolframcharge. Da die zur Verfügung stehende Menge an Probenmaterial stark limitiert war, wurden zum Zwecke eines breiteren Probenspektrums und für die ersten Vorversuche noch 2 mm dicke Proben aus einem in größeren Mengen am Erich-Schmid-Institut verfügbaren Wolframblech gefertigt. Die Mikrostruktur der in dieser Arbeit getesteten Materialien wurde mittels Elektronenrückstreubeugung (EBSD) analysiert. Je höher der Umformgrad und somit je dünner die Proben, desto kleiner erwies sich die Korngröße und desto ausgeprägter die Textur.

Für die Bruchzähigkeits- und R-Kurvenversuche wurde aus den zur Verfügung gestellten Materialien L-T Proben hergestellt und diese bei zwei unterschiedlichen Temperaturen getestet, nämlich bei Raumtemperatur (RT) und bei 200°C. Von jeder getesteten Probe wurde im Anschluss an die Bruchzähigkeitsversuche eine Aufnahme der Bruchflächen im Rasterelektronenmikroskop (SEM) erstellt. Bei RT war für die 2 mm Proben noch kein R-Kurvenverhalten feststellbar, bei 200 °C jedoch konnte bereits eine ausgeprägte R-Kurve aufgezeichnet werden. Mit Fortlaufen der Tests konnte bei RT mit abnehmender Probendicke eine Änderung des Bruchverhaltens festgestellt werden. Die 0.5 mm Probe zeigte bei RT und reduzierter Belastungsgeschwindigkeit bereits den Ansatz einer R-Kurve und damit einhergehend eine Veränderung im Bruchbild, nämlich einen Übergang von rein sprödem Bruch bei den zuvor untersuchten 2 mm Proben zu einem Mischbruch aus Delamination und

anschließendem Sprödbuch bei den nunmehr untersuchten 0.5 mm Proben. Dies lässt darauf schließen, dass sich die spröd-duktil-Übergangstemperatur (DBTT) von Wolfram (W), die bei den 2 mm Proben bei ca. 200°C lag, bei den 0.5 mm Proben in Richtung RT verschoben hat. Alle nachfolgend getesteten dünneren Proben von 0.2 mm und 0.1 mm zeigten bereits bei RT ein R-Kurvenverhalten und zumindest anteilig Delamination. Die gemessenen Bruchzähigkeitswerte aller bei RT getesteten Proben befanden sich im Bereich von 50 bis 60 MPa√m, mit Ausnahme der 2 mm Proben, bei denen sie deutlich darunter bei ca. 16 MPa√m lagen. Die Erhöhung der Testtemperatur auf 200 °C führte bei den dickeren Proben (2 mm bis 0.5 mm) zu einer Steigerung der gemessenen Bruchzähigkeitswerte auf 56 bis 70 MPa√m, bei den 0.2 mm und 0.1 mm Proben konnte keine solche Steigerung beobachtet werden.

Die größte Herausforderung dieser Arbeit lag darin Methoden zu entwickeln, die es überhaupt erst ermöglichen, Wolframproben mit so unterschiedlichen Dicken auf zumindest ähnliche Weise hinsichtlich Bruchzähigkeits- und R-Kurvenverhalten zu testen. Ob jetzt allein die feinere Mikrostruktur der Grund für die besseren bruchmechanischen Eigenschaften ist oder welchen Einfluss die abnehmende Probendicke hat (Stichwort: Probengrößeneffekt), bleibt noch ein Fall für weitere Diskussionen und Untersuchungen.

Abstract

Tungsten (W) samples with different microstructures were tested regarding their fracture toughness and R-curve behaviour. The different microstructures were obtained by increasing the degree of deformation resulting in a decrease of material thickness. To produce these samples in the company Plansee SE (Reutte, Austria) a W ingot was submitted to a thermomechanical rolling process, at appropriate stages of this process samples with the targeted thicknesses of 1 mm, 0.5 mm and 0.2 mm were taken. The advantage of this approach is that influences regarding the chemical composition on the mechanical properties can be excluded. The 0.1 mm material was produced in the same processing route, however from a different W ingot. In order to achieve comparison over a wider range of thickness of samples preliminary tests on a 2 mm material originating from resources of the Erich-Schmid Institute were performed.

The microstructure of the materials tested was analysed using electron backscatter diffraction (EBSD). As expected, the grain size of the samples decreased with decreasing sample thickness, and the texture became more pronounced. The fracture toughness was tested at room temperature (RT) and 200 °C, and after testing micrographs of the fracture surface of each sample was taken using a scanning electron microscope (SEM). The 2 mm samples did not exhibit an R-curve behaviour at RT, though pronounced R-curves could be recorded when performing the tests at 200°C. Further tests revealed a change in fracture behaviour at RT with decreasing sample thickness. The 0.5 mm sample tested at RT and with a slower loading rate was the very first sample showing a slight R-curve behaviour at RT. Fracture surfaces changed from pure brittle fracture at the 2 mm samples to some mixed fracture with delamination and brittle fracture for the 0.5 mm samples. This indicates that the ductile to brittle transition temperature (DBTT) shifted from about 200 °C to RT when sample thickness decreased from 2 mm to 0.5 mm. The thinner samples, i.e. 0.2 mm and 0.1 mm, showed an R-curve behaviour at RT already and brittle fracture mixed with delaminations. The fracture toughness at RT for all samples tested ranged between 50 to 60 MPa√m, except for the 2 mm samples, which had a fracture toughness of about 16 MPa√m. Increasing the testing temperature to 200 °C lead to an increase in fracture toughness for the thicker samples (2 mm, 1 mm, 0.5 mm) ranging between 56 to 70 MPa√m. For the thinner samples (0.2 mm and 0.1 mm) such an increase in fracture toughness was not observed.

The biggest challenge of this thesis was to develop methods to test samples of divergent thickness in a similar way. It is still up for discussion and further testing to verify whether the improved mechanical properties of the thinner materials tested in this thesis exclusively are a result of the improved microstructure, or whether there could be an influence of the sample thickness.

1. Introduction

In addition to the highest melting point of 3422 °C of all metals [1] tungsten (W) features several other outstanding properties. The good thermal conductivity, the high strength at elevated temperatures and the low thermal expansion coefficient qualify W for being a desired material for high temperature applications. However, the engineering usage of W is restricted due to two major drawbacks. The first drawback is the low corrosion resistance of W at temperatures higher than 400 °C [2], strictly conflicting with W to be used at high temperatures without protective coatings or in protective gas atmosphere. The second and even more problematic drawback is as follows: As any other metal with body-centred cubic lattice (bcc) W is inherently brittle below its ductile to brittle transition temperature (DBTT). For commercially used W the DBTT is above RT, essentially complicating W to be utilized as a structural material. Extensive research on tungsten single crystals has been carried out in the nineties with the phenomenological fracture behaviour now being understood relatively well [3]. The fracture behaviour of polycrystalline tungsten depends on many influences such as impurities, microstructure, production route and thermomechanical treatment, testing parameters like testing method, temperature, sample geometry and loading rate; facts making it very challenging to compare respective results achieved.

Research on polycrystalline W has been sparked by the idea of using W, based on its high melting point, and its excellent high temperature properties as well, as a plasma facing material in the upcoming fusion reactor ITER (International Thermonuclear Experimental Reactor) and DEMO (DEMOnstration Power Plant) [4,5]. Oodles of work and research have been invested in the last 20 years to learn more on the fracture mechanisms and fracture behaviour of polycrystalline W and to improve it.

Three different approaches to improve the mechanical properties of W emerged over the last few decades: alloying, improving the microstructure and production of composite materials (e.g. tungsten-fibre reinforced tungsten [6] or tungsten laminated composites [7]). Of these three approaches alloying is the one where most research has been carried out so far. The beneficial effect of rhenium (Re) alloying is well known for decades [8]. In a recent study conducted by Wurster et al. [9] the high temperature fracture behaviour on W-Re alloys has been investigated, showing that Re alloyed W even after recrystallization keeps its improved

fracture behaviour unlike pure W. The approach to improve the mechanical properties of W by means of refining its microstructure is the target of this thesis. Nikolić et al. [10] showed in their extensive work on ufg (ultra-fine grained) W foils that these foils do not behave brittle. Parts of this thesis presented were inspired by the work of Nikolič et al., and methods described in their publications are applied in this thesis as well. Bonk et al. [11,12] and Bonnekoh et al. [13] have carried out extensive research regarding the tensile strength, the microstructure and the fracture toughness of the materials tested in this thesis, too. Still left to be examined is the correlation between the microstructure and the fracture toughness of these materials and to reveal details on an R-curve potentially occurring due to the improved fracture behaviour of materials with refined microstructure, an issue being carried out within this thesis now. In case of materials showing an R-curve behaviour, the fracture toughness cannot be expressed by means of a single value anymore. Additionally to K_{IC}, the critical fracture toughness value of a sample tested, the R-curve behaviour of this sample must be examined and indicated in some detail, an issue this thesis presented starts with. The occurrence of an R-curve for any sample tested implies that the fracture toughness of this sample increases continuously with increasing crack extension. The goal of this thesis was to examine the fracture behaviour of W samples with reference to their particular microstructure and to record the R-curve occurring in case the sample actually featured such R-curve.

2. Basics

2.1. Fracture toughness and linear elastic fracture mechanics

The fracture toughness is defined as the resistance of a material against crack growth of a component or specimen which contains already a crack. If the dimensions are not sufficient the fracture toughness depends on the geometry of the sample tested. Due to this the fracture toughness is not a material constant, it is rather some value to describe the crack resistance of a material under defined testing parameters [14]. An easily comprehensible description of the basics of fracture mechanics can be found in the book of T.L. Anderson: Fracture Mechanics, Fundamentals and Applications [15]. Just below a short summary of the essential concepts of fracture mechanics is given, especially on the linear elastic fracture mechanics (LEFM). Any material fractures when enough stress is applied to it to break the atomic bonds. The theoretical strength of a material is determined by the strength of the bonding force between its atoms. Experiments on the fracture strength of materials revealed that the theoretical strength of brittle materials is higher by orders of magnitude than all values for the respective fracture strength ever received experimentally, a phenomenon being due to flaws in the material or plastic deformation. A material impossibly may fracture unless the stress at the atomic level exceeds the cohesive strength between the atoms, therefore the flaws must amplify the stress locally. By analysing elliptical holes in flat plates Inglis [16] in 1913 was the first scientist to find quantitative evidence for flaws like pores and cracks magnifying the local stress[1]. Due to this local stress concentration, crack initiation and crack growth preferably take place at flaws like pores, notches and imperfections. Important tasks of fracture mechanics are to investigate and examine the fracture behaviour of materials, to analyse how and why components or materials fail, to understand the underlying mechanisms of crack initiation and crack growth, and to find ways to improve the fracture properties of materials in order to improve the lifespan of particular components.

There are two approaches for considering the fracture toughness considering in the linear elastic fracture mechanics (LEFM). One of these approaches is based on the concepts of

[1] Local stress: The stress occurring locally within the material at the region of these flaws.

energy and conservation of energy. This approach referred to as the extended energy criterion was proposed by Griffith [17] in 1920 and further developed by Irwin in 1956 [18]. The extended energy criterion states that a crack extension may not take place until the available energy G (energy release rate) for crack growth is equal or higher than the resistance R (or in other terms the critical energy release rate G_c, respectively,) of the material [Eq. 2.1]. This resistance R includes the energy necessary for forming new surfaces γ, the plastic deformation energy W_{pl} necessary to move the plastic zone around the crack and other forms of energy dissipation during crack extension Δa [Eq. 2.2] (B is the thickness of the sample).

$$G \geq R \qquad \text{[Eq.2.1]}$$

$$G_c = R = \frac{1}{B} * \frac{d(W_{pl}+2\gamma)}{d(\Delta a)} \qquad \text{[Eq.2.2]}$$

For an infinite plate with a critical crack length a_c (above which unstable crack growth will occur), with Young's modulus E and with an external stress σ_f applied to the plate, the critical energy release rate is given by equation [Eq. 2.3]

$$G_c = \frac{\pi * \sigma_f * a_c}{E} \qquad \text{[Eq.2.3]}$$

The second approach to calculate the fracture toughness is the stress-intensity approach, used frequently in fracture mechanics and especially used widely in engineering applications. In this approach a single constant, the stress – intensity factor K_I, is used to describe the entire stress distribution in the vicinity of the crack tip in a linear elastic material. The index indicates one of three possibly ways of crack opening. Mode I refers to a crack tip opening under a stress normal to the crack plane, Mode II to opening in in-plane shear and Mode III to opening in out-of-plane shear. For most cases the fracture toughness of a material will be determined applying a normal stress, due to materials usually being most sensitive for crack propagation normal to the stress applied. A material critically fails if K_I exceeds the critical-stress intensity factor (or fracture toughness) K_{IC} (analogous to G reaching R within the energy concept of fracture mechanics). Equation 2.4 describes the value of the stress intensity factor K_I for a

through crack of length a in an infinite plate when loaded with a remote tensile stress σ. Equation 2.5 depicts K_I for realistic cases of linear elastic materials, where P is the load applied, B the sample thickness, W the sample width and f(a/W) a dimensionless factor which takes into account the way of sample loading and the geometry of the samples. The geometrical factor f(a/W) is determined by means of fracture toughness experiments or numerical simulations for a multitude of testing and sample configurations, correspondent descriptions and values can be found in fracture mechanics handbooks dedicated exclusively to that factor.

$$K_I = \sigma * \sqrt{\pi * a} \qquad \text{[Eq.2.4]}$$

$$K_I = \frac{P}{B*\sqrt{W}} * f\left(\frac{a}{W}\right) \qquad \text{[Eq.2.5]}$$

The description of the stress field in front of a crack, using only one simple constant K, provides an elegant solution for problems in fracture mechanics difficult to solve otherwise. The validity of the linear elastic fracture mechanic is limited by the size of the plastic zone and the predominant linear elastic behaviour of the sample. According to the ASTM E399 [19], the standard test method for linear-elastic plane-strain fracture toughness K_{IC} of metallic materials, a sample must comply with Eq. 2.6. in order to fulfil the preconditions for valid fracture toughness tests. If the sample geometry complies with Eq.2.6 (where σ_{ys} is the 0.2 % offset yield strength under test conditions identical to those of the fracture toughness tests) the plastic zone at the crack-tip assuredly is small compared to the crack size a , specimen thickness B and ligament (W-a), and the sample is tested in pure plane-strain dominated conditions.

$$a, B, W - a \geq 2.5 * \left(\frac{K_{IC}}{\sigma_{ys}}\right)^2 \qquad \text{[Eq.2.6]}$$

Considering the constraints on sample dimension implicated by the goal of this thesis to test samples of very small thickness, none of the samples tested for this thesis actually complies with Eq.2.6, therefore all fracture toughness results obtained in this thesis are not to be specified as fracture toughness K_{IC} but as conditional fracture toughness K_q.

2.2. Fracture mechanisms in metals

Every metal inevitably features some varying number of defects like inclusions, segregations, second phase particles, pores, micro cracks and crystal defects such as dislocations. There are two distinctive fracture mechanisms in metals, in both mechanism dislocations play an important role. Fracture in ductile metals is characterized by broad plastic deformation before and during the fracture process occurring. The ductile fracture mechanism can be segmented into three steps: nucleation, growth, and coalescence of voids that are initiated at segregations or inclusions (figure 2.1). If stress is applied to a ductile metal sufficiently strong to break the interfacial bonds between impurities - like e.g. inclusions - and the matrix, voids are formed. Dislocation pile-ups can be responsible for forming voids, too. Further stress increase leads to growth of these voids, local stress concentration within the material remaining between the voids and finally to coalescence of the voids, resulting in fracture of the material.

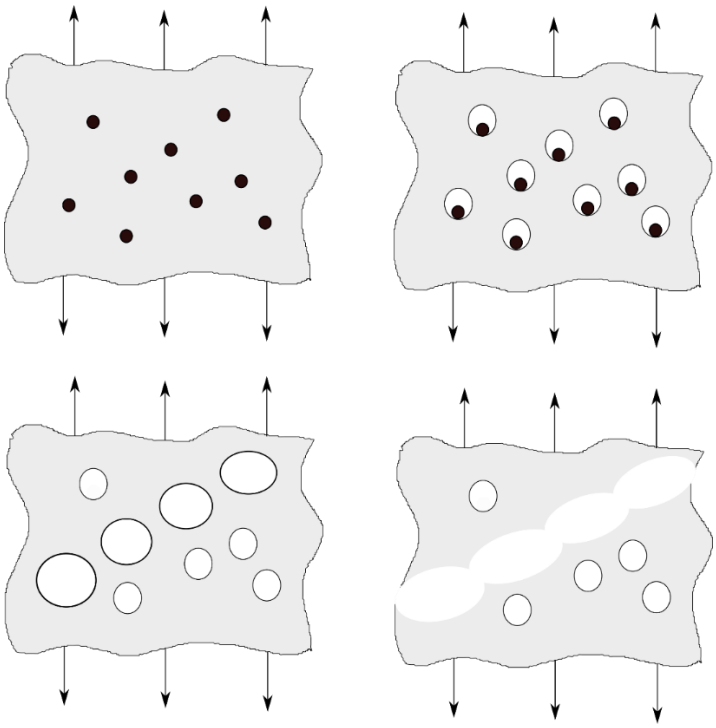

Figure 2.1: The three stages of fracture in a ductile metal. Top left: ductile metal with impurities before nucleation; Top right: nucleation of voids due to a stress applied sufficiently high enough to break the interfacial bonds between the matrix and the impurities; Bottom left: growth of the voids; Bottom right: coalescence of the voids.

Brittle fracture is characterized by little to no plastic deformation in the material before or during the fracture process. This results in little to no reaction time from fracture initiation to complete failure of the material or component, a phenomenon being the most important reason why brittle fracture is so dangerous. There are two main brittle fracture mechanisms in metals and alloys, namely intergranular and transgranular fracture (figure 2.2). Crack propagation always takes place along the path of least resistance through a material. Dislocation pile-ups cause high local stress concentrations which can lead to fracture along preferred lattice planes through grains, resulting in a fracture surface oriented into different directions depending on the orientation of the respective grain. This kind of fracture is referred to as a transgranular fracture. If the grain boundary strength is significantly weaker than the inherent strength of the grain, the fracture will take place along the grain boundaries, this being referred to as an intergranular fracture [20].

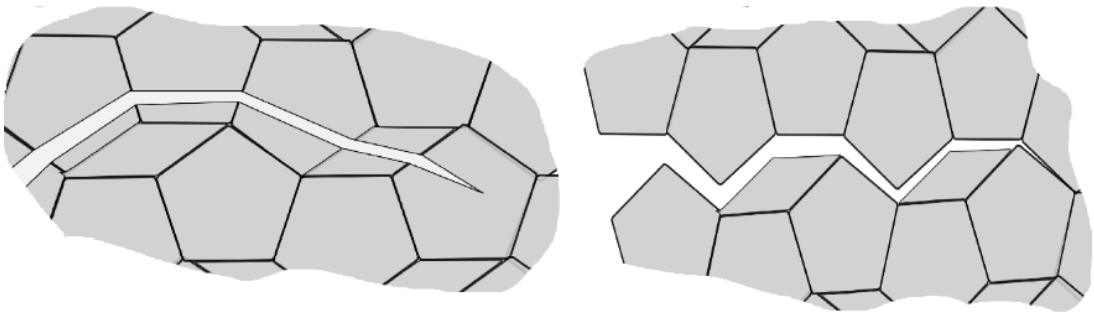

Figure 2.2: Schematic representation of transgranular fracture on the left-hand side and intergranular fracture on the right-hand side.

When discussing fracture mechanisms of metals one more aspect has to be considered. In contrast to fcc (face-centred cubic) metals, where the fracture behaviour is less dependent from temperature, bcc (body-centred cubic) metals exhibit a material property referred to as ductile to brittle transition temperature (DBTT). This means that below a certain temperature depending as well on the respective metal as on the loading rate and on the condition of the respective material (like grain size, recrystallized, etc.) a bcc metal will show brittle behaviour, above this DBTT the metal will show ductile fracture behaviour. One of the origins of this different behaviour of fcc and bcc metals is the difference in Peierls potential / Peierls stress [21]. If a bcc metal is loaded below its DBTT, the external stress will exceed the inherent cleavage stress of the material before significant dislocation movement is activated, resulting in brittle fracture of the material. At higher temperatures dislocation are thermally activated

and dislocation movement can take place more easily. Therefore, above some specific temperature threshold (the DBTT) bcc metals become tougher and do not break in a brittle manner. In fcc metals the Peierls potential is low enough for thermal activation of the dislocations being not necessary, thus fcc metals always will behave ductile. Figure 2.3 gives some rough comparison of the magnitude of the fracture toughness K_{IC} of fcc metals, bcc metals and cast iron, and as well of the dependency of the K_{IC} on the temperature for these materials.

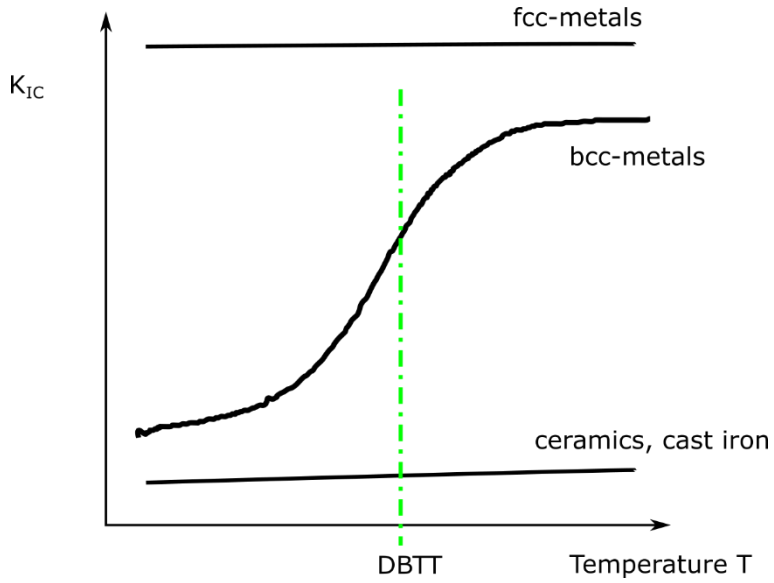

Figure 2.3: Schematic representation of the dependency of the fracture toughness on the temperature for bcc and fcc metals.

2.3. R-curve

An increase of the fracture resistance with increasing crack extension is called an R-curve behaviour. In the simple LEFM approach the fracture resistance of a material is assumed to be independent of the crack extension Δa. The energy needed to produce a fracture surface under LEFM conditions is the sum of the specific surface energy necessary to create new surfaces and the specific plastic work to extend the crack, which both are assumed to be independent of the total crack length. As a consequence of these assumptions, the critical energy release rate and consequently the critical stress intensity factor K_{IC}, too, should not depend on the crack extension Δa. The R-curve of an ideal brittle material is flat and looks like the graph to the left of figure 2.4, exhibiting no increment in fracture resistance with crack length increasing. As soon as a material shows an R-curve behaviour, as sketched

schematically in the graph on the right-hand side of figure 2.4, the critical stress intensity factor as a single value, is not sufficient anymore to describe the fracture behaviour of this material. In this case, a graph of the stress intensity factor as a function of the crack extension (shortened: an R-curve) is required in order to describe the fracture behaviour of this material completely.

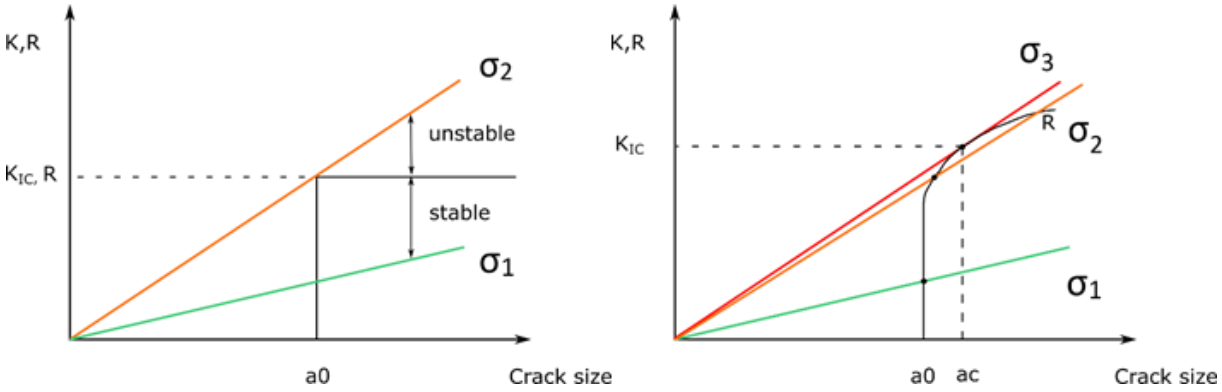

Figure 2.4: Schematic representation of the R-curve behaviour of an ideal brittle material on the left; the graph on the right shows a typical R-curve shape of a ductile metal. The lines differently coloured represent different external loads applied ($\sigma_1 < \sigma_2 < \sigma_3$). In the brittle material on the left-hand side the load σ_2 already leads to an unstable crack growth, resulting in failure of the component. For a material with an R-curve behaviour the same load σ_2 just causes some stable crack growth. Only when the load applied is being increased further up to σ_3, an unstable crack growth will take place in the ductile material represented on the right-hand side.

A rising R-curve is always an indicator that toughening mechanisms take place within a material while it is being fractured. An overview of potentially toughening mechanisms is given in chapter 2.4. For measuring the crack extension while testing the samples for this thesis the Direct Current Potential Drop Method (DCPM) was used. The DCPM benefits from a physical property of any conductive material, namely the electrical resistance R of the sample will increase [Eq.2.7] if the cross-sectional area A of this material diminishes (e.g. by crack growth).

$$R = \frac{l}{A} * \rho \qquad \text{[Eq.2.7]}$$

The electrical resistance R is measured indirectly by determining the potential difference U occurring according to Ohm´s law (U=R*I) when an electric current of amperage I is passing through the sample. To be able to measure the very small crack extension in the magnitude of tens of micrometres and to achieve a potential signal of sufficient hight, corresponding to the increase of R resulting from crack growth, a current as high as possible is applied onto the

samples. The potential difference $U\text{-}U_0$ measured during the test is being converted into a crack extension by means of the Johnson Equation [Eq. 2.8], where a is the actual crack length, a_0 the initial crack length, W the sample width, U the actual potential, U_o the initial potential from the start of the test and 2λ the distance between the two measuring leads [22]. Figure 2.5 sketches a possible testing configuration for the DCPM.

$$a = \frac{2*W}{\pi} * \cos^{-1}\left\{\frac{\cosh\left(\frac{\pi*\lambda}{2*W}\right)}{\cosh\left(\frac{U}{U_0}*\cosh^{-1}\left(\frac{\cosh\left(\frac{\pi*\lambda}{2*W}\right)}{\cos\left(\frac{\pi*a_0}{2*W}\right)}\right)\right)}\right\} \qquad \text{[Eq.2.8]}$$

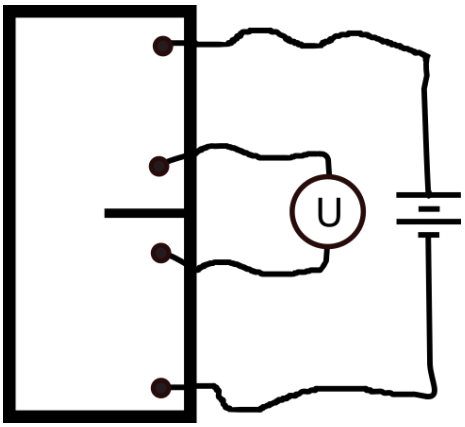

Figure 2.5: Sketch of a possible testing configuration for the DCPM.

2.4. Toughening mechanisms in metals

Crack extensions are caused by the presence of a crack driving force like the stress intensity factor K_I, and they are opposed by the fracture resistance of the material, which depends on the microstructure of this material. Except in ideal brittle materials, where it depends solely on the surface energy. The growth of a crack can be restrained by lowering the load applied or by toughening the material. R.O. Ritchie et al. conducted extensive studies on the mechanisms of fatigue-crack propagation in ductile and brittle solids [23] and on the toughening mechanisms in metals and other materials [24] as well, the short summary given hereafter is based on their work. Basically, two sources for toughening effects can be distinguished, to be specific, intrinsic and extrinsic mechanisms. The intrinsic toughening mechanisms refer to increasing the bond strength and increasing the ductility, e.g. by microstructural changes like grain size and texture optimization or lowering the proportion of segregations. Intrinsic toughening mechanisms are changes of properties inherent to the material and therefore independent of the crack length and the geometry of the sample. Extrinsic toughening mechanisms shield the crack tip from the crack driving force (zone shielding, contact shielding). These shielding mechanisms result from the creation of inelastic zones around the crack or from physical contact between the crack surfaces by means of crack bridging (i.e. tungsten fibres reinforced tungsten), wedging (i.e. from oxide films, or rust particles) or cracking of weaker precipitates in front of the crack to absorb a part of the energy from the crack driving force (stress-intensity factor), or crack deflection (on very tough particles for example) and meandering. If any of these extrinsic toughening mechanisms occurs in materials, these materials show an R-curve behaviour.

2.5. Electron backscatter diffraction (EBSD)

The electron backscatter diffraction is a method of scanning electron microscopy which uses the information gathered by electrons after being diffracted on crystallography planes within the sample according to the Bragg's law and captured subsequently by a phosphor screen. The source of these diffracted electrons are electrons scattered elastically within the sample, on their part sourcing from the primary beam of the scanning electron microscope (SEM) directed onto the sample (figure 2.6).

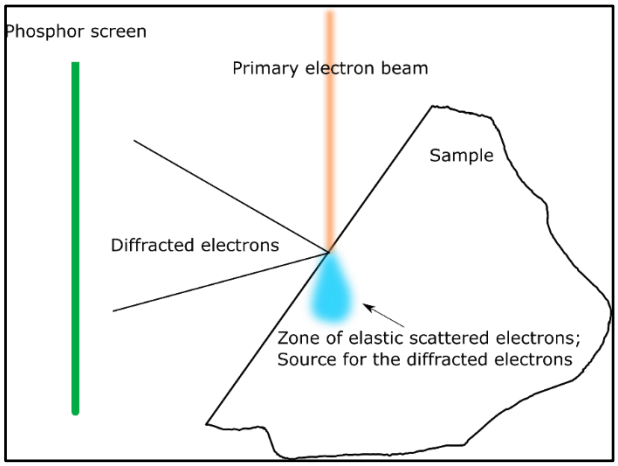

Figure 2.6: Schematic representation of the generation of diffracted electrons for EBSD.

The image on the phosphor screen created by the diffracted electrons represents so-called Kikuchi-Patterns, lines in these patterns represent the lattice planes of the sample. Intersections of these lines form zone axes, which are identified by the angles between the lines and the zone axis. The position and knowledge of the identity of these zone axes and the knowledge of the exact experimental setup is then used to calculate the crystal orientation map. Figure 2.7 shows how a result of a grain orientation analysis by means of EBSD can look like, a coloured coded orientation map, with the standard orientation triangle as legend. The EBSD method is used to acquire knowledge on the crystallographic orientation of and within the grains, on grain size, grain shape and texture eventually occurring within the sample [25–27].

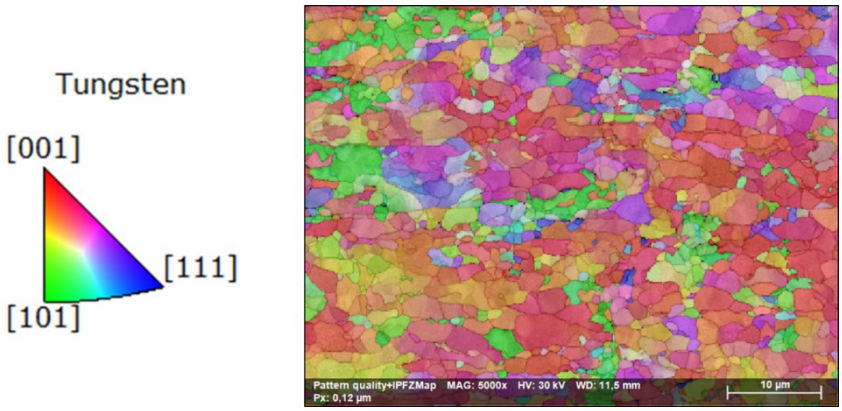

Figure 2.7: Result of an EBSD scan, with the orientation triangle to indicate which colour represents which orientation.

In figure 2.8 the meaning of the different colour-coding used in figure 2.7 is shown, as well as how grains are aligned regarding the surface of the sample.

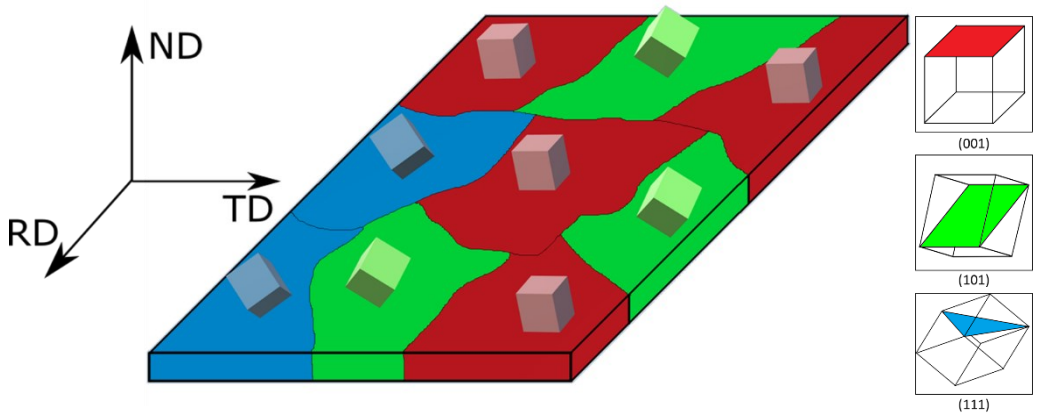

Figure 2.8 Schematic representation of the meaning of the different colours in an EBSD scan in terms of the alignment of grains regarding the surface of the sample.

3. Material

The materials used in this thesis were provided by the company PLANSEE SE (Reutte, Austria) and the Karlsruhe Institute of Technology (KIT). Tungsten sheets were produced in the conventional powder metallurgic route. Due to the high melting point of W and the high reactivity with oxygen the production of this metal by means of melting is quite challenging. An overview of the W production is given in figure 3.1. Source material for the W production is tungsten trioxide WO_3, found primarily in the minerals Wolframite and Scheelite. The WO_3 is reduced under a hydrogen atmosphere to metallic W at temperatures between 500 °C and 1000 °C ($WO_3 + 3H_2 \rightarrow W+3H_2O$). The pure W powder is then mixed with sintering aids and, depending on the product, mixed additionally with doping or alloying elements like potassium, lanthanum or rhenium. This procedure is followed by pressing the W powder into a bar or disc shape, which is done via hot isostatic pressing and sintering afterwards at temperatures of 2000 °C approximately. The thermomechanical processing performed subsequently to the sintering (for example, rolling the material at different temperatures, with or without recrystallization) has a major influence on the microstructure and consequently on the properties of the material[28].

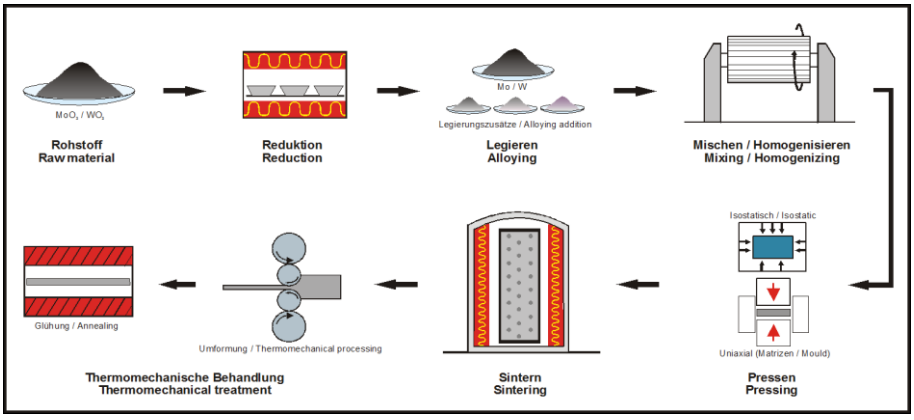

Figure 3.1: Process route of the Mo and W production [28].

The goal of this thesis was to examine how varying microstructures influence the fracture toughness and the R-curve behaviour of fracture toughness of pure W samples. One of the easiest ways to influence the microstructure of a material is by deformation. For this thesis a

well-defined deformation was applied to the materials by means of hot-and cold rolling. A detailed description of the processing route for the 1 mm, 0.5 mm, 0.2 mm and the 0.1 mm is given in the following.

A pure W ingot was hot rolled to a thickness of 6 mm at a temperature higher than 1200 °C, so recrystallization could occur. The material then was “cold rolled”, i.e. rolled at temperatures between 1200 °C and 300 °C, which is below the recrystallization temperature, to a thickness of 0.2 mm. During this cold rolling process, samples were taken at 1 mm, 0.5 mm and 0.2 mm thickness. Further rolling was performed to reach a sheet thickness of 0.1 mm, “low-temperature rolling” with a temperature below 300 °C [13,29].

In references given further below in this thesis the various plates, sheets and foils tested are referred to as 2 mm material, 1 mm material, 0.5 mm material, 0.2 mm material and 0.1 mm material. The samples are labelled by giving the sample number followed by the material designation. For instance, sample 3_0.1 mm would be the label for the third sample of the 0.1 mm material. Referring to the two letter code for sample orientation nomenclature of the ASTM E399 [19], the standard test method for linear-elastic plane-strain fracture toughness K_{IC} of metallic materials, the samples in this thesis were tested in L-T direction. The first letter designates the direction normal to the crack plane, and the second letter the expected direction of crack propagation, as shown in figure 3.2. In the tests performed the samples were loaded in rolling direction, the expected direction of crack propagation was normal to the rolling direction.

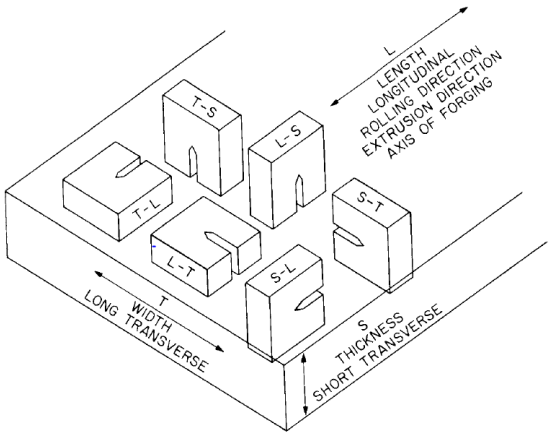

Figure 3.2: Sample nomenclature according to ASTM E399 [19].

It seems worth to emphasize that the 1 mm, the 0.5 mm and the 0.2 mm material tested in this thesis were produced from one and the same W ingot. Therefore, any variation in chemical composition, with potential influence on the microstructure or the mechanical properties, could be excluded. The materials cited were provided by the KIT in the shape of 50 mm x 70 mm^2 sheets. The 0.1 mm material was processed following the same production path as the other materials, though from a different W ingot. No details on the production and the thermomechanical treatment were known for the 2 mm plate; however, the microstructure could be determined by EBSD and its parameters (grain size, strength of texture) could be used for the discussion of the results. Energy dispersive X-ray spectroscopy (EDX) was carried out on the 2 mm and the 1 mm material. The EDX spectrum (Figure 3.3) clearly confirmed that the two materials analysed were pure W, as far as the sensitivity of this method allows.

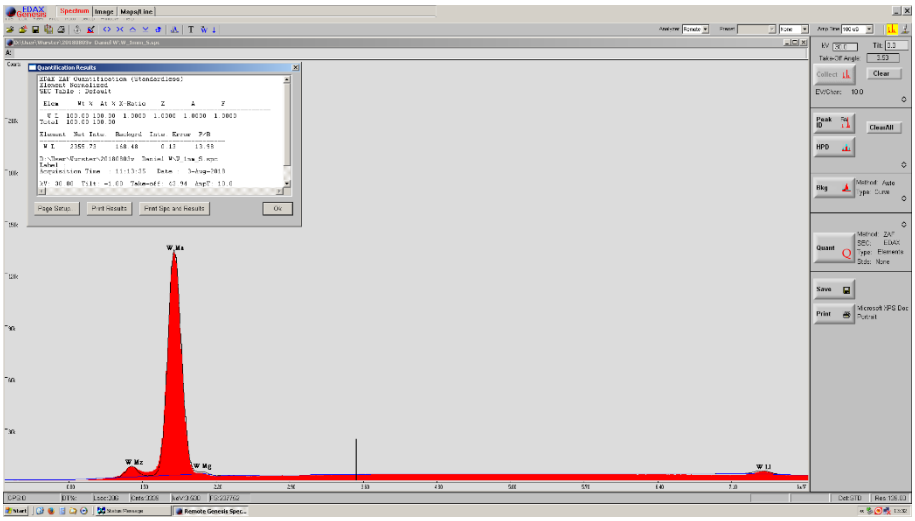

Figure 3.3: EDX spectrum for the 1 mm sample. The result shows that the sample indeed is pure W.

4. Experimental methods

The goal of this thesis was to examine how varying microstructures may influence the fracture toughness and the R-curve behaviour of pure W samples. The respective microstructural features like grain size, grain orientation and texture were analysed by means of EBSD. The influence of the microstructure was investigated by measuring the fracture toughness and using the DCPM to determine the occurring crack extension when the five materials specified in chapter 3 were tested in L-T direction at RT and at 200 °C. Higher testing temperatures were considered but would have required an extremely complex experimental set-up. Due to the increasing oxidation of W at elevated temperatures the tests would have to be performed in vacuum. High temperature tests on such W samples are covered in [9,10,30–32].
The fracture surfaces for all samples tested were examined in the SEM and are discussed in chapter 5.2, as well as the respective results of the fracture toughness. On materials which exhibited an R-curve behaviour, the so called 80 % tests were performed in addition. Samples were loaded under normal testing conditions at 200 °C up to approximately 80 % of their maximum bearable load expected, then the loading was stopped and the samples were cooled down slowly. Afterwards the samples were broken in liquid nitrogen (LN) and micrographs of the fracture surface were taken with the SEM.

4.1. General considerations on sample design

After decision to fix the number of materials which will be tested to be five (viz. 2 mm, 1 mm, 0.5 mm, 0.2 mm and 0.1 mm), that the tests will be performed only in one testing direction (viz. in L-T direction addressed in chapter 3, figure 3.2). However, the tests have been performed at two different temperatures, namely at RT and at a temperature of 200°C. A few more questions had to be answered, e.g. the following: Which sample dimension would work best? How should the samples be prepared? How should they be tested and under which conditions should the tests be performed?
Because of the particular processing route of the materials provided by the KIT (for more information see chapter 3) the amount of material available was quite limited. Considering

these limitations and using the knowledge of the latest studies on those materials to be tested [13], i.e. the experience gained from experiments done on W foils at the ESI [10] the sample dimension used was set to 24 x 10 mm^2 (figure 4.1).

The reasons for the sample size chosen were beside to maximize the possible number of samples out of the 70 x 50 mm^2 sheets provided by the KIT, to have enough space for wire connections and drill holes eventually needed, too.

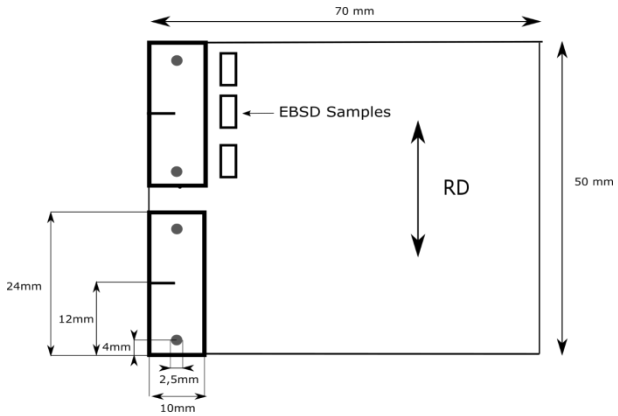

Figure 4.1: Sketch of the 2 mm sample preparation.

4.2. Microstructural analysis via EBSD

Using electrical discharge machining (EDM), for the purpose of microstructure analysis samples were cut out measuring up to 4 x 6 mm^2 at most, depending on the amount of material available. For each material, samples were prepared for scans into three viewing directions, with these directions being orientated parallel to the transversal direction (TD), to the rolling direction (RD), and to the normal direction (ND) perpendicular to the foil. Although the orientation and consequently the texture as well are known from one single scan already, scans from all three directions yield access to the anisotropic grain shape. The 2 mm and the 1 mm material samples were large enough to be handled without being embedded. The 0.5 mm, the 0.2 mm and the 0.1 mm samples had to be hot embedded in a conductive polymer called Polyfast. The surface preparation for all samples was done using an automated preparation system by the company STRUERS (Sarasota, Florida, USA). In this preparation system three samples were mounted together at the same time, the only modification necessary was to change the grinding plates and to clean the samples and the grinding plate

used after every step. For the polishing a few drops of a diamond suspension and a few drops of dihydrogen dioxide were added on the polishing plate in order finally to receive a clean and smooth surface. Subsequently, the prepared samples were mounted in an SEM sample holder and taped with copper foil to increase the electrical conductivity (to help lead off electrons for increased image stability (figure 4.2)). It seems worth to note that the copper tape necessarily had to be taped over a big part of the sample area to fulfil its purpose. Subsequently the sample was placed in the vacuum chamber, being ready for the EBSD scanning. For EBSD analysis, the SEM of type LEO 1525 (Zeiss) equipped with an EBSD detector type e-Flash (Bruker) was used. Typical imaging conditions were a large aperture size of 120 µm, maximizing the probe current and an acceleration voltage of 30 kV. The data was analysed using the software Esprit 2.1 from Bruker.

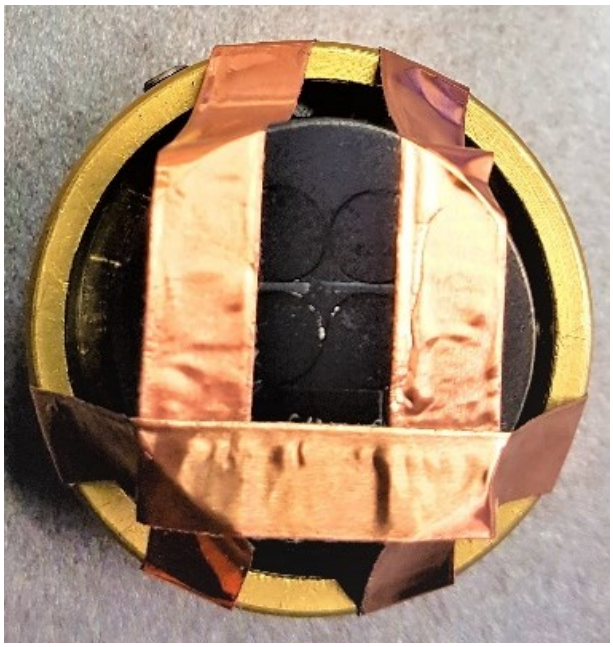

Figure 4.2: Side surface and front surface samples of the 0.5 mm material embedded and ready to be scanned.

4.3. Fracture toughness and R-curve experiments

4.3.1. Considerations and calculations necessary for designing the samples and the experimental set-ups

The development of the sample design is described in chapter 4.1 already. The next step was to determine the best suitable experimental set-up, and to choose which testing device should be used, which furnace, what load cell and how the sample should be mounted in the testing linkage. The experience with this kind of experiments was limited, therefore every test gave new insight to adjust and improve the set-up for the samples following. Finally three different experimental set-ups for different sample thicknesses were established, which will be described in detail further below. (Chapters 4.3.6 to 4.3.8).

To determine which size of load cell would be needed, rough calculations for the 2 mm and 1 mm samples were carried out considering a SECT (single edge cracked plate tension) sample, and using the equations 4.1 and 4.2 according to Murakami [33].

$$K_{IC} = \sigma * \sqrt{\pi * a} * f_I(\alpha) \qquad \text{[Eq.4.1]}$$

$$f_I(\alpha) = 1{,}12 - 0{,}231 * \alpha + 10{,}55 * \alpha^2 - 21{,}72 * \alpha^3 + 30{,}39 * \alpha^4 \qquad \text{[Eq.4.2]}$$

$$\alpha = \frac{a}{W}$$

$$\sigma = \frac{P}{B * W}$$

$$P = \frac{K_{IC} * B * W}{\sqrt{\pi * a} * f_I(\alpha)}$$

The values inserted in the calculations were as follows: For the 2 mm sample the sample thickness B was 2 mm, the sample width W was 10 mm, the crack length a was 5 mm, and the

fracture toughness K_{IC} was estimated to be 25 MPa√m. The force necessary to break the sample was calculated to be 2823 N.

$$P = \frac{K_{IC} * B * W}{\sqrt{\pi * a} * f_I(\alpha)} = \frac{25\ MPa\sqrt{m} * 2mm * 10mm}{\sqrt{\pi * 5 * 10^{-3}m} * 2{,}826} = 2823N$$

For the 1 mm material the same calculation was performed, with the sample thickness now being 1 mm, the sample width W being 10 mm, and the crack length a being 5 mm. The fracture toughness K_{IC} was set to be 86 MPa√m, this value taken from Bonnekoh et al. [13], who had tested the fracture toughness using another method. The result of this calculation led to a force of 2430 N necessary to break the sample.

For the calculation of the bolt/hole size needed the higher force value was used. It may be of interest that in the very beginning using a shorter crack length of about 2 mm was intended, but in this case a much higher force would have been required and therefore much bigger bolts would have been needed. Below, a rough estimation of the bolt diameter is shown. Figure 4.3 shows the drawing used for the calculations.

$$d = \sqrt[3]{\frac{P * 1.5 * 16}{\sigma b * \pi}}$$

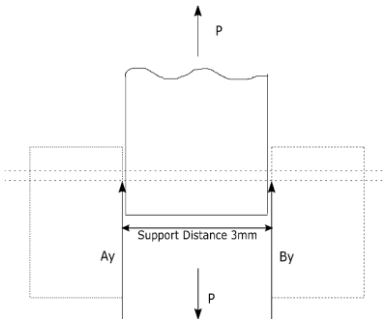

Figure 4.3: Drawing of a built-in sample to calculate the minimum bolt diameter and the used equation.

The minimal bending strength for ceramic bolts (Al_20_3) is about 300 MPa and about 2500 MPa for a bolt made of high-speed steel (HSS). Bolts made of ceramics would have been preferred, but due to the low bending strength and the large bolt diameter herefrom resulting bolts of HSS have been used. According to the equations and the sketch above (figure 4.3) the minimal bolt diameter with a safety factor of 1 would be 4.14 mm for the ceramic and 2.05 mm for the HSS steel. For this reason 2 mm HSS steel drill bits were chosen as bolts, actually the shank of the drill bit having been used only, the drill body was cut off.

4.3.2. Pre-cracking

The fracture toughness is defined as the resistance of a material against the propagation of a crack already existing. In order to achieve proper measurements of the respective fracture toughness, the samples consequently need to exhibit a sharp and stable pre-crack[2]. There are several well-established methods for introducing a pre-crack into a sample, like cyclic compression, FIB machining, compound bending and electrical discharge machining. Gludovatz et al. [32] provided a very useful comparison on these methods, taking into account all the advantages and drawbacks of each method in their paper about crack propagation resistance in pure W. Mainly due to the large variation in sample thickness two different approaches were used to achieve the goals of this thesis, accompanied by some trials on a third method of pre-cracking, those three methods addressed being described below.

- **Pre-Cracking for the thicker samples (2 mm/1 mm/0.5 mm): Cyclic Compression**

A short fatigue crack is a sharp crack used as stable pre-crack for the fracture toughness experiments. To initiate this crack in the thicker samples, the method of cyclic compression was chosen. Each load cycle leads to a cyclic plastic strain at the notch, which is the cause of the crack initiation. To avoid any issues with buckling or off-centre loading, a special sample holder was used, equipped with different spacers to make it usable for 2 mm, 1 mm and 0.5 mm samples. The notch necessary for the cyclic compression procedure was introduced into the sample by using EDM, and consequently refined further by means of a razor blade polishing using a 6 µm diamond suspension. The samples were polished prior to the cycling procedure to be able to see these cracks. All the thicker materials except one were polished on both surfaces. The 0.5 mm samples were polished on just one side, because polishing one side removed at about 100 µm of the sample thickness already. The cyclic compression took place on a high frequency fatigue testing machine from Russenberger & Müller (RUMUL), with the length of the cracks obtained depending on the stress intensity factor range ΔK_I (K_{max}-K_{min}) applied, on the stress intensity ratio R ($R = K_{min}/K_{max}$), on the number of cycles N and last but

[2] A stable pre-crack is a crack which grows upon initiation in an uncritical manner, it does not extend until the load on the sample is increased further.

not least on the size of the sample [34]. Changes on R were necessary to ensure that the samples at any time were under compression load, with this ratio R ranging from 4 to 10 depending on the sample and the minimum load applied. A schematic visualisation for R is given in figure 4.4a. For the cycling procedure the sample was placed below the upper stamp of the RUMUL in the sample holder, ensuring by visual inspection that the notch of the sample was placed directly underneath the loading bolt (figure 4.4b). The samples then were loaded with a pre-determined stress intensity factor range ΔK_I for 30000 cycles and examined subsequently for visible cracks at the notch with the light microscope (LIMI). The stress intensity factor range ΔK_I started at 4 MPa√m for materials not yet tested and was increased in steps of 2 MPa√m for another 30k cycles in case no cracks were seen with the LIMI. Figure 4.5 presents sample 11_2 mm prior to the pre-cracking on the left and after pre-cracking on the right. The fatigue crack length was determined to be approximately 38 µm.

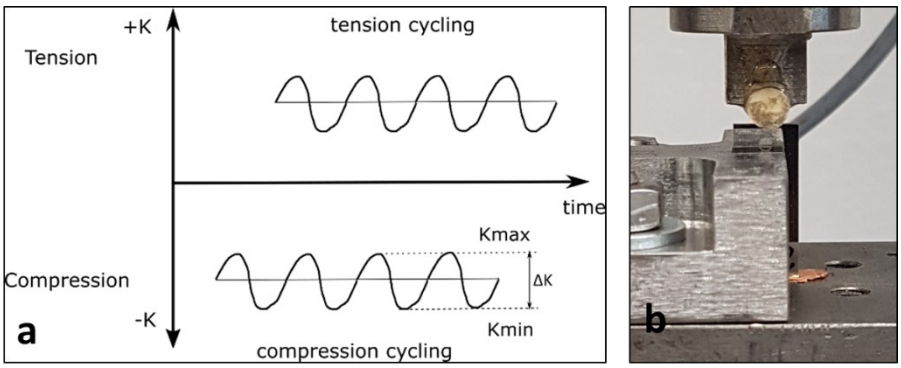

Figure 4.4: a) Load conditions during cycling; b) 2 mm sample during the cyclic compression process.

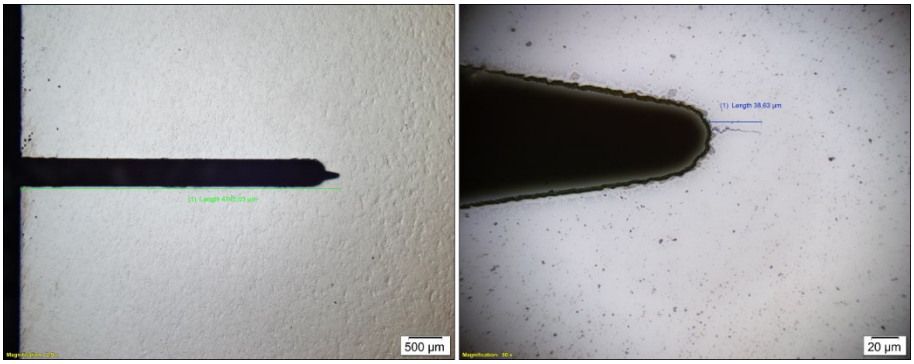

Figure 4.5: Sample 11_2 mm prior to the pre-cracking on the left-hand side and after pre-cracking on the right-hand side. On the left the notches resulting from EDM and razor blade sharpening are depicted. The fatigue crack length was determined to be approximately 38 µm.

- **Pre-cracking of the thinner samples (0.2 mm and 0.1 mm): FIB machining**

Because of a high probability to destroy one of the thinner samples in the course of a cyclic compression procedure due to the higher probability of buckling for these samples, the difficult task of polishing the side faces of a sample already very thin, and as well due to the limited amount of material available, the pre-cracks for the thinner materials were initiated by means of another method. A well-established method for producing a sharp pre-crack in foils is the focussed ion beam (FIB) machining, already used by Nikolić et al. [10]. The pre-notch was cut by means of EDM followed by a refinement of the notch by using a razor blade and diamond suspension, as having been carried out for the thicker samples. Afterwards the samples and especially the notches were cleaned thoroughly, using isopropanol and compressed air. The notches subsequently were examined with the LIMI to ensure no dirt would interfere with the FIB. The samples were placed in bundles of three into the focused ion beam workstation (Leo 1540, Zeiss). One after the other two cuts were done in the root of the refined notch of the samples. The first cut with a current of 10 nA and a milling time between 120 s and 180 s was used to check the correct position of the FIB directed onto the notch of the sample. The second cut was done with the same current and a milling time of 60 min for the 0.1 mm samples and 120 min for the 0.2 mm samples, resulting in the same ion fluence rate. The result was a pre-crack with depth of a few µm, ranging through the whole thickness of the sample. Very likely intended cracks seem to propagate from this FIB induced sharp pre-cracks. In figure 4.6 the fracture surface of sample 1_0.2 mm is shown, the area red framed marks the pre-crack induced by FIB, its length being 10 µm.

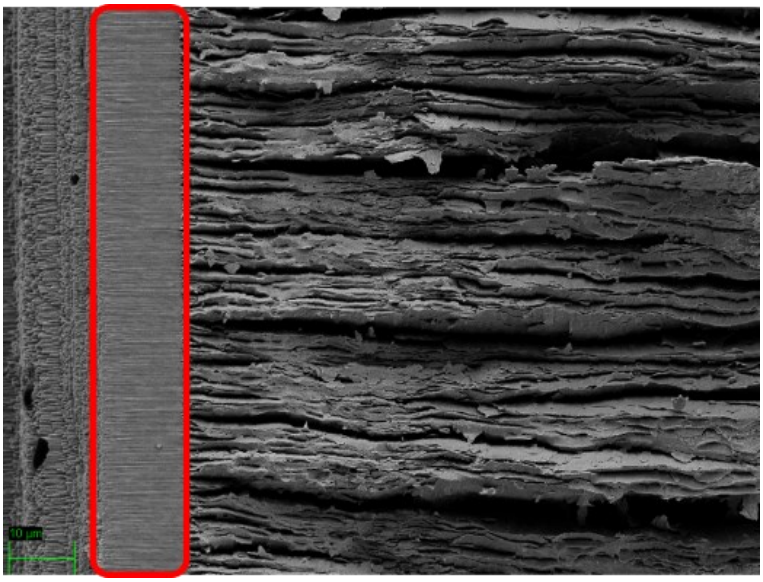

Figure 4.6: Fracture surface of sample 1_0.2 mm. Red framed area marks the FIB induced pre-crack with a length of approximately 10 µm.

Pre-cracking experiments with 0.1 mm samples: Thermal shock cracking

By means of cyclic compression a sharp fatigue crack ideal for fracture toughness experiments can be introduced in the sample. For the reasons already mentioned inducing a fatigue pre-crack in thin samples is quite difficult. Even though FIB machining delivers quite good results in term of sharp pre-cracks, these FIB milled notches are not ideally sharp. The idea of the experiments described below was to introduce a natural sharp crack in the 0.1 mm W foils by means of a thermal shock. For this experiment 0.1 mm foils were prepared in the same way as the samples described above, they were milled by FIB in order to feature a pre-crack of a radius as small as possible and thus a stress concentration at the crack tip as high as possible. To be able to recognize a crack occurring due to these thermal shock experiments the samples had to be polished. Mechanical polishing was not possible due the low thickness, so electrolytic polishing was performed, reducing the sample thicknesses to approximately 60 to 70 µm.

As an attempt further to refine the FIB-pre-crack the procedure following was developed: Two copper blocks were put into a container full of liquid nitrogen (LN) and left there to temperate. In two other copper blocks larger than the ones addressed above the samples were fixed in the way following: The end of the pre-crack slightly protruded the copper blocks, with just the ligament of the sample actually having been fixed between the copper blocks (figure 4.7). This

sample holder with the sample fixed in was then put into a furnace at 300 °C for 30 min. Then the set-up was put out of the furnace and immediately the two LN-tempered copper blocks addressed at the beginning of this paragraph were clamped on both sides of the sample (figure 4.7). The idea was that the temperature gradient resulting would induce tensile stress at the tip of the notch, which in its turn would lead to a thermal crack. Rough calculation putting in a thermal expansion coefficient α of $4.5*10^{-6}$ /K [1] and a Young´s-Modulus of 405 GPa for W resulted in a thermal stress of about 810 MPa at the crack tip with a temperature difference of about 500 K. Taken into account the thermal expansion of copper and the thermalization of the W-foil at intermediate temperature, a smaller stress acting at the crack tip could be expected. Several samples have been tested this way, but none of them showed any crack initiation. Figure 4.8 presents a sample prior and after the thermal shock treatment; no crack extension was recognisable with the LIMI.

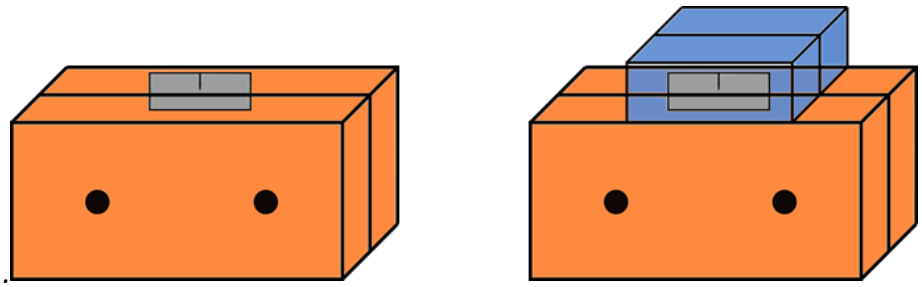

Figure 4.7: On the left: Sample (grey) fixed in the copper sample holders (orange), temperated in the furnace;
On the right: Copper blocks (blue), temperated in LN and clamped onto the sample.

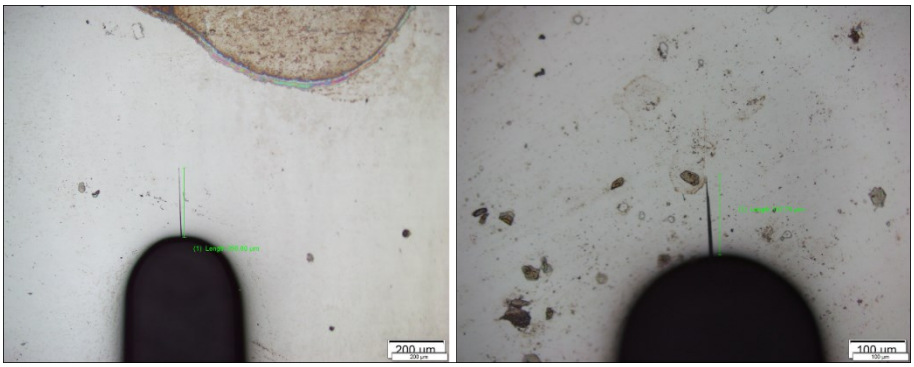

Figure 4.8: On the left: sample prior to the thermal shock treatment; On the right-hand side: sample after the thermal shock treatment.

4.3.3. Wiring

To measure the crack extension Δa during the experiment the direct current potential drop method (DCPM) was used. A description of the DCPM has been provided in chapter 2.3. already. For applying this method the sample must be wired to a potentiometer and to a constant current supply as well; two contacts are needed for each of them. The standard method for wiring samples in the DCPM is by pining them with 1.4 mm silver coated pins, plugging wires onto these pins and connecting them to the corresponding device. This standard method of wiring was not applicable for most of the materials tested in this thesis. The smallest pins available featured a diameter of 1.4 mm. Because of the spatial restrictions due to the small sample size and the experimental set-up chosen the pins for wiring could only be stuck into the front face of the samples, a method applicable for the 2 mm samples only. In order to gain comparability of the measurements for all the materials to be examined, the challenge was to find a method likewise applicable for each of the materials. Even though the weldability of W is very limited because of its high melting point and the immediate oxidation at elevated temperature, one of the most promising methods of joining the wires and samples was spot welding, called point welding as well. Point welding was used because it is a commonly used technique and applicable for a lot of different materials. For the first tests of point welding, dummies of the 2 mm material were used due to the vast amount of 2 mm material available. Fixing the wires turned out to be challenging. The corresponding welding experiments started off with W wires of varying diameters, however none of these wires attached at all to the sample after point welding. Even at maximum power the point welder was not able to melt the W wires. As a possible alternative copper and platinum wires were tested, too, once again with different diameters and varying welding parameters. Results were as before, the wires did not connect to the W sample. Rather by accident than on purpose the next wire tried out was a K-thermocouple (NiCr-Ni) wire, which attached to the sample properly. Referring to the Ni-W phase diagram [35] shown in figure 4.9, W is able to form intermetallic phases with Ni which allow Ni-wires to connect to W samples. For further welding experiments a 0.5 mm Ni-wire with 99.5 %wt. Ni was used. The mechanical strength of the welds still was relatively poor. For the 2 mm samples tested first, in addition to the welding spots a drop of super glue was put on top of the wires in the experimental set-up,

with the idea that the super glue could absorb most of the mechanical stress exerted during soldering and loading of the specimen. This method worked but could be used for RT experiments only. For the 200 °C experiments a few other glues were tested, glues based on epoxide resin or glues based on silver or carbon with an organic solvent (glues which are used in the SEM and TEM preparation). None of those glues increased the mechanical strength of the bond, so for the 200 °C tests no kind of glue was used.

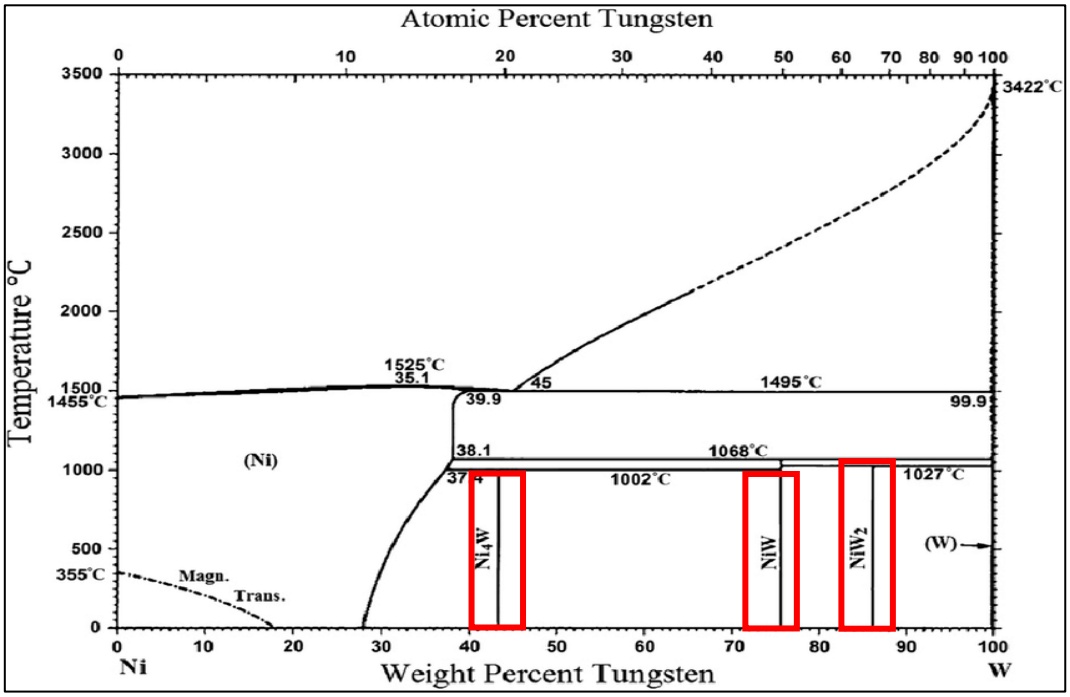

Figure 4.9: Ni-W phase diagram, with marked intermetallic phases [34].

In the course of the experiments ongoing a lot of work was invested to improve the wiring process. A detailed description of the refined wiring process resulting is given hereafter:
All wires used were Ni-wires with 99.5 %wt. Ni and 0.5 mm Ø. Before the wires could be point welded to the samples a few steps of preparation were necessary. For thermal and electric insulation the wires were shrouded in a 0.5 mm high temperature silicate glass insulation. To be able to connect the wires with the corresponding devices, a 1.4 mm silver coated pin was soldered to each wire on one side, for the 200 °C experiments the pins were hard soldered to the wires. For preparation of the respective point welded spots of the samples and the wires some ethanol, sanding paper, a side cutter and tweezers were needed. To remove dirt or any oxide layer on the wire the first few millimetres were nipped off and the part of the wire to be point welded to the sample was cleaned with ethanol and kept free of any dirt until the

welding. The corresponding sample was fixated in a sample holder in order to facilitate the correct positioning below the electrode of the point welder. At the welding position of the sample the surface was ground carefully, followed by removal of any dirt or oxides and cleaned afterwards by removing grinding debris with a soft cloth dipped in ethanol. A wire was positioned below the electrode by means of a pair of tweezers, the electrode subsequently being lowered onto the wire, clamping it between the electrode and the sample (the thinner the W samples got, the more careful this had to be done). When the wire was at the position required, the point welder was activated and a current was sent from the electrode through the wire, melting it partially. The two adjustable parameters of the point welder, viz. the current strength and the duration of the welding process had to be adapted for every material, heavily depending on the thickness of the material (e.g. welding time of 2 s and an amperage of 2 A for a majority of the 0.1 mm samples). Depending on whether the wire already stuck sufficiently firm to the sample or not, if necessary, a second or even a third spot weld was made to ensure the wire stuck reliably to the sample. Even with this approach in some cases a wire fell off, or at least the wire eventually was to fall off during testing. In these cases, the whole procedure of careful grinding and cleaning had to be repeated before the wire could be point welded onto the sample again.

This is the proper place to put some note for anybody whom this might concern, e.g. because in future intending to perform measurements in the same way as described in this thesis: In order to perform successfully the respective measurements, the preparation steps already described above and those described below had to be performed very carefully because of a quite large probability to restart the respective experiment with lots of work invested in vain in case anything went wrong (several examples might be found in this chapter).

Figure 4.10 gives impressions of the progress made in the wiring process, image a) showing one of the first attempts on point welding a sample, b) shows depicting a point welding in progress and image c) presenting one of the 0.2 mm sample nicely point welded and ready for testing.

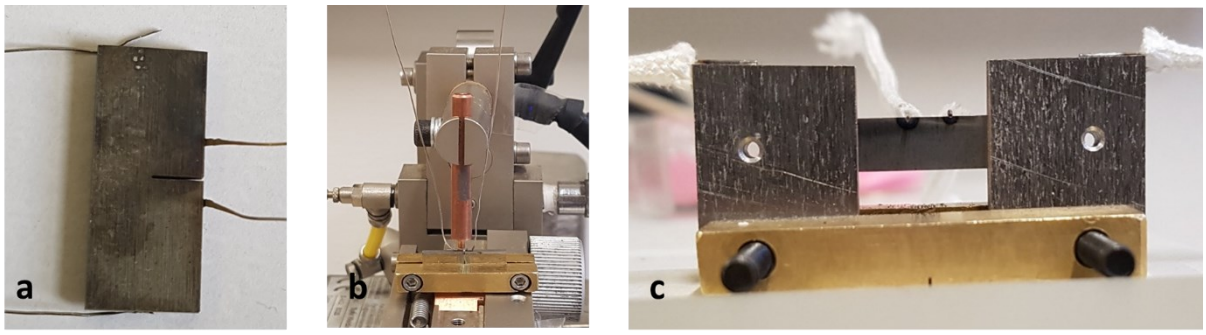

Figure 4.10: a) The result of one of the first point welding trials. b) Point welding in progress. c) 0.2 mm point welded sample, ready for testing.

As discovered during improving the experimental set-ups, the direction in which the wires were point welded to the sample had a severe impact on the stability or instability of the potential measurement. To emphasize this influence on the potential stability, figure 4.11 presents a schematic sketch of the two different possible welding directions. The wires in the example on the left-hand side still were able to move a little bit under load, resulting in variation in the size of the contact surface and consequently leading to a change in the potential measured. In summary, the setup depicted to the left will result in a very unstable crack length measurement. On the right-hand side the wires are point welded over the whole sample thickness to the sample, so no variation in the size of contact area and position on the sample is possible.

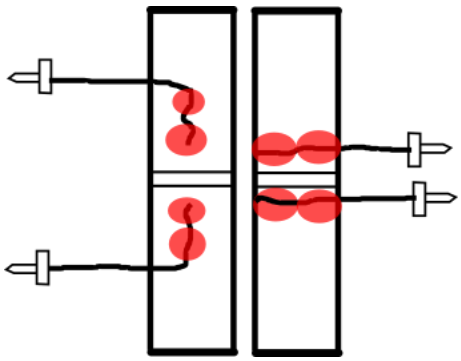

Figure 4.11: A schematic sketch of the two directions in which wires may be point welded onto the sample. The red areas symbolize the welding spots. On the left-hand side the wires still can move a little bit, resulting in a contact surface of variable size. On the right-hand side, the wires impossibly may move, assuring a constant size of contact surface.

4.3.4. Sample preparation finally adopted for the thicker samples

In addition to the steps already described in 4.3.2 and 4.3.3 this chapter will give a brief summary on how the thicker samples (2 mm, 1 mm and 0.5 mm) were prepared and in which order the particular steps were done. Figure 4.12 depicts the instruction to manufacture the 2mm samples, an instruction to be adjusted after the first experiments with the experimental set-up I have been performed (for description of this set-up see ch.4.3.6).

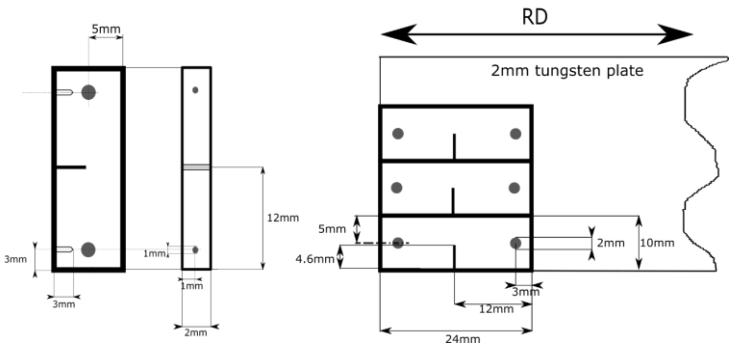

Figure 4.12: Manufacturing instructions for the 2mm samples.

This instruction was modified once more for the samples tested latest, the diameter of the drill hole was increased to 2.4 mm to be able to use 2.2 mm bolts coated in Kapton tape for the purpose of electrical insulation. In figure 4.13 to the left one of the 2 mm samples tested first can be seen, to the right one of the 2 mm samples tested in later design is presented.

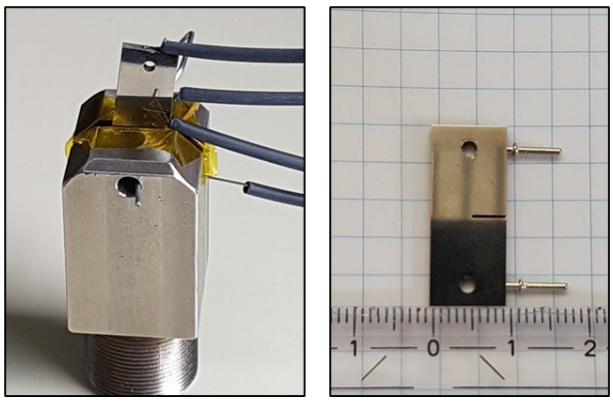

Figure 4.13: On the left-hand side: One of the first 2 mm samples; On the right-hand side: One of the latest 2 mm samples after a few adjustments.

With the results received from the experimental set-up I (described in chapter 4.3.6) a few modifications of the sample preparation were necessary. One of the goals of this thesis was to test all samples in a way as similar as possible. Thus, using 0.5 mm Ni-wires for both the current supply and the potential measurement was intended. The issue with these 0.5 mm Ni-wires was these wires being limited to a current of 2 A applicable at most. Higher currents led to an increased temperature of the wires and the samples, which led to variations in the electrical resistance influencing the potential measurement. In the first tests with the 2 mm samples the electrical resistance of the 2 mm samples turned out to be too low for 2 A to result in reliable potential drop measurements. Hence, the approach of testing all the samples in the same way had to be adjusted. The current supply for each material was adjusted to result in the best possible potential measurement. Figure 4.14 gives a summary on the methods used to supply current to the samples.

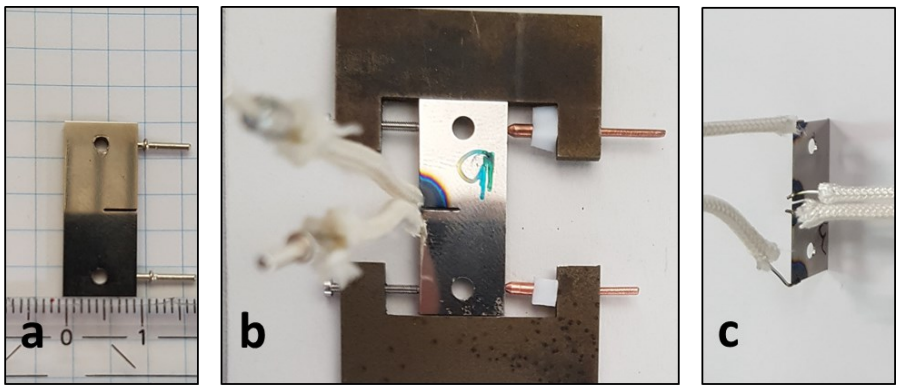

Figure 4.14: Examples of different ways to supply power to the samples. a) Pins for the 2 mm samples. b) Clamps for the 1 mm samples, power is supplied using Cu-pins; c) Ni-wires directly welded onto the 0.5 mm samples.

Important remark: Despite using different ways to supply current to the samples, the samples always were welded to 0.5 mm Ni-wires which then were connected to the nanovoltmeter for the potential measurements. The same sample dimension of 24 x 10 mm^2 was used for the 2 mm, 1 mm and 0.5 mm material. The targeted crack length a_0 was from 4.5 mm to 4.8 mm which results in an a/W ratio from 0.45 to 0.48. After cutting a notch with the EDM, refining the notch with the razor blade and inducing the pre-crack by means of cyclic compression, the samples were cleaned with isopropanol in an ultrasonic bath. After each of these steps the notch/crack length was measured with the LIMI.

The final initial crack length a_0 was measured with the LIMI on both surfaces of the sample and was used as crack length a_0. In order to mount the thicker samples in the linkage of the experimental set-up, two 2.4 mm holes were drilled into the samples in the course of the sample cutting process. Through these holes the samples were fixed and mounted in the experimental set-up. Besides fixing the samples in the testing linkage the bolts were used to transfer the force applied by the experimental set-up to the samples, too (figure 4.15).

Figure 4.15: 2 mm sample mounted by Kapton covered bolts in the experimental set-up.

A brief bullet point list for the sample preparation of the 2 mm/1 mm/0.5 mm samples:

- Cutting the sample with the EDM, drilling necessary holes for pins and/or bolts
- Refining the EDM notch with a razor blade using a 6 µm Diamond suspension
- Cleaning, grinding and polishing the side faces of each sample to be able to see, whether a crack has formed after a cycling step
- Initiation of a stable pre-crack by means of cyclic compression
- Wiring the samples:
    - The 2 mm samples were pinned, enabling the supply of 9 A
    - The 1 mm samples were current supplied via clamps, limiting the current to 6 A
    - The 0.5 mm samples were too thin even for the clamps, therefore 0.5 mm Ni-wires were used for the current supply, limiting the current to 2 A.
      (Remark: The 0.5 mm samples were polished on one side only)
- Point welding the wires for the potential measurement onto the samples
- Measuring the distance (2λ) between the wires for the potential measurement using a calliper

4.3.5. Sample preparation finally adopted for the thinner samples

For the 0.2 mm and the 0.1 mm samples the method used to mount the thicker samples was not applicable. The issue with the 0.2 mm and the 0.1 mm samples was that if bolts were used to transfer the force to the sample, the probability of merely elongating the drilled holes was very high. This deformation would lead to some variation in the electric resistance resulting in an incorrect R-curve. Another method to fix the samples in the experimental set-up had to be found.

Experiments using clamps for mounting the samples into the experimental set-up revealed new undesirable issues. The grip of the clamps on the samples was quite weak even when the clamps were sandblasted before the samples were mounted. In one out of two experiments the clamps were not able to clip the sample properly, with the sample being pulled out of the clamp. Furthermore it was very challenging to ensure the samples were aligned perfectly straight in the clamps with respect to the loading direction, and into the bargain buckling occurred during fracture testing of samples (figure 4.16). Hence, the three issues of buckling of the samples, non-perfect alignment and the restricted amount of force applicable to the samples due to limited grip of the clamps had to be resolved in order to test the 0.2 mm and 0.1 mm samples in a reliable manner.

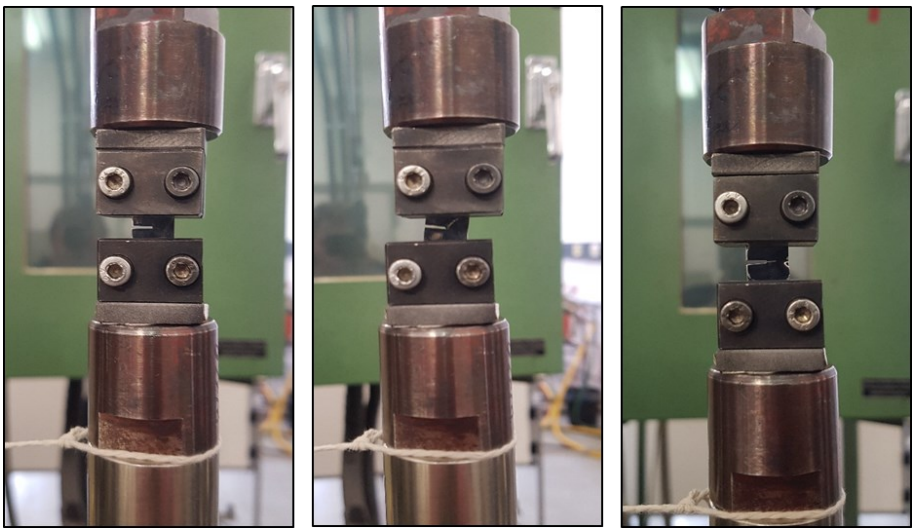

Figure 4.16: 0.1 mm samples during experiments with clamps. The image in the middle depicts the problem when the sample is not aligned perfectly, or when the grip of the clamps is not constant over the whole clamping area. The third image demonstrates the bucking phenomenon.

A few approaches were considered. A reduction of the a/W-ratio would reduce the propensity of the sample buckling drastically, though with the consequence of a much higher force needed to break the sample. This would not be applicable in case clamps were used to mount the samples. Another concept considered to remove buckling was to switch the sample set-up from samples with one crack (SENT) to samples with cracks on both sides (DENT). Calculations done for the sample 5_0.1 mm following Murakami [33] for the SENT and DENT configuration showed that the force necessary to fracture the samples would be 281 N for SENT and 834 N with the DENT configuration. With a force that high the clamps used impossibly could hold the samples in place. Furthermore, using the DENT configuration would also double the FIB time for pre-crack initiation, which was quite extensive already. The most promising idea was to use the sample preparation method developed by Nikolić et al. [30] for testing 0.1 mm ufg-W foils. In order to avoid buckling Nikolić et al. had used a smaller sample width W of 5 mm. To mount the samples in the experimental set-up the samples were hard soldered into steel sample holders to avoid clamps and bolts. The disadvantage of this method with respect to the goal of this thesis was the imperative to switch to smaller sample dimensions. A switch of sample size form 24 x 10 mm^2 to 24 x 5 mm^2 for the 0.2 mm and 0.1 mm samples (figure 4.17) was pre-condition for the thinner samples to be bested in this manner. In the course of changing dimensions the starting crack length was switched from 5 mm to approximately 1 mm in order to get an a/W-ratio of 0.2 approximately (to avoid buckling and to have more space available for the crack to grow). To mount the samples they were brazed into 15 x 15 x 3 mm^3 steel sample holders. The holders were cut by using EDM, while the slit for the samples was created with a SECOTOM cutting machine using a 0.3 mm thick tungsten carbide cutting disk for the 0.1 mm samples and a 0.5 mm thick corundum cutting disk for the 0.2 mm samples. For the brazing, the samples were placed in the slit of the sample holders between two brazing foils with a thickness of 0.1 mm. For the 0.2 mm samples the amount of brazing foil was doubled on one side of the sample. As brazing foil an eutectic silver cooper foil with 72 wt.% Ag and 28 wt.% Cu was used. The advantage of using these foils was their excellent wettability on the W samples without any diffusion [5] into the W and their melting temperature being relatively low, so no recrystallization of the samples should take place [30]. The samples were put into a brazing holder specially designed and were placed subsequently in the vacuum chamber of the furnace. The brazing took place in high vacuum at 780 °C for 20 minutes, followed by subsequent furnace cooling. A detailed description of

the pre-cracking and the wiring was given in the chapters 4.3.2 and 4.3.3. A sample brazed and already wired is presented in figure 4.18.

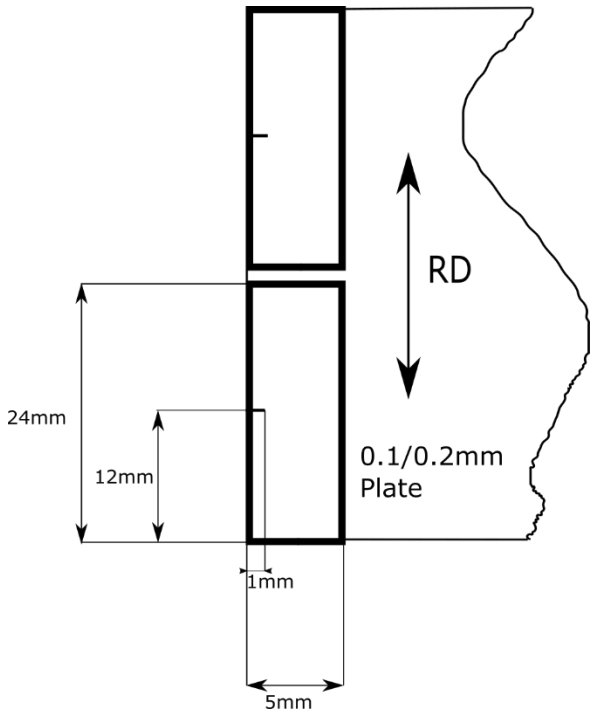

Figure 4.17: 0.2 mm / 0.1 mm sample with the dimensions changed according to preconditions of the new testing mode applied.

Figure 4.18: Brazed and wired 0.2 mm sample, ready to be tested.

A brief bullet point list for the sample preparation of the 0.2 mm / 0.1 mm samples:

- Cutting the sample by use of EDM
- Refining the EDM notch with a razor blade
- Cleaning the samples
- Initiation of a stable pre-crack by means of FIB machining
- Soldering the samples into steel sample holders
- Wiring the samples with two 0.5 mm Ni-wires for current supply, limiting the current to 2 A. The wires are point-welded onto the steel sample holders and not to the samples anymore
- Point welding the wires for the potential measurement onto the samples
- Measuring the distance (2λ) between the wire for the potential measurement by using a calliper

4.3.6. Experimental set-up I

A large task of work for this thesis was to establish a sample preparation method proper and reproducible. Sometimes modification of the experimental set-up was necessary, in order to test materials of different thickness in a way ensuring a stable potential measurement. The first experimental set-up failed regrading reliable and stable potential measurements. Major modifications had to be figured out regarding the experimental set-up, but as well on the design and preparation of samples. Experimental set-up I (figure 4.19) was an approach to test the crack extension Δa by means of the DCPM in the course of a standard fracture toughness test, resembling a set-up successfully deployed already for fracture toughness test of ufg W foils in Nikolič et al. [30].

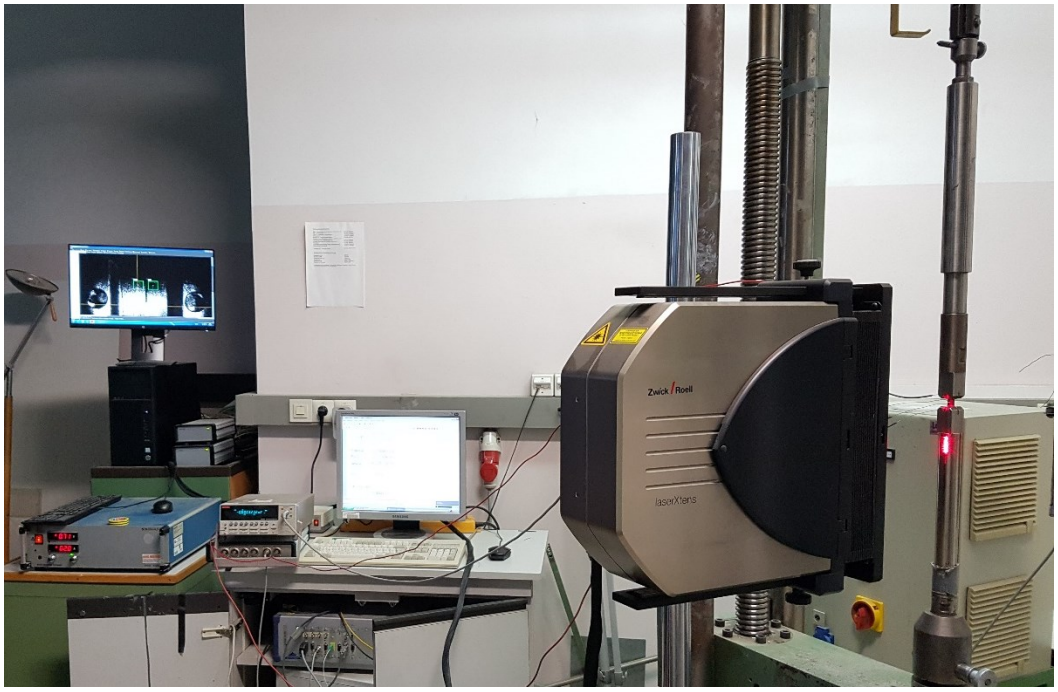

Figure 4.19: Experimental set-up I, almost complete as deployed in one of the experiments. The laser extensometer is pointing at the sample for measuring the displacement of the sample. The sample is fixed within a long linkage, which leaves enough space for later furnace mounting (the furnace is not placed within the frame of the image).

Experimental set-up I consisted of:

- ZWICK Multi-purpose testing device
- ZWICK laser-extensometer HD/TZ ZWICK/ROELL
- Low-voltage power supply unit FUG NTN 350-6,5
- Nanovoltmeter KEITHLEY 2182A
- Polarity reversal device I_{max} = 10 A
- HERAEUS tube-furnace for temperatures up to 1000 °C
- Thermocouple type K
- Signal converter DEWERTRON DEWE 30-16
- Software DASYLab 9
- 10 kN load cell

At RT and 200 °C, this set-up should be able to:

- measure the load applied to the sample
- measure the displacement of the sample
- measure a stable potential prior to the test as well as the deviation in the potential occurrent in the course of the test in case of crack extension
- measure the temperature at the sample

After establishing a procedure properly to wire the samples, three 2 mm samples were prepared to be examined in pre-tests by means of this first experimental set-up. The correspondent sample preparation is described in chapter 4.3.4 already. Before mounting the samples into the experimental set-up a few trials with the potential measurement were carried out in order to verify the stability of the measurement. Simultaneous measurement of the load applied and the potential occurring allowed deriving an R-curve in case the material showed an R-curve behaviour. The samples were electrically separated from the rest of the experimental set-up to avoid disturbances in the potential measurements. For this reason a part of the lower linkage had been electrical insulated, and in addition to this the sample holders were coated with Kapton tape, a temperature resistant and electrical insulating material (figure 4.20).

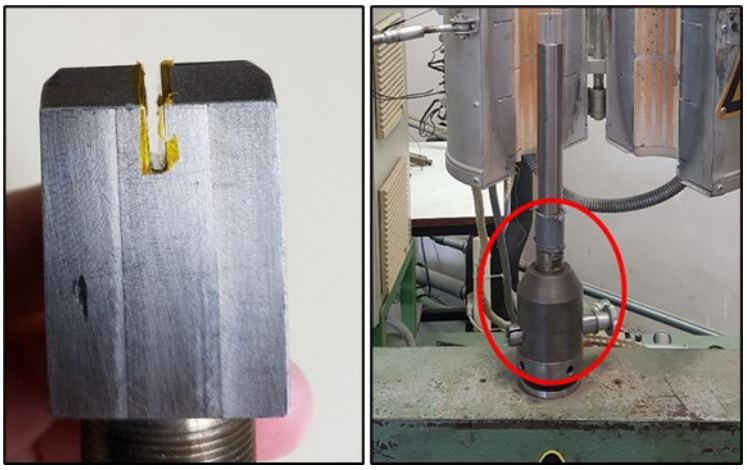

Figure 4.20: To the left: Kapton tape coated sample holder; To the right: Lower part of the experimental set-up, the red area marks the adapter with the electrical insulation incorporated.

The experimental procedure started with an inspection of the load cell by applying weights of 2 kg and 10 kg to the top linkage and checking the indicated weight on the computer. Subsequently the functionality of the thermocouple was checked by holding the exposed contacts into the flame of a lighter. The inspection of the setup was completed by controlling the alignment of the experimental set-up using a dummy sample first. The software used to record all the experimental data is called DASYLab 9, it recorded the force applied to the sample, the potential drop on the sample and the displacement of the sample. Once the software was started, the sample was mounted in the experimental set-up and a force of approximately 100 N was applied immediately. Next, the thermocouple was fixed near the sample on bolts and wires for the power supply and for the potential measurement were connected to the respective devices. The laser-extensometer was put into place and aligned with the edges of the notch for the displacement measurement. The current was set to 2 A on the power supply and the recording of the measurement was restarted. Figure 4.21 depicts sample 1_2 mm after fracture but still mounted in the experimental set-up. Sample 1_2 mm was tested at RT with a testing speed of 0.4 mm/min.

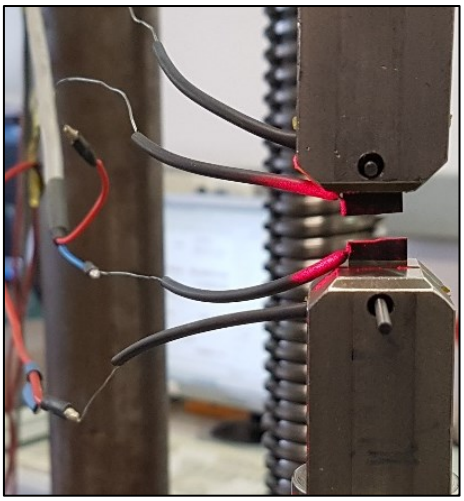

Figure 4.21: Sample 1_2 mm after fracture, still mounted in the experimental set-up.

The sample fractured under a load of 1223 N resulting in a fracture toughness of 24.4 MPa√m. The potential measurement was very noisy and unstable, the maximum value of the potential was 77.291 µV, the minimum value 75.683 µV. Converting the utmost drop of potential would result in a crack extension of 6 µm (figure 4.22), though with a potential measurement thus unstable it would be very challenging if not impossible at all to measure crack extensions expected to be in the range of a few micrometres.

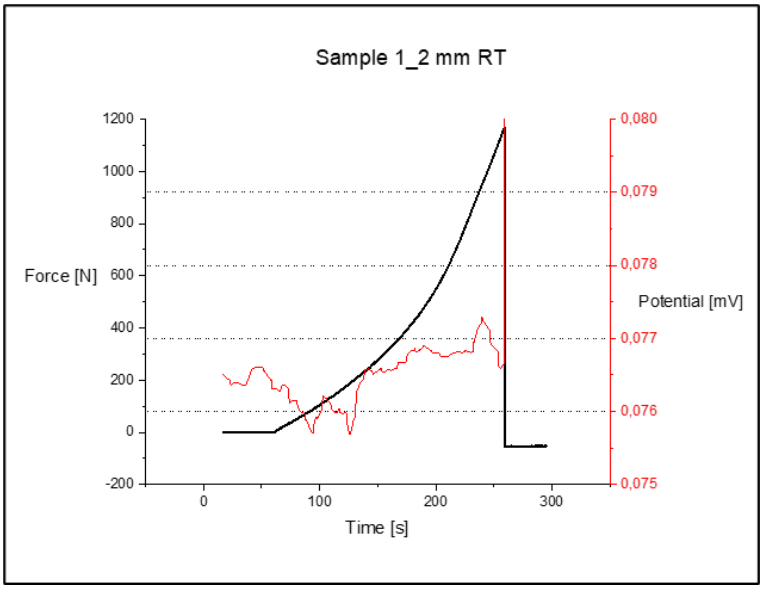

Figure 4.22: Potential (red) and Force (black) graphs of sample 1_2 mm. As being observable there were no issues with the force measurement, but there were severe instabilities with the potential measurements, making it difficult to determine crack extension on a µm-scale.

Sample 2_2 mm was tested at RT as well, at a speed of 0.4 mm/min but with a current increased to 3 A. The higher current should have lowered the signal to noise ratio. Most likely due to the Ni-wires warming up this resulted in an even more noisy and unstable potential signal (figure 4.23). With this kind of instability in the potential measurement this set-up was not even close to be able to measure crack extension in W samples on the micrometre scale. The sample fractured under a load of 985 N resulting in a fracture toughness of 21.2 MPa√m.

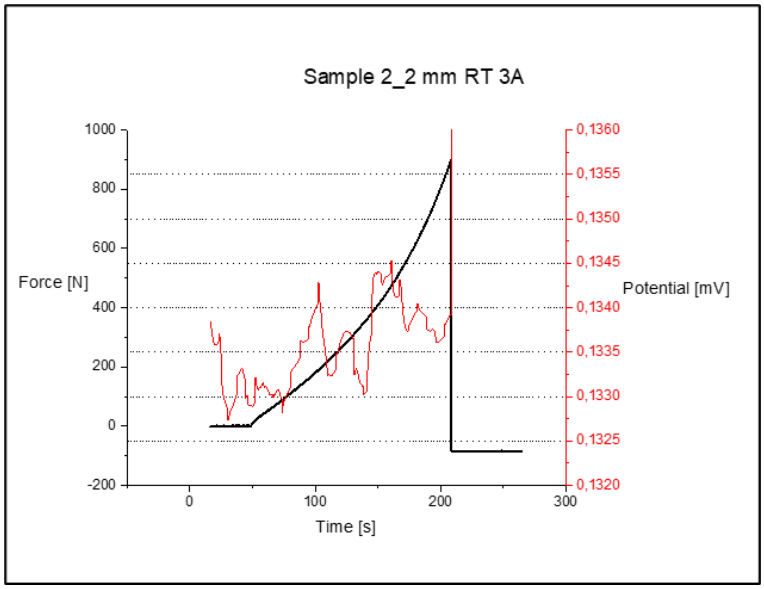

Figure 4.23: Potential (red) and force (black) graphs of sample 2_2 mm. As being observable no issues with the force measurement were evident, but the potential measurement was significantly worse compared to the first sample tested.

The third sample tested with experimental set-up I, i.e. sample 3_2 mm, was tested at a temperature of 250 °C in atmosphere. All the other testing parameters like preload and testing speed were the same as in the previous tests. This test revealed even more issues regarding this set-up. For the furnace to work properly the tubular heating chamber should be closed around the sample. A complete closing of the chamber was impossible due to the wires connecting the sample to the power supply and the nanovoltmeter. Furthermore, the laser-extensometer needs direct view to the sample to be able to measure the displacement (figure 4.24). Since the furnace had to stay open the temperature was very unstable, the furnace temperature had to be set to 460 °C to reach approximately 250 °C on the sample. Due to the unstable temperature the potential measurement was more unsteady than before (figure 4.25). For the sake of testing the fracture toughness the experiment was continued, however the results of the potential measurement were unusable.

Figure 4.24: Set-up for sample 3_2mm tested at 250°C; on the right the tubular heating chamber of the furnace can be seen.

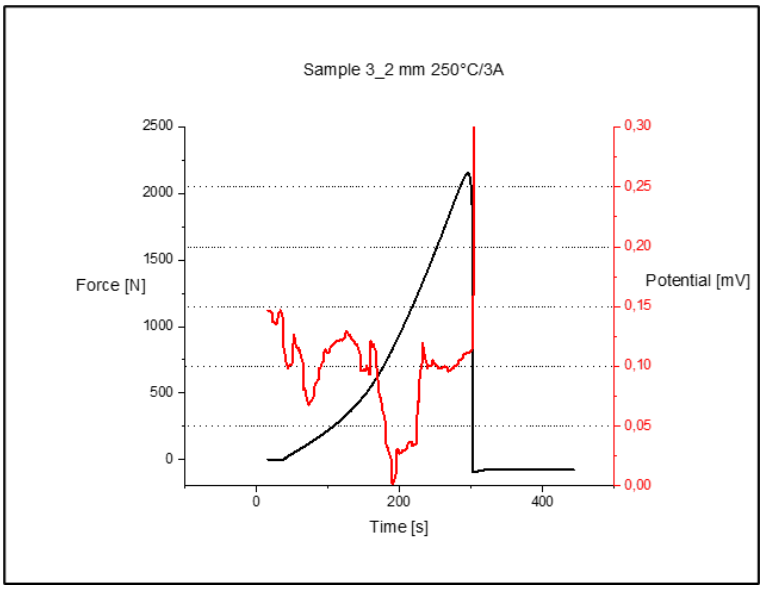

Figure 4.25: Potential (red) and Force (black) graphs of sample 3_2 mm tested at 250 °C; as being observable there were no issues with the force measurement, but just a very random potential signal.

The sample fractured under a load of 2228 N resulting in a fracture toughness of 55.7 MPa√m. The experiments performed till now revealed that the experimental set-up used was not applicable for this kind of R-curve experiments. The influence of small variations of temperature and even small air currents had been underestimated. At this stage of the thesis a lot of work went into literature research, into dummy testing with varying set-ups and sample configurations, improving the wiring process and testing of diverse nanovoltmeters,

power supplies and wire connections. One of the major problems of this set-up was the high sensitivity on temperature changes. The signal limit of the KEITHLEY 2182A nanovoltmeter is 60 nV peak to peak round about, with a response time of 60 ms [36]. The goal for the set-up to be developed was to reach a stable signal with a noise maximum of 100 nV peak-to-peak.

4.3.7. Experimental set-up II

Discussions on the issues resulting from the principles adopted in the experimental set-up I led to modifications in the set-up design. Details of the set-up II finally adopted are given below, visual impressions of set-up II are given in figures 4.26 and 4.27.

1. By using now 0.5 mm Ni-wires for the current supply, the electrical current was limited to 2 A. Using these wires for the power supply was caused by the intention to test all samples in ways as similar as possible. The 2 mm experiments were negatively affected by this principle. Due to their larger cross-sectional area, thicker samples feature a lower electrical resistance than thinner samples. For a reliable potential measurement rather large currents were needed for the thicker samples, therefore every material was tested with a current at maximum limit with respect to the sample wiring. For the current supply of the 2 mm samples pins were used, permitting the current to be increased to 9 A. The way the potential was measured (using 0.5 mm Ni-wires) remained the same for every sample and every material.
2. Improvements of the point-welding procedure had a significant influence on the performance of the potential measurement, which clearly improved as well. This especially applied to the wire configuration on the samples (for details see chapter 4.3.3).
3. Additional thermal and electrical insulation was achieved by shrouding the wires with a high temperature silicate glass insulation of 0.5 mm inner diameter.
4. Further electrical insulation was added, now completely separating the sample from the rest of the experimental set-up by means of Kapton tape coated bolts and an additional electrical insulation adapter in the top part of the linkage also.

5. Considering the massive issues with the tubular furnace chamber and temperature instabilities when using experimental set-up I, the whole set-up was moved to another ZWICK (multi-purpose testing device). The furnace attached to this ZWICK is a closed furnace chamber using hot circulation air. The temperature in this furnace was limited to 200 °C. The circulating air flow did not have any negative impact on the measurement, on the contrary the closed furnace chamber isolated the sample from any environmental influences. The furnace had a side access allowing wires to lead into the chamber. Temperature resistant, insulated cable extensions were used to access the furnace and connect the wires with the respective devices. The only drawback of this closed furnace chamber was that displacement measurements using the laser extensometer were not possible anymore.
6. The testing speed was decreased to 0.2 µm/min in order to allow the nanovoltmeter to register crack extensions more easily.

Figure 4.26: Experimental set-up II, with closed furnace chamber.

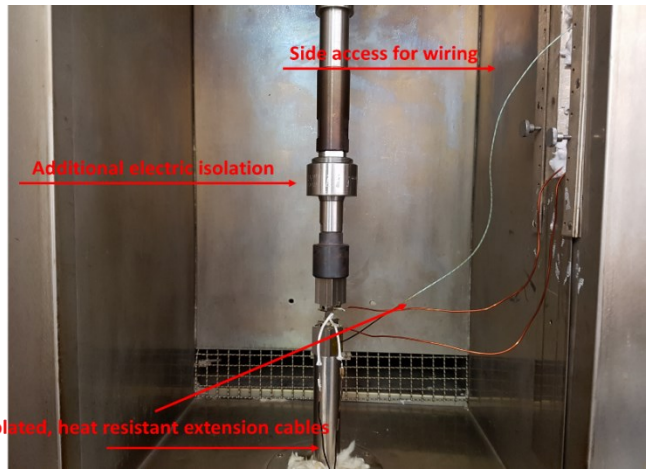

Figure 4.27: Set-up inside the furnace chamber, side access and bottom access were insulated by means of silicate glass fibre insulation.

The device list for experimental set-up II:

- ZWICK Multi-purpose testing device
- ZWICK hot air oven
- Low-voltage power supply unit FUG NTN 350-6,5
- Nanovoltmeter KEITHLEY 2182A
- Polarity reversal device I_{max} = 10 A
- Thermocouple type K
- Signal converter DEWERTRON DEWE 30-16
- Software DASYLAB 9
- 10 kN load cell/1 kN load cell (for the thinner samples)

Prior to testing the first sample, all the procedures described in chapter 4.3.6. for experimental set-up I (e.g. to control the load cell and the thermocouple) were conducted for set-up II as well. Moreover, every switch in testing speed now was controlled by means of a dial gauge and a stopwatch. Conducting the experiments was as follows: Before mounting a sample the recording of the force applied was started, subsequently the samples were pre-loaded with a pre-load of 20 to 100 N dependent on the respective thickness of the material. Next, all the wires were connected to their respective devices and the power supply was turned on. The furnace chamber was closed, and the recording of the measurements was started. Before conducting the test on the sample a waiting period of 10 to 20 minutes was let passing to ensure the initial potential was stable. In case of this precondition not being fulfilled the wire connections were checked once more, and sometimes the sample had to be removed from the set-up and had to be rewired once again. The stable initial potential before the experiment was used as U_0 for the calculation of the crack extension Δa according to the Johnson-Equation (chapter 2.3). When a stable potential exhibited the experiment was started and conducted until the sample fractured. For the 200 °C experiments the sample had to be monitored, in order to control that the preload during the heating process remains constant. This was done by slowly lowering the crosshead continuously to keep a constant force applied to the sample. After reaching the target temperature of 200 °C, a waiting period of about 15 minutes was let pass to ensure stability of temperature and to check once more whether the potential was stable as well. In case each precondition was fulfilled the experiment was conducted.

Fractured samples were cleaned in isopropanol, with the fracture surfaces being examined afterwards in the SEM.

4.3.8. The LN-experiments

The goal of the experiments described in this chapter was to examine the development of the fracture surface due to the crack extension of materials that showed an R-curve behaviour when tested at 200°C. Samples of materials (1 mm and 0.5 mm)which showed delamination only at 200°C were tested like the samples prior to them at 200°C, just without the wires for the power supply and the potential measurement. Samples which exhibited delamination already at RT where tested like the samples prior to them at RT. The test was stopped when reaching 80 to 90 % of the estimated load for fracture approximately. The sample was cooled down slowly at first and unloaded afterwards. To be able easily to distinguish the fracture surface formed by stable crack growth during the loading of the sample at 200 °C and the fracture surface formed by just fracturing the sample, the sample was fractured subsequently in LN (figure 4.28). To be able to conduct this procedure the experimental set-up slightly had to be modified (the furnace and the wiring was removed, at the lower part of the linkage a pot able to hold the LN was added and sealed to the linkage with sanitary silicone). The sample was mounted in the altered set-up and LN was filled into the pot. Once the sample was covered in LN completely, it was loaded until fracture with the same standard testing speed of 0.2 mm/min. After half an hour of warming the sample could be removed from the set-up. After cleaning the sample in isopropanol, the fracture surfaces were examined in the SEM.

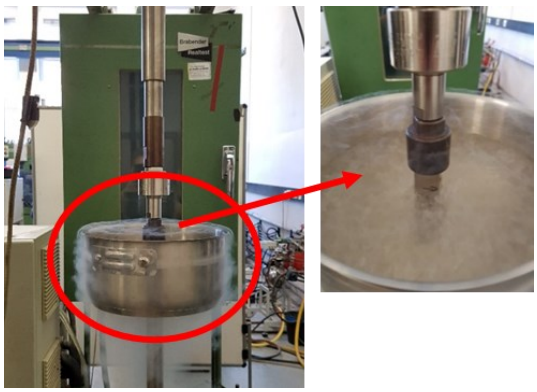

Figure 4.28: Adjusted experimental set-up, to fracture the samples under LN.

5. Results and discussion

5.1. Microstructure

In this chapter the results of the microstructural analyses carried out by means of EBSD are summarized. First topic will be a presentation of the results of the grain size determination and a discussion on the impact of the respective experimental parameters chosen on the results obtained. Next topic will be to give an overview of the microstructure for all materials examined. Last topic will be the development of this microstructure in the course of the different stages of rolling by comparing the texture of the materials of 1 mm, 0.5 mm, 0.2 mm and 0.1 mm to each other.

5.1.1. Grain size

This chapter is focussed on the determination of the respective grain sizes of the materials. In table 5.1 the results achieved are listed with respect to the correspondent degree of deformation, the grain size, and the respective value of the total number of grain count considered for determining this grain size. The development of the grain sizes, a function of the degree of deformation, obtained is as expected in case where no intermediate recrystallization occurs. The results were derived for a pixel-to-pixel misorientation of 15°. A discussion on the influence of the analysis settings chosen on the results is given below.

Table 5.1: Results of the grain size measurements for all samples tested.

Material thickness	Degree of deformation	Grain size [µm]	Grain count
2mm	Unkown	3.4	365
1mm	1.8	3.0	563
0.5mm	2.5	2.3	726
0.2mm	3.4	2.1	1351
0.1mm	4.1	1.5	2078

The degree of deformation φ and its calculation according to the appropriate formula is given below for the 1 mm material in Eq.5.1., corresponding values for all materials investigated are given in table 5.1. The thickness h_0 (=6 mm) refers to the thickness of the original W plate before the thermomechanical processing was carried out. The thickness h_1 refers to the actual sample thickness.

$$\varphi = \ln\left(\frac{h_0}{h_1}\right) = \ln\left(\frac{6mm}{1mm}\right) = 1{,}79 \qquad \text{[Eq. 5.1]}$$

Figure 5.1 presents the images used for the different materials to determine their grain size, the orientation triangle for tungsten (or inverse pole figure) appendant and a sample reference plate for easier catching the meaning of the colours. Due to the rolling process, a strong anisotropy of grain shape (elongated grains) is expected, getting more pronounced with increasing degree of deformation. These characteristics of the materials cannot be detected when looking in ND, but they can be recognized easily when looking in TD (to the side face) or RD (to the front face).

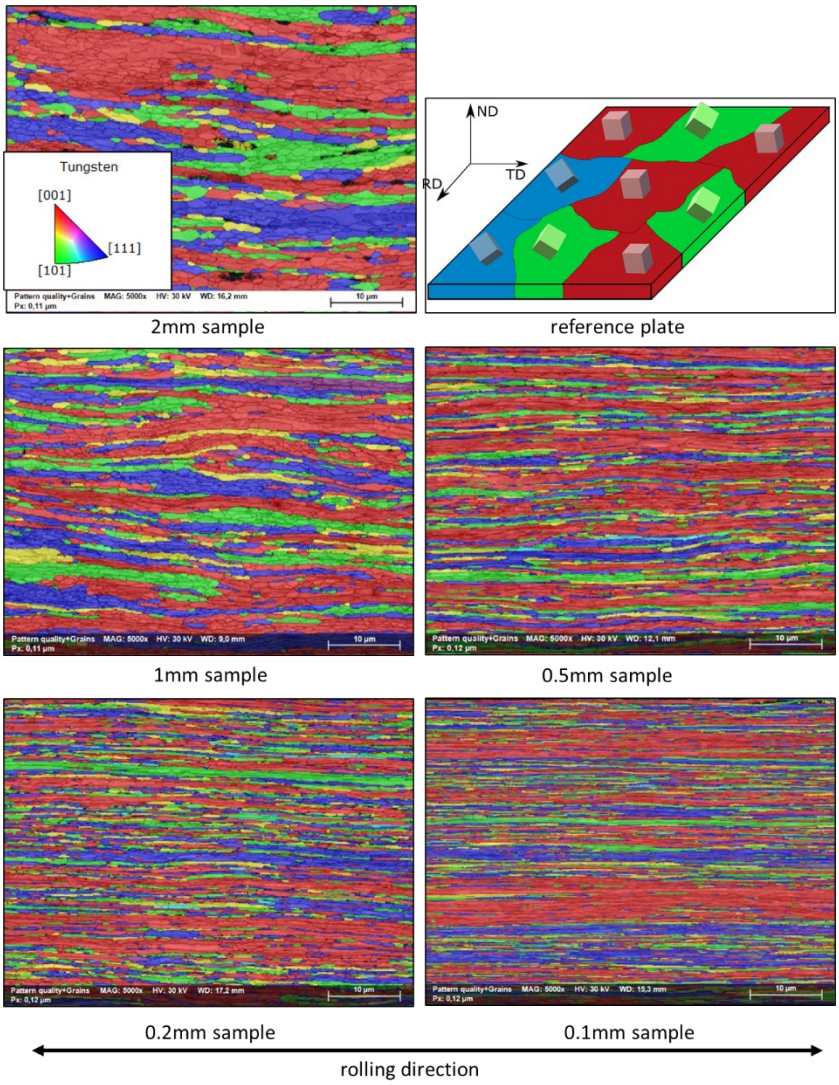

Figure 5.1: IPF images used for the grain size determination (unique grain colour with pattern quality map overlay). The images were taken from the side faces (transversal direction) of the materials to get a good impression of the grain shape aspect ratio increasing with the corresponding degree of deformation increasing. *name of the corresponding overlay in the EBSD software.*

The grain size determined for two reasons may depend on the magnification used. On the one hand there might simply be unsatisfactory statistics due to fewer grains counted at higher magnification and on the other hand there is a tendency, with higher magnifications to cut out and disregard larger grains. For this reason, for the determination of grain size the magnification for each scan used (or for each material used, respectively) was kept fixed to 5k, and the statistics of the number of grains examined is given in the table of the respective grain sizes (table 5.1), too. Furthermore, the orientation of the scanned surface with respect to the rolling direction of the sample has an influence on the grain size, as being observable in the figures 5.3. till 5.7. in the next chapter. The results obtained for the grain size are

influenced as well by the parameters chosen for grain-and-grain boundary-definition. For example, how many pixels does a grain have to cover in order to be recognized as a grain? Are grains located in part only within the examination frame included or are they excluded? What degree of misorientation angle has to be chosen to define separate grains? The decision addressed last heavily affects the total number of grains counted, as the scanned W materials show a pronounced tendency towards subgrain formation. In case of different methods or parameters used clearly deviating results for the grain sizes determined are to be expected. For all the reasons explained above, the grain size determination in this thesis for all samples was carried out using the same software parameters, the same magnification, the same misorientation angle of 15° (concordant to the definition of large angle grain boundary predominantly used) and taken from the same corresponding surface orientation. Figure 5.2 illustrates the correlation between the misorientation angle and the resulting grain size. For this example, the grain size was determined for the top side (normal direction) of the 1 mm material with a magnification of 1k, the misorientation angle ranging from 5° to 15°. A linear increase of grain size with the misorientation angle increasing is assumed, the peak at 13° is due to larger grains at the edges of the scan which were not taken into account anymore.

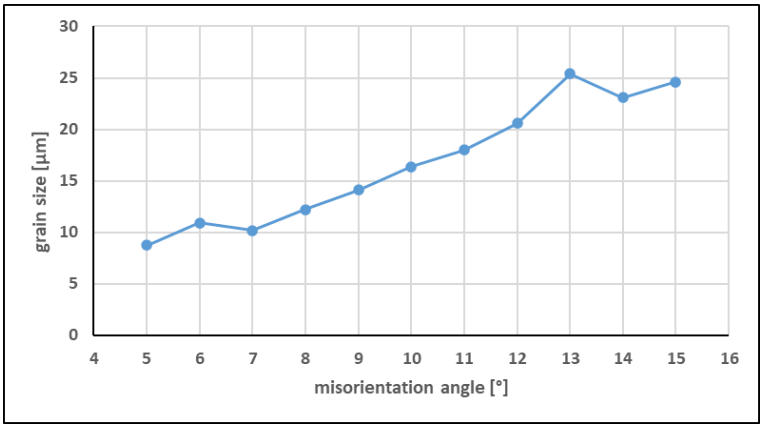

Figure: 5.2: Effect of the misorientation angle and the grain size determined on an 1 mm sample from top view.

.

5.1.2. Overview on the microstructures of the materials investigated

The figures following (figure 5.3 to figure 5.7) present the results of the microstructural analysis for each side of all five materials examined. Frame (b) in each figure displays the scan in the normal direction (ND), frame (c) in the transversal direction (TD) and frame (d) in the rolling direction (RD). Each scan was taken at a magnification of 5k and illustrates the microstructure of the sample examined, this has been achieved by depicting an orientation map indicating the out-of-plane orientation of the grains, associated with a pattern quality map overlay. Frame (a) for the 2 mm material (figure 5.3.) sketches a reference sample, giving a visualization of the different directions. For all the samples following (figure 5.4. to figure 5.7.) frame (a) presents a reference image of the surface in normal direction without any map overlay.

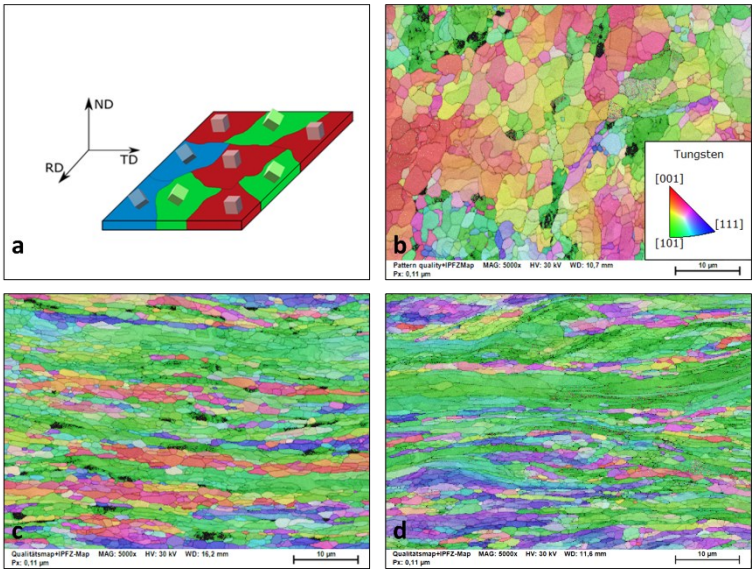

Figure 5.3: EBSD results of the microstructural analysis of the 2 mm sample, with all scans taken at 5k magnification; a) reference sample with definition of directions; b) scan in normal direction (ND); c) scan in transversal direction (TD); d) scan in rolling direction (RD).

The microstructural analysis of the 2 mm materials scanned in RD and TD already exhibits a slightly pronounced rolling texture within some areas, whereas in the scan in ND no pronounced preferred crystal orientation is recognized.

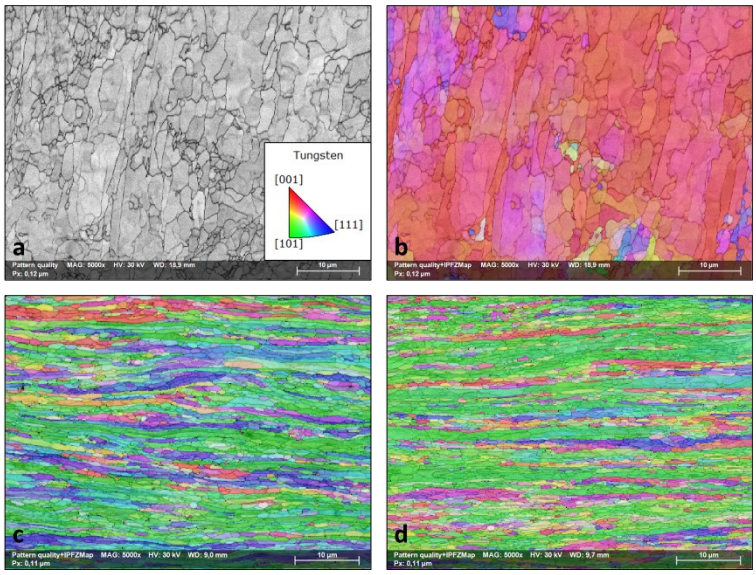

Figure 5.4: EBSD results of the microstructural analysis of the 1 mm sample, with all scans taken at 5k magnification; a) reference image of the surface in ND; b) scan in ND; c) scan in TD; d) scan in RD.

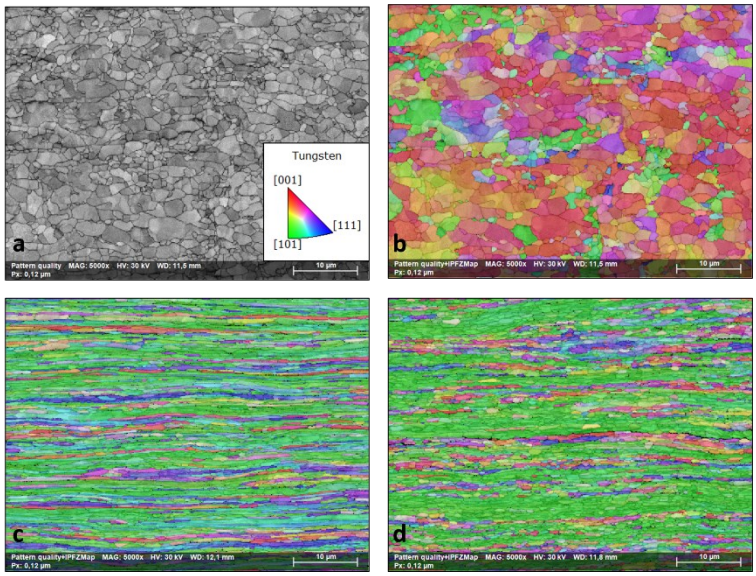

Figure 5.5: EBSD results of the microstructural analysis of the 0.5 mm sample, with all scans taken at 5k magnification; a) reference image of the surface in ND; b) scan in ND; c) scan in TD; d) scan in RD.

In the scans given in figure 5.4 and 5.5, displaying the EBSD scans of the 1 mm and the 0.5 mm material, the forming and development of a pancake-shaped microstructure can be recognized. Due to the rolling performed, with increasing degree of deformation the grains were elongated preferably into RD, though to some share into TD as well, developing a grain structure which resembles stacked pancakes.

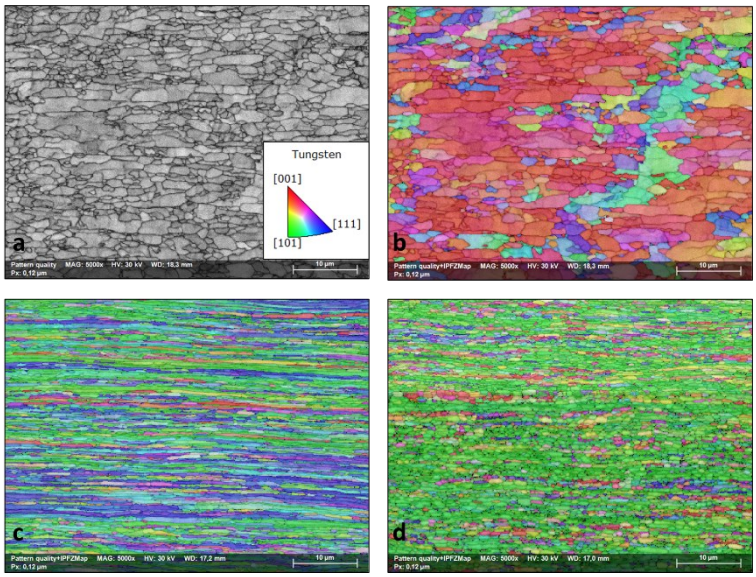

Figure 5.6: EBSD results of the microstructural analysis of the 0.2 mm sample, with all scans taken at 5k magnification; a) reference image of the surface in ND; b) scan in ND; c) scan in TD; d) scan in RD.

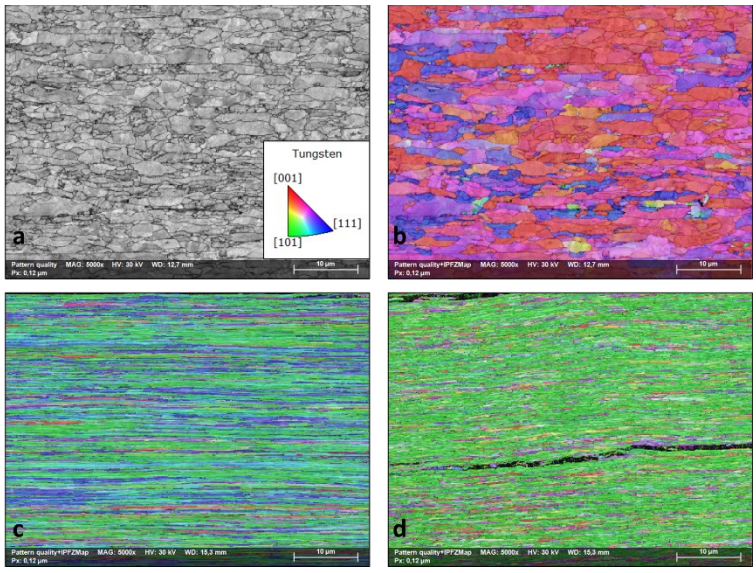

Figure 5.7: EBSD results of the microstructural analysis of the 0.1 mm sample, with all scans taken at 5k magnification; a) reference image of the surface in ND; b) scan in ND; c) scan in TD; d) scan in RD.

Comparison of the EBSD scans arranged in decreasing order of the sample thickness, i.e. from starting with the 2 mm material down to the 0.1 mm materials reveals forming of a rolling texture increasingly pronounced with increasing degree of deformation. These elongated, pancake-shaped grains in case of the investigated samples will act as some kind of crack divider, with the crack branching along different grain boundaries, and thus leading to delamination and increased fracture toughness.

5.1.3. Texture development

The increasingly pronounced texture addressed above can be visualized by means of stereographic projections. Each grain and its orientation is represented in a statistics counting conformity regarding orientation, the results have been summarized and colour-coded into three directions of crystallography planes. Figure 5.8 demonstrates that the development of a texture is more pronounced with the increasing of grade of deformation. While only a weak texture can be recognized in the 1 mm sample, the strength of texture significantly increases the thinner the material gets, until the 0.1 mm sample exhibits a texture extremely pronounced (rotated cube texture).

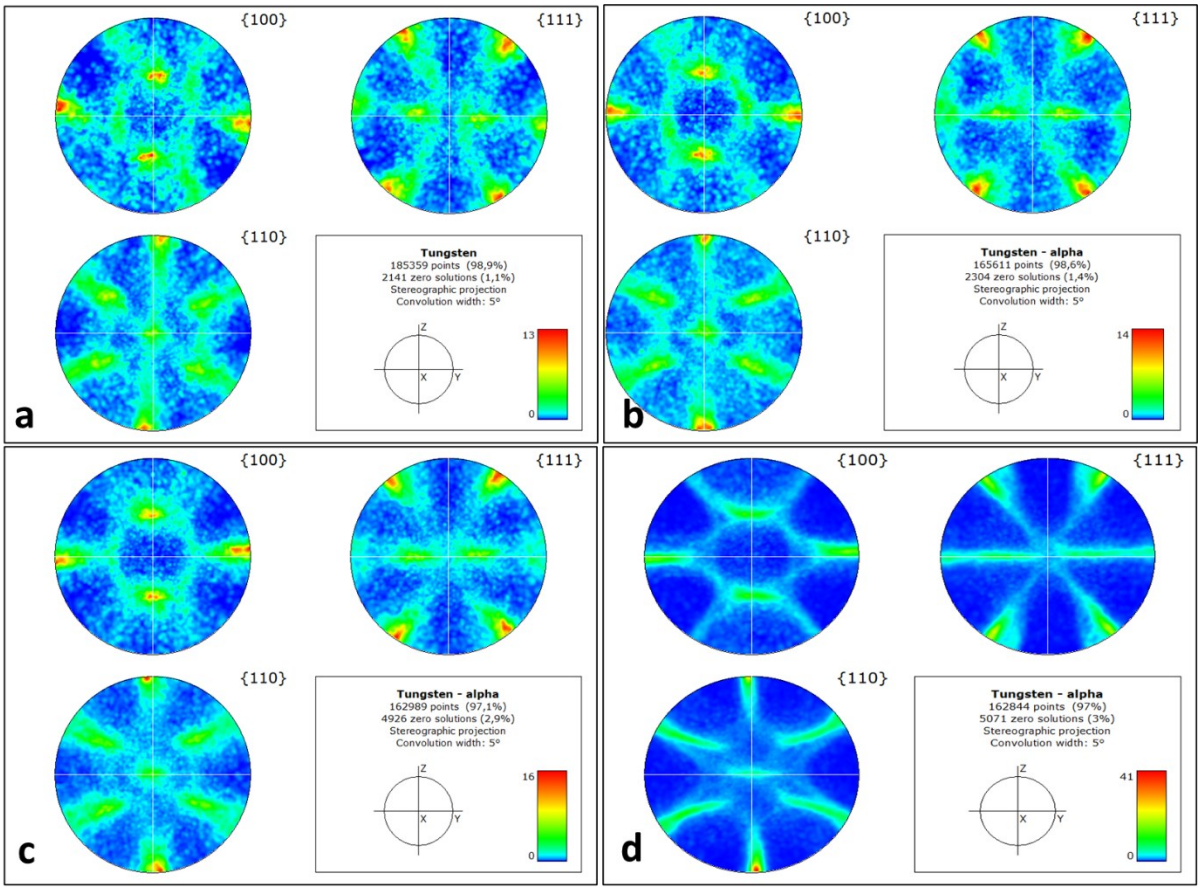

Figure 5.8: Survey of the texture development of the materials tested a) 1 mm material b) 0.5 mm material c) 0.2 mm material d) 0.1 mm material. Pay attention to the change in colour code used to describe the texture of the particular samples. Higher numbers describe stronger texture, but may be colour-coded differently.

5.2. Fracture toughness and R-curve experiments, including fractography

This chapter starts with the presentation of the results of the conditional fracture toughness and R-curve experiments performed for each material, including the micrographs of the fracture surfaces taken with the SEM. Subsequently a comparison between the different materials will be given, followed by a discussion of the results of the fracture toughness and R-curve experiments and a presentation of the results of the so called 80 % experiments described in chapter 5.3. As addressed already in chapter 2.1, due the unavoidable constrains on sample dimensions the samples tested did not meet the size requirements given by the ASTM E399 [Eq.2.6]. Furthermore, in order to be able at all to record the crack extension of quickly growing cracks the requirements regarding the loading rate given by the ASTM E399 were neglected and much lower loading rates were chosen. Consequently all results obtained for fracture toughness in this thesis must not be specified as fracture toughness K_{IC} but as conditional fracture toughness K_q. In order to approximate the requirements of the ASTM E399 as close as possible despite all the issues regarding testing the materials described in chapter 4.3, the samples were tested as described in chapter 4.3.7 by methods as comparable as possible. The method of measuring the potential and the change in potential never altered throughout all the experiments. What had to be adjusted was the way of supplying the current to the samples and the mounting of the sample in the linkage.

5.2.1. Results for the 2 mm samples

As described in chapter 4.3.4 in case of the 2 mm samples a current of 9 A was applied through pins on the front side of the sample. The thickness B of the sample was measured with a micrometre screw, the distance 2λ was measured with a calliper rule and the starting crack length a_0 was determined with the LIMI. The conditional fracture toughness K_q and the geometry factor f(a/W) were calculated according to Cravero [37] [Eq.5.2 and Eq.5.3] for a pinned sample with a fixed crack length a_0. For the R-curves corresponding (given some pages further below in figure 5.10) the calculations considered the current crack length a ($a=a_0+\Delta a$) at the respective load. An increased fracture toughness was to be observed in any case a crack extension Δa could be measured at all.

The value of the crack extension Δa was obtained by means of the Johnson-Equation ([Eq.2.8] chapter 2.3). The calculation was carried out for a measured potential U, the initial potential difference U_0 was fixed to be the average potential of the 5 to 15-minutes waiting period before every test. In order to consider the preload applied to the sample, the zero-level load P_0 (which has been determined after complete fracture) had to be subtracted from the load P_{appl} applied. As an example, for the 2_10 mm sample P_{appl} was 1251 N and the zero-level load P_0 was -55 N. For calculation of the conditional fracture toughness K_q the maximum force was used. The sample width W for all 2 mm samples tested was 10 mm. The calculation for the sample 10_2 mm is given below.

$$K_q = \frac{P}{B * \sqrt{W}} * f\left(\frac{a}{W}\right) \qquad \text{[Eq.5.2]}$$

$$f\left(\frac{a}{W}\right) = -0.0720 + 11.6294 * \left(\frac{a}{W}\right) - 61.6928 * \left(\frac{a}{W}\right)^2 + 223.4007 * \left(\frac{a}{W}\right)^3 - 355.5166 * \left(\frac{a}{W}\right)^4 + 239.3969 * \left(\frac{a}{W}\right)^5 \qquad \text{[Eq.5.3]}$$

$$f\left(\frac{a}{W}\right) = -0.0720 + 11.6294 * \left(\frac{4.777}{10}\right) - 61.6928 * \left(\frac{4.777}{10}\right)^2 + 223.4007 * \left(\frac{4.777}{10}\right)^3 - 355.5166 * \left(\frac{4.777}{10}\right)^4 + 239.3969 * \left(\frac{4.777}{10}\right)^5 = 3.2$$

$$K_q = \frac{(1251N - (-55N))}{\frac{1.76}{1000}m * \sqrt{\frac{10}{1000}m}} * 3.2 = 23.8\ MPa\sqrt{m}$$

Table 5.2 for the 2 mm samples tested gives the values of the conditional fracture toughness K_q, the corresponding testing parameters (testing temperature T and testing speed v), and the acquired data of the samples. The thickness of the samples 2 mm, 1 mm, and 0.5 mm actually was slightly smaller than the nominal one, this being due to the sample preparation unavoidable, i.e. grinding and polishing the side surfaces for making the introduced pre-crack visible. All results presented in this chapter originate from experiments conducted by use of the experimental set-up II described in chapter 4.3.7.

Table 5.2: Testing parameters and data obtained for the 2mm samples tested.

Sample	T [°C]	v [µm/min]	2λ [mm]	B [mm]	a [mm]	P [N]	Δa [µm]	K_q [MPa√m]
10_2mm	RT	20	1.0	1.76	4.777	1306	-	23.8
11_2mm	RT	200	1.2	1.65	4.792	863	-	16.8
12_2mm	200	200	1.3	1.79	4.746	3348	556	59.1

As discussed in chapter 4.3.7 the maximum loading rate (i.e. the speed of the crosshead movement) has already once been reduced when changing the experimental set-up from #I to #II, i.e. changing the testing speed from 400 µm/min to 200 µm/min in order to enable the nanovoltmeter to measure the consecutive change in potential with an increased resolution. After a few tests not obtaining any R-curve behaviour at RT (e.g. Sample 11_2 mm) and in order to test whether this was an issue with the resolution of the nanovoltmeter, the test speed was further reduced to 20 µm/min. Even at this slow testing speed this material did not show any R-curve behaviour (Sample 10_2 mm) at RT. The figures 5.9, 5.10, and 5.11 depict the original load-potential curves, as recorded from experimental set-up II, and images of the associated fracture surfaces taken with the SEM are shown. The red line represents the measured potential and the black one the force on the sample. For both samples tested at RT the fracture surfaces (Figures 5.9 and 5.10) show brittle transcrystalline fracture with little to no stable crack extension.

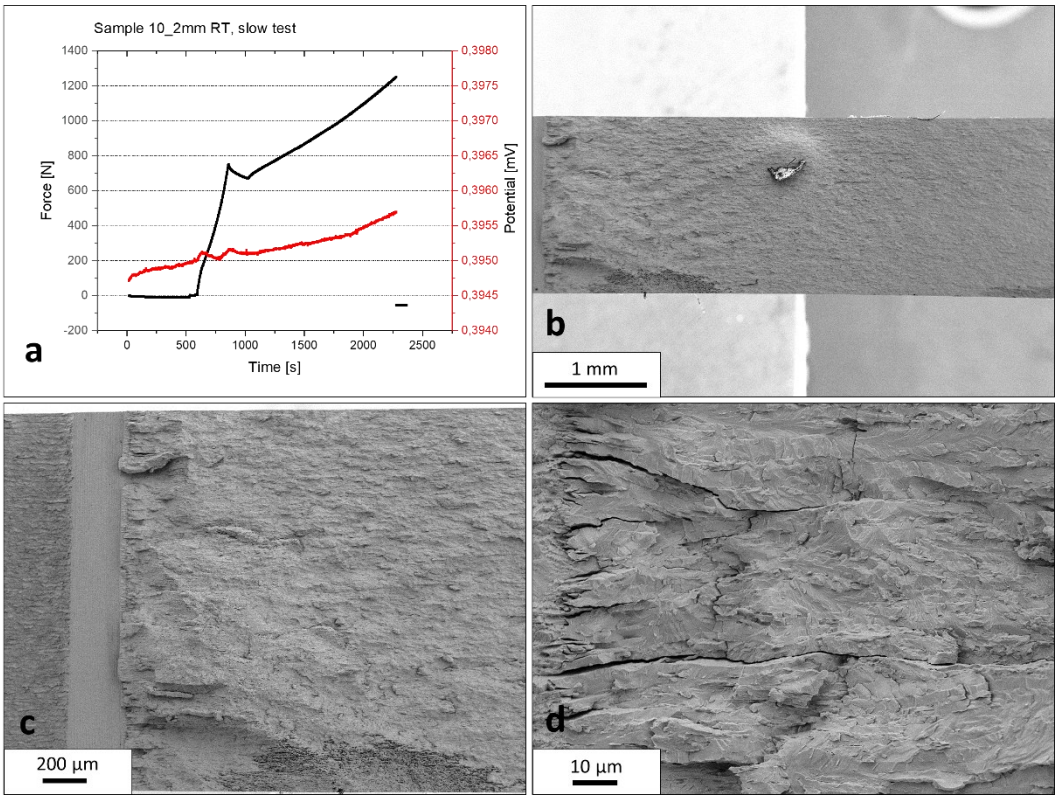

Figure 5.9: a) Load-potential curve of sample 10_2 mm tested at RT with 20 µm/min; b) fracture surface overview; c) starting crack overview; d) early crack extension in detail.

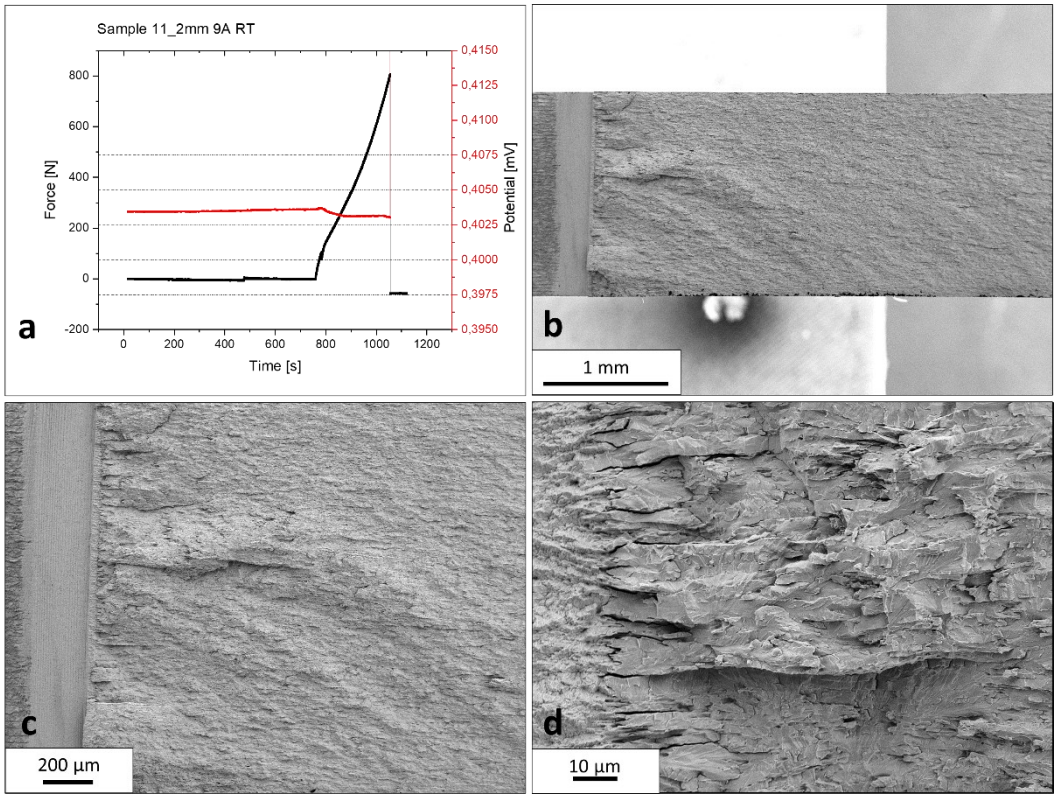

Figure 5.10: a) Load-potential curve of sample 11_2 mm tested at RT with 200 µm/min; b) fracture surface overview; c) starting crack overview; d) early crack extension in detail.

Contrary to the RT tests, the 2 mm sample at 200 °C clearly shows an R-curve behaviour. The two drops in the loading curve in figure 5.11a are due to both bolts breaking under load one after the other. Because of the broken bolts wedging the test fortunately could be continued. As the potential measured did show just a small drop in course of the second bolt failing, the potential measurement was considered to be valid. Furthermore, the potential increasing at the end of the experiment fits very well to the fracture surface observed in the SEM. In contrast to the fracture images of the samples tested at RT, the figures 5.11 b,c,d of the fracture surfaces of the sample tested at 200 °C show crack extension in form of delamination within the plane of the plate. In figure 5.11b on the left the FIB-introduced pre-crack can be recognized, adjacent to the crack extension by delamination. Furthermore, a deviation of the crack path under an angle of 45° can be seen. This deviation is accompanied by a transition from delamination to transcrystalline brittle fracture, where the sample finally failed critically. Figures 5.11c,d give more details of the delamination region and the region of transition from delamination to brittle failure.

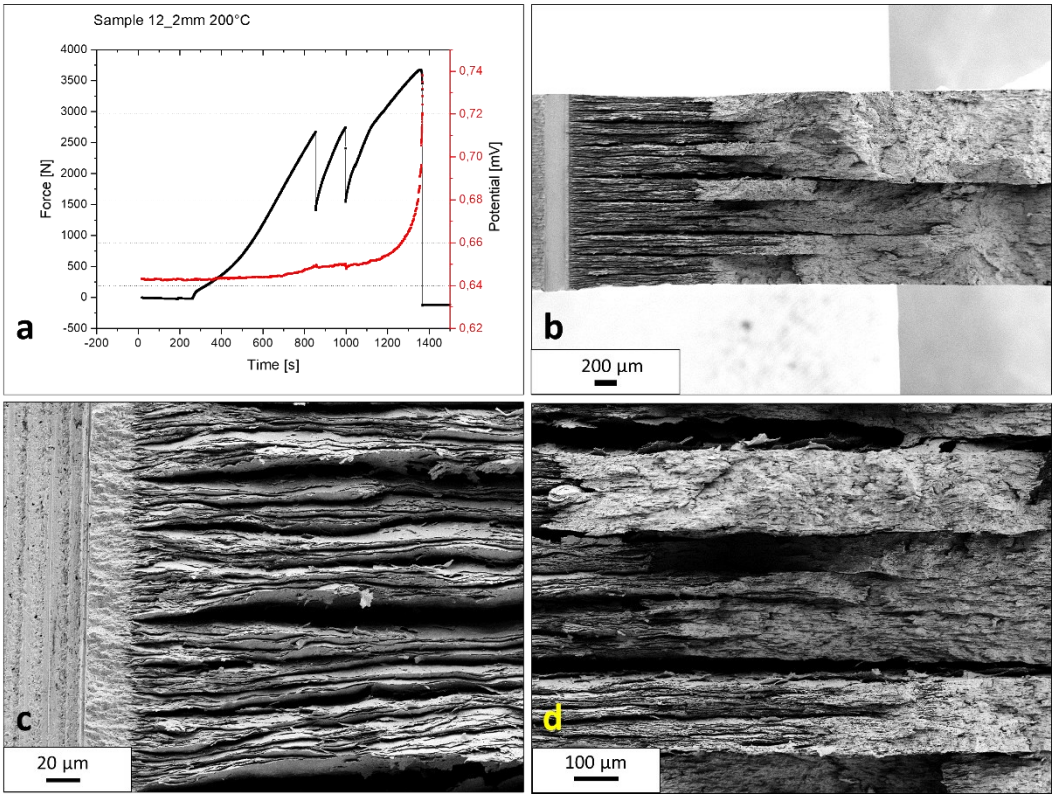

Figure 5.11: a) Load-potential curve of sample 12_2 mm tested at 200 °C with 200 µm/min. The two drops in force are due to the bolts failing. The potential shows just a slight drop at the moment the second bolt failed; b) fracture surface overview; c) starting crack overview region of early stable crack extension; d) crack extension in detail in the transition to the cleavage mode.

Figure 5.12 is a presentation of the results of the R-curve measurements of all samples of the 2 mm material. The red curve represents the 200 °C tested sample, the green line shows the sample tested slowly at RT and the blue line the sample tested at RT with standard testing speed of 200 µm/min.

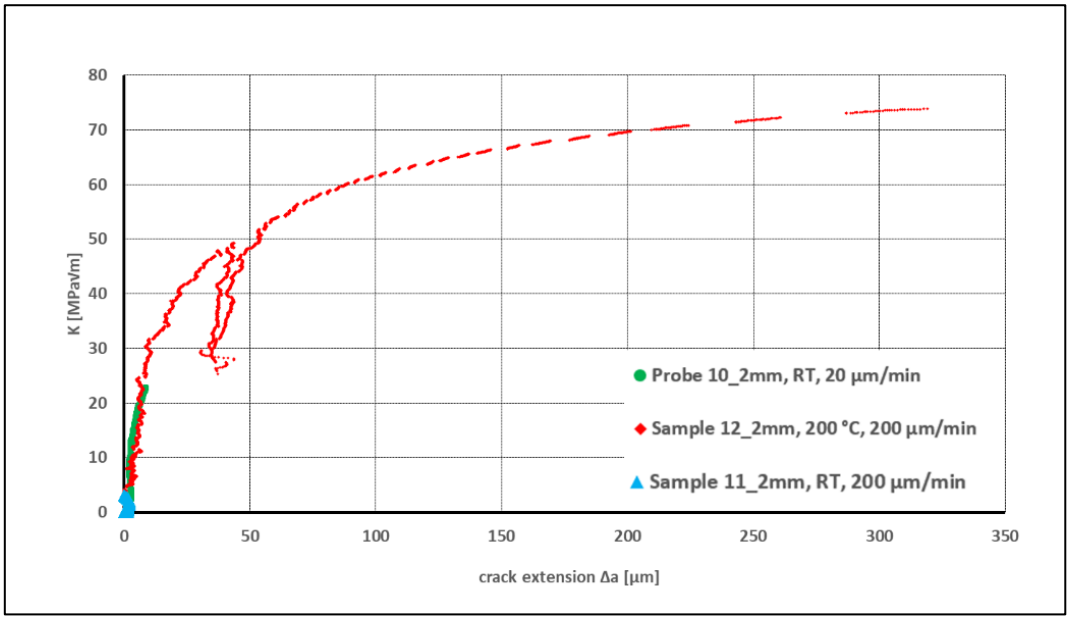

Figure 5.12: Presentation of the R-curves obtained, given for all samples of the 2 mm material. The drop in the R-curve for sample 12_2 mm is caused by both bolts breaking during the experiment.

5.2.2. Results for the 1 mm samples

The major modification in the experimental set-up compared to the tests of the 2 mm samples was the new method of applying the power to the samples described in chapter 4.3.4 (experimental set-up II), permitting a current applied sufficiently high to provide an increase in potential now being large enough to detect and measure a relative small crack extension Δa. The maximum limit for the current applicable was found out to be 6 A, any current higher led to a significant heating of the wires, interfering with the accuracy of the potential measurement. For testing and calculating the conditional fracture toughness K_q and the crack extension Δa of the 1 mm samples no further changes in the set-up compared to the tests of the 2 mm samples (described in chapter 5.2.1) were necessary. The sample width W for all 1 mm samples was 10 mm. The values of the conditional fracture toughness K_q, the corresponding testing parameters (testing temperature T and testing speed v) and the data acquired for the 1 mm samples are given in table 5.3.

Table 5.3: Testing parameters and data obtained for the 1mm samples tested.

Sample	T [°C]	v [µm/min]	2λ [mm]	B [mm]	a [mm]	P [N]	Δa [µm]	Kq [MPa√m]
1_1mm	RT	20	1.4	0,91	4.876	1243	70	45.7
2_1mm	RT	200	2.0	0,86	4.874	1327	20	51.7
3_1mm	200	200	1.8	0,85	4.761	1828	789	68.1

The load-potential graphs from the measurements and the corresponding fracture surfaces obtained from the SEM are shown in the figures 5.13 – 5.15.

Alike the 2 mm samples at RT, neither the 1 mm samples at RT exhibited a pronounced R-curve behaviour (figure 5.13a), only a few µm of crack extension Δa could be measured.

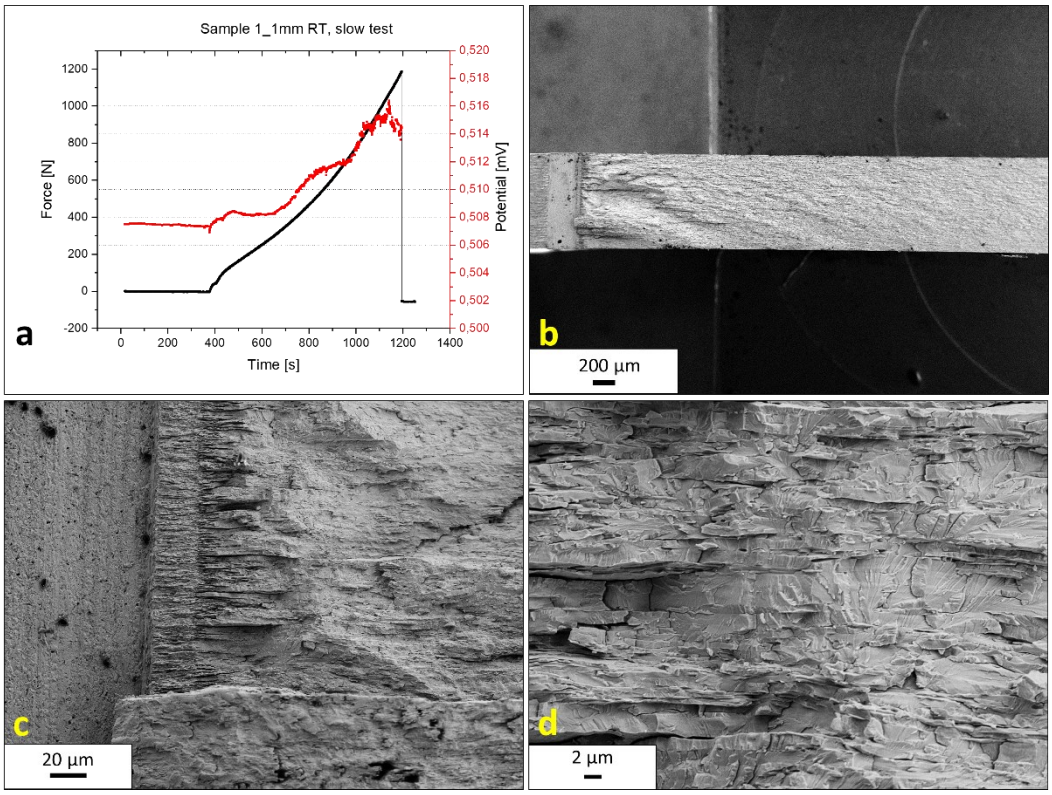

Figure 5.13: a) Load-potential curve of sample 1_1 mm tested a RT with 20 µm/min; b) fracture surface overview; c) starting crack overview; d) detailed view on the fracture surface, mixed transcrystalline (river patterns) and intercrystalline fracture.

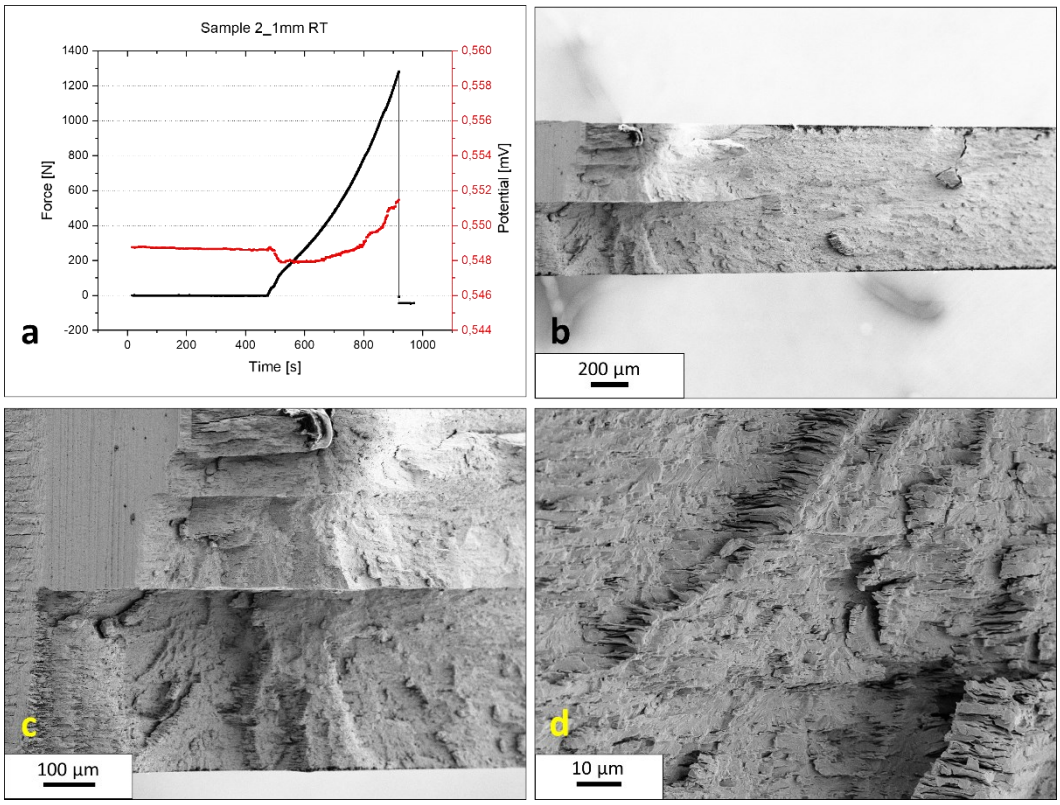

Figure 5.14: a) Load-potential curve of sample 2_1 mm tested at RT with 200 µm/min; b) fracture surface overview; c) starting crack overview, crack splits +45° and -45° in regard of the expected crack propagation plane, notch plane respectively; d) crack extension in detail.

The potential-force graph of sample 3_1 mm at 200 °C, did show an unusual behaviour (figure 5.15a), resulting in the serrated R-curve displayed in figure 5.17. The corresponding fracture surfaces may explain the unusual effects observed. In the image in figure 5.15 b,c micrographs of both halves of the fractured sample are shown. At one half a regular crack extension seems to have taken place, but at closer inspection on one side of the sample some part of the crack front proceeded further than the majority of the other cracks. For the share of the crack front remaining some contact could have happened, as long as the crack did not growth through completely.

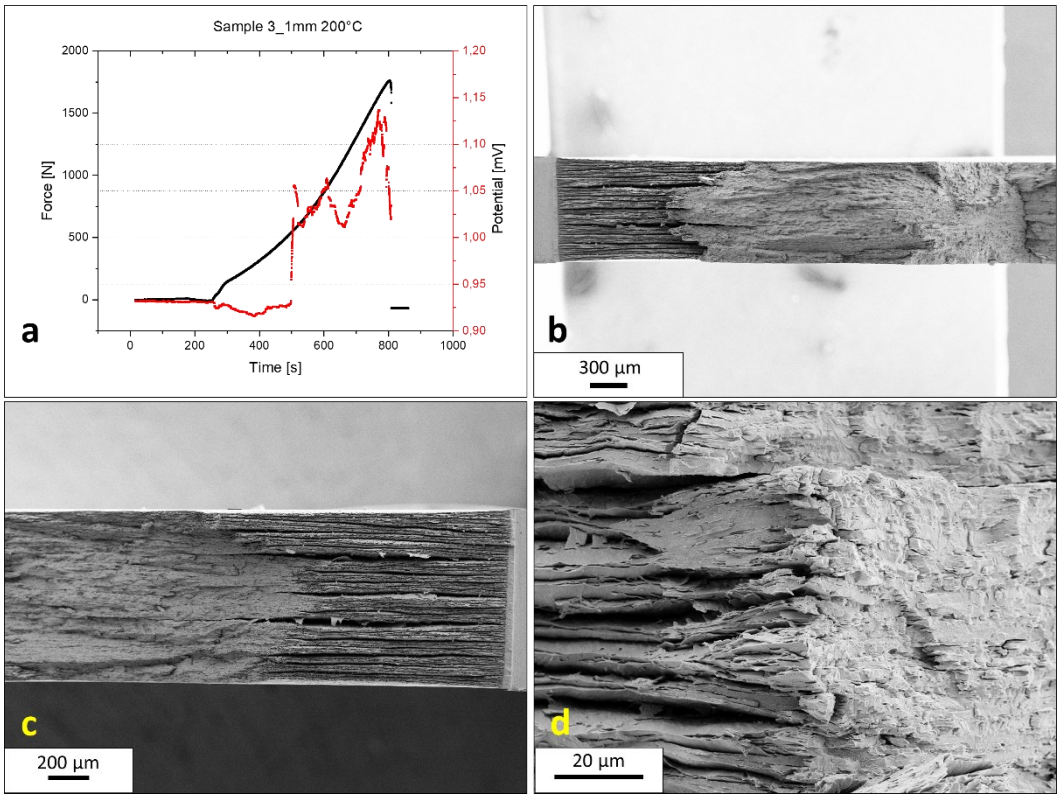

Figure 5.15: a) Load-Potential curve of sample 3_1 mm tested at 200 °C with 200 µm/min; b) transition from delamination to brittle fracture; c) fracture surface overview, fracture surface I; d) fracture surface overview, fracture surface II.

Two different kinds of fracture behaviour can be observed at the samples in figure 5.16. The two samples tested at RT broke under 45° into three pieces. The third sample tested at 200 °C exhibited crack propagation almost within the notch plane. Figure 5.17 provides a summary of the R-curves of all 1 mm samples tested.

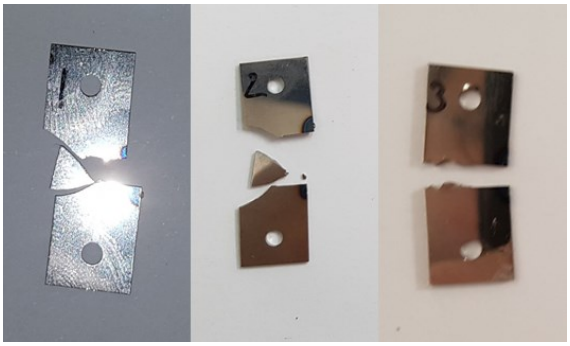

Figure 5.16: Observable differences in fracture behaviour of the 1 mm samples. The two RT samples (1) (2) broke into 3 pieces, fracture for the 200 °C sample occurred along the notch plane. It fractured into 2 pieces.

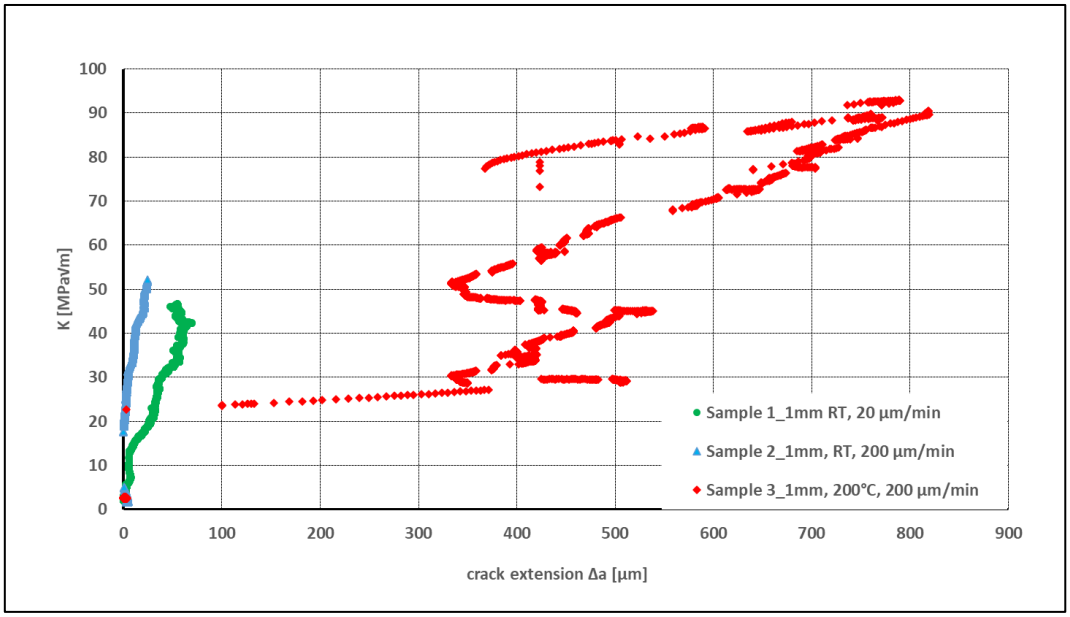

Figure 5.17: Presentation of the R-curves obtained, given for all samples of the 1 mm material. The serrated red curve might be due to the contact area across the partially cracked region changing in the course of the experiment.

5.2.3. Results for the 0.5 mm samples

The design of the current supply used for the 1 mm samples turned out not to be applicable for the 0.5 mm samples (for details see 4.3.4). Due to the modifications necessary the current supply on the samples was limited to 2 A. All the other steps to perform the experiments on the 0.5 mm samples, i.e. how the samples were installed into the experimental set-up, the calculations for the fracture toughness, the geometry factor and the crack extension remained strictly as being applied at the tests of the 2 mm and 1 mm samples. The sample width W for all tested 0.5 mm samples was 10 mm. The testing parameters, data acquired for the 0.5mm samples and the values resulting for the conditional fracture toughness K_q are given in the table 5.4.

Table 5.4: Testing parameters and data acquired for the 0.5mm samples tested.

Sample	T [°C]	v [µm/min]	2λ [mm]	B [mm]	a [mm]	P [N]	Δa [µm]	Kq [MPa√m]
1_0.5mm	RT	200	3.0	0.43	4.741	645	22	47.4
2_0.5mm	RT	20	1.6	0.43	4.791	889	98	67.3
3_0.5mm	200	200	1.7	0.46	4.809	974	421	69.2

The load-potential graphs and micrographs of fracture surfaces corresponding are presented in the figures (5.18-5.20). Like all samples tested so far at RT, the 1_0.5 mm sample tested at RT with a testing speed of 200 µm/min did not show an R-curve behaviour. In the images of the fracture surfaces (5.18, 5.19) hardly any crack extension or delamination can be seen, instead of this brittle fracture under 45° occurred.

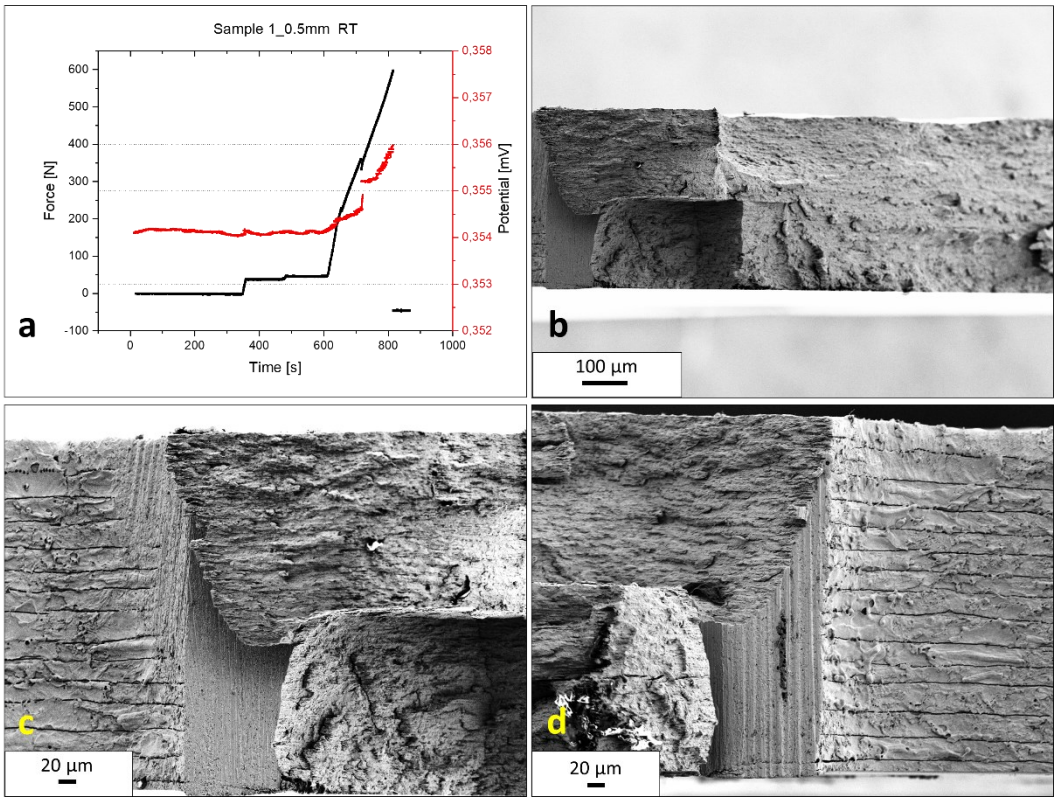

Figure 5.18: a) Load-Potential curve of sample 1_0.5 mm tested at RT and 200 µm/min; b) fracture surface overview; c) starting crack on fracture surface I; d) starting crack on fracture surface II.

The 2_0.5 mm sample tested at RT, but with a testing speed of just 20 µm/min showed a behaviour completely different compared to all samples tested at RT so far. The potential for the first time clearly ascended at RT, as displayed in the potential-load curve in figure 5.19a. The corresponding fracture surfaces depicted in the figures 5.19b-d clearly exhibit delamination. The ligament remaining after stable crack extension by delamination fractured brittle under 45°. Concordant to the ascending potential the 2_0.5 mm sample tested at RT showed an R-curve, a behaviour neither observable for thicker samples nor for the sample of same thickness tested at higher testing speed. From those facts reported it can be deduced that by the refinement of the microstructure of the samples the DBTT is lowered to the range of RT and that the fracture behaviour – as being well known to hold for most bcc metal – is dependent on the loading speed.

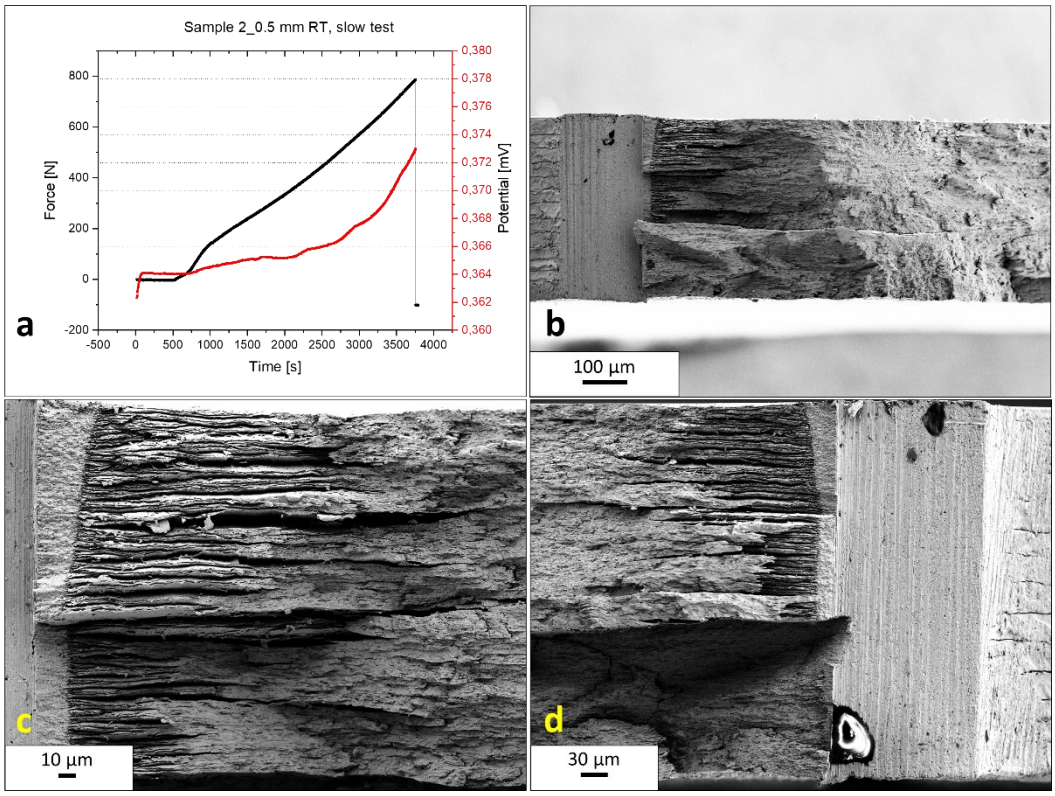

Figure 5.19: a) Load-potential curve of sample 2_0.5 mm tested at RT with 20 µm/min; b) fracture surface overview, for the first time showing delamination at RT; c) fracture surface I: transtion from delamination to brittle fracture; d) fracture surface II: transtion from delamination to brittle fracture.

Concordant to the results obtained from the 0.5 mm samples tested at RT and a testing speed of 20 µm/min, the sample 3_0.5 mm tested at 200 °C exhibits R-curve behaviour too, as shown in figure 5.20. However, there is an important difference to the thicker samples tested at 200 °C, as this sample did show a different behaviour. The fracture surfaces exclusively show delamination without any sign of brittle fracture. All thinner samples examined at 200 °C, i.e. the 0.2 mm and the 0.1 mm samples presented a fracture behaviour strictly identical to this.

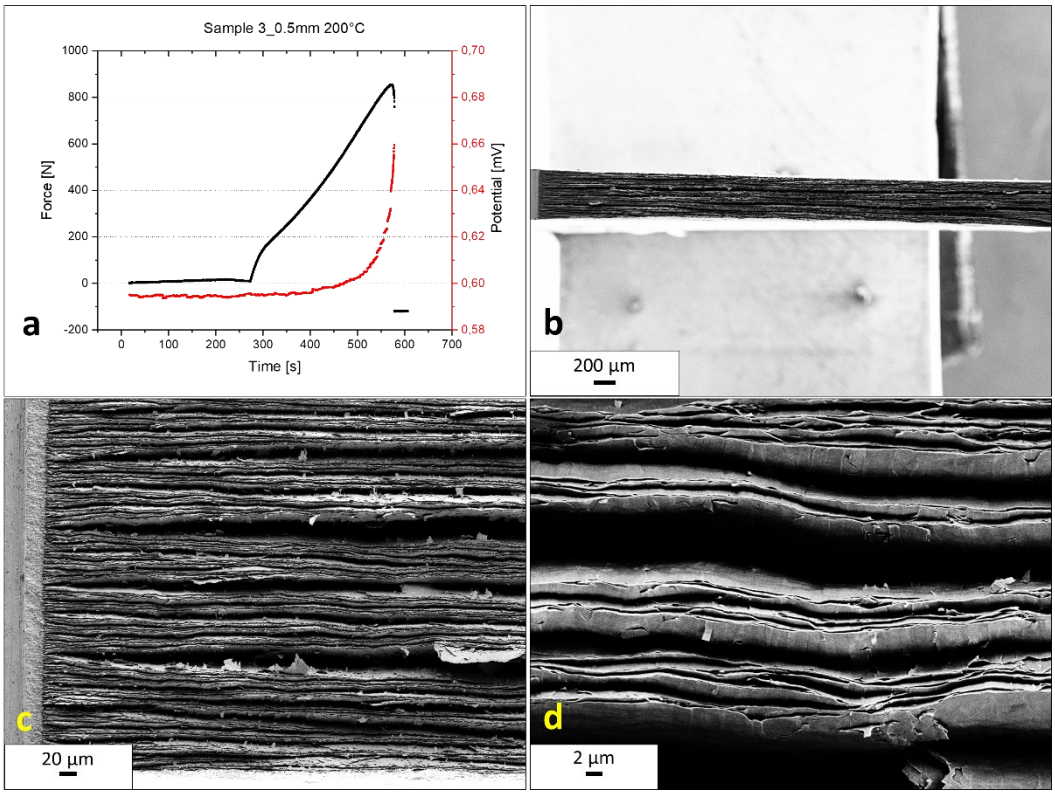

Figure 5.20: a) Load-Potential curve of sample 3_0.5 mm tested at 200 °C with 200 µm/min; b) fracture surface overview, pure delamination; c) starting crack fracture surface I; d) view on the delamination further zoomed in.

Two kinds of fracture behaviour can be observed at the samples in figure 5.21. Both samples tested at RT failed under 45° into three pieces. The third sample tested at 200 °C showed plane fracture along the notch plane. Figure 5.22 provides a summary of R-curves of all 0.5 mm samples examined.

Figure 5.21: Left: sample tesed at RT; Right: sample tested at 200 °C.

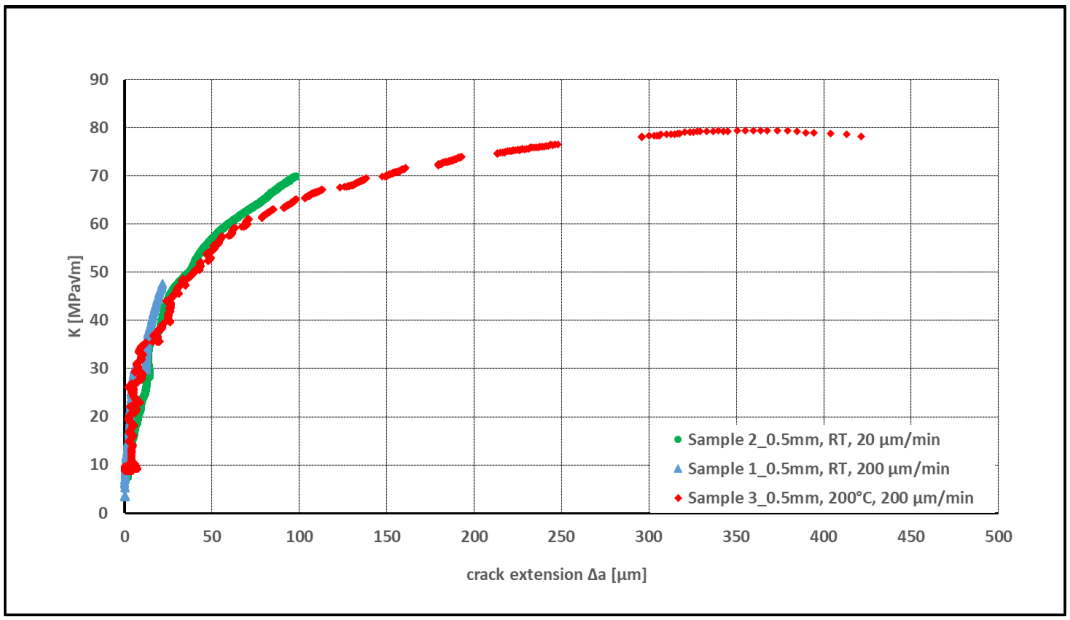

Figure 5.22: Presentation of the R-curves obtained, given for all samples of the 0.5 mm material.

5.2.4. Results for the 0.2 mm samples

Some major modifications to the experimental set up II and to the design of the samples were necessary to be able to perform tests on the 0.2 mm and 0.1 mm (for details: chapter 4.3.5.). The sample width W was reduced to 5 mm. Due to the altered configuration in order to apply the load, the calculations of the conditional fracture toughness K_q and of the geometry factor f(a/W) now had to be performed according to Murakami [33] [Eq.5.4 and Eq. 5.5] instead of according to Cravero [37]. The main difference is that [37] performs the calculation according to pin loading whereas [33] assumes stressing the sample along the whole width. Differences are minor and were found to be approximately 1 %. The calculations for the crack extension Δa were still performed following the Johnson Equation. As an example, calculation for the sample 1_0.2 mm is shown below.

$$K_q = \frac{P}{B*W} * \sqrt{\pi * a} * f\left(\frac{a}{W}\right) \qquad \text{[Eq.5.4]}$$

$$f\left(\frac{a}{W}\right) = 1.12 - 0.231 * \left(\frac{a}{W}\right) + 10.55 * \left(\frac{a}{W}\right)^2 - 21.72 * \left(\frac{a}{W}\right)^3 + 30.39 * \left(\frac{a}{W}\right)^4 \text{[Eq. 5.5]}$$

$$f\left(\frac{a}{W}\right) = 1.12 - 0.231 * \left(\frac{1.096}{5}\right) + 10.55 * \left(\frac{1.096}{5}\right)^2 - 21.72 * \left(\frac{1.096}{5}\right)^3 + 30.39 * \left(\frac{1.096}{5}\right)^4 = 1.418$$

$$K_q = \frac{678N}{0.20mm * 5mm} * \sqrt{\pi * \frac{1.096}{1000} m} * 1.418 = 56.4MPa\sqrt{m}$$

Tests with a slower testing speed were no longer performed, due to the fact that the samples already showed an R-curve behaviour at RT and at normal testing speed of 200 µm/min. For each temperature two tests were carried out. Table 5.5 shows the testing parameters, the data obtained and the results for all 0.2 mm samples tested. Important to note for calculation and for interpretation of the results, the sample dimensions have changed. The sample width W was reduced from 10 mm to 5 mm. The actual thickness of the 0.2 mm and 0.1 mm samples now coincided with their nominal thickness B, due to surface preparations not being necessary any longer.

Table 5.5: Testing parameters and data acquired for the 0.2 mm samples tested.

Sample	T [°C]	v [µm/min]	2λ [mm]	B [mm]	a [mm]	P [N]	Δa [µm]	Kq [MPa√m]
1_0.2mm	RT	200	2.7	0.20	1.096	678	300	56.4
2_0.2mm	RT	200	3.5	0.20	1.142	649	90	56.0
4_0.2mm	200	200	1.4	0.20	1.118	674	193	57.1
5_0.2mm	200	200	1.6	0.20	1.196	869	138	78.3

Figure 5.23 shows the force-potential curve for sample 1_0.2 mm, the drops in force represent the bolts breaking. The fracture surfaces once more show a mixed fracture, starting with delamination and transition to brittle fracture under 45°.

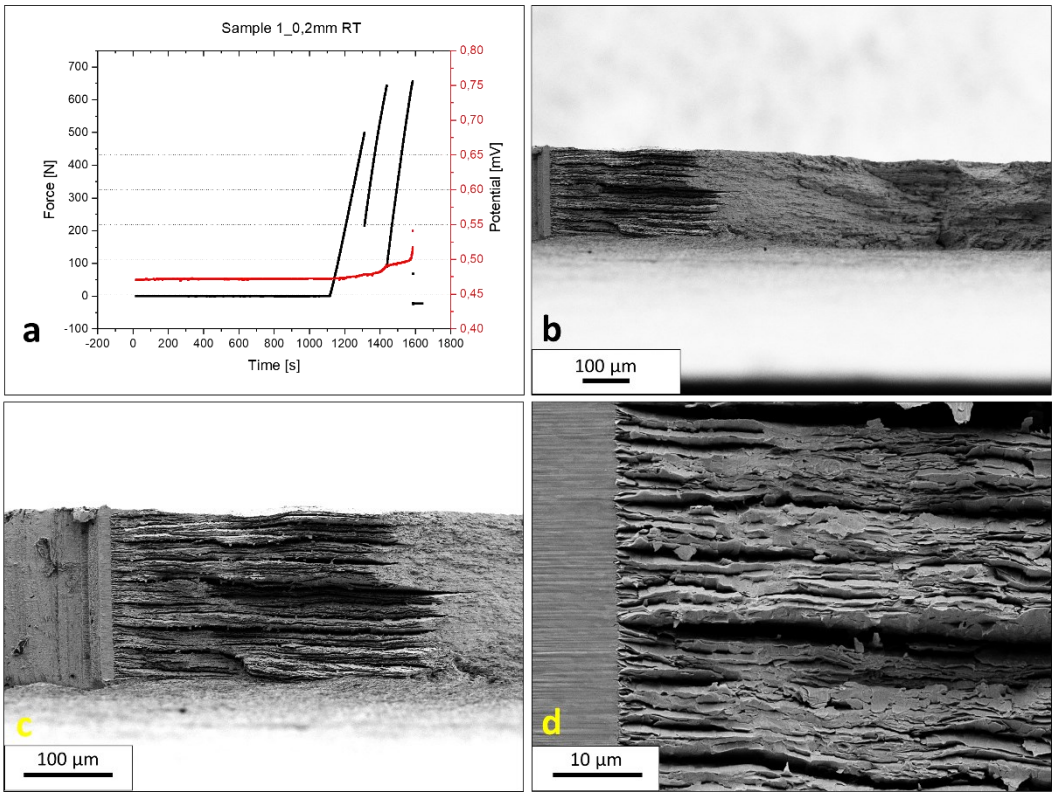

Figure 5.23: a) Load-potential curve of sample 1_0.2 mm tested at RT and 200 µm/min; b) fracture surface overview, delamination mixed with brittle fracture; c) starting crack on fracture surface; d) more detailied view on the starting crack.

Figure 5.24 shows the force-potential curve for sample 2_0.2 mm, where in contrast to sample 1_0.2 mm the bolts did not fail. The fracture surfaces offered a remarkable phenomenon, with a crack dividing into two different fracture planes already in the notch region (probably caused by the sample preparation). The lower crack path shows delamination, whereas the upper one shows more of a brittle facture behaviour. The two samples tested at RT once again broke under 45° into three pieces.

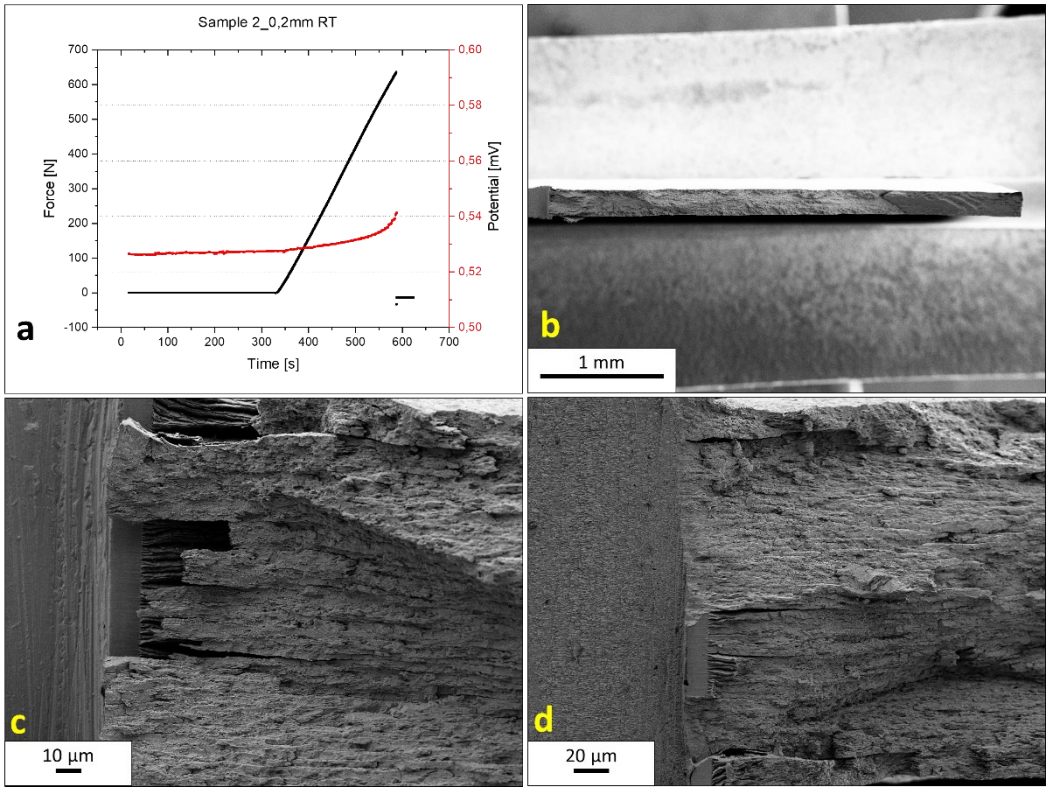

Figure 5.24: a) Load-potential curve of sample 2_0.2 mm tested at RT and 200 µm/min; b) fracture surface overview; c) starting crack fracture surface I; d) starting crack fracture surface II.

Figures 5.25 and 5.26 show the force-potential curves for the samples 4_0.2 mm and 5_0.2 mm tested at 200 °C, adjacent to the corresponding fracture surface images. Once again, the drop in the force for the sample 5_0.2 mm represents the bolts breaking. For both samples, the whole fracture surface shows delamination without any brittle fracture failures.

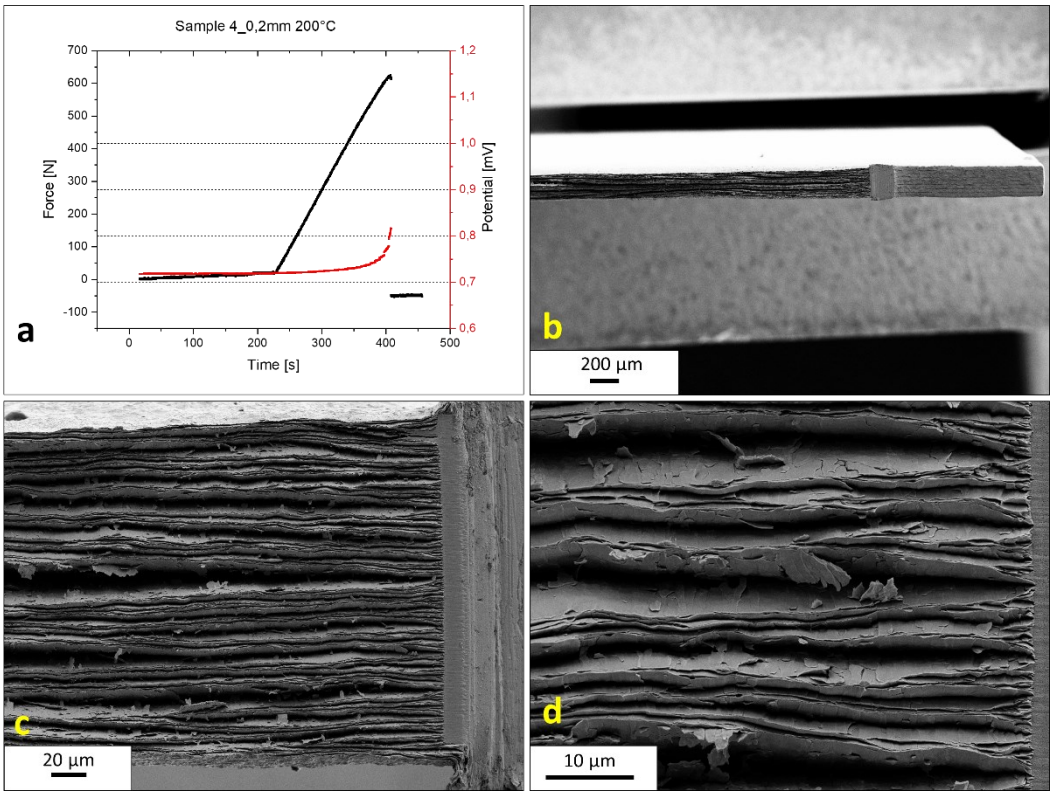

Figure 5.25: a) Load-potential curve of sample 4_0.2 mm tested at 200 °C with 200 µm/min; b) fracture surface overview, pure delamination; c) starting crack fracture surface; d) more detailied view on the starting crack.

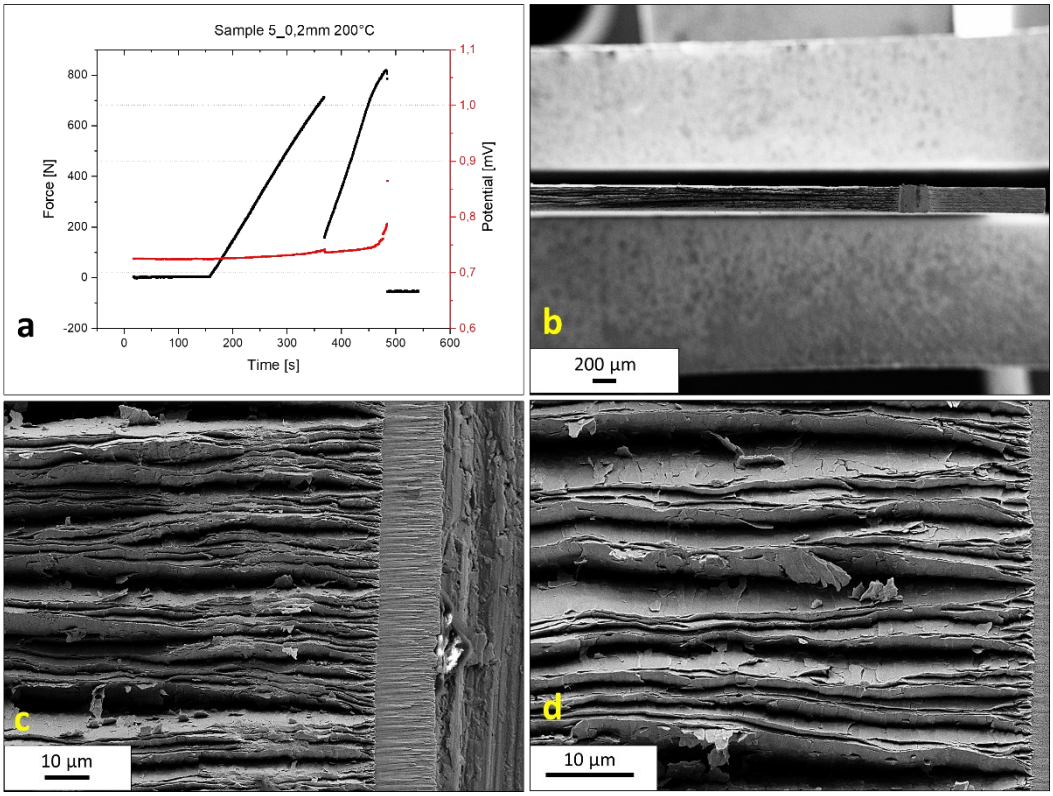

Figure 5.26: a) Load-potential curve of sample 5_0.2 mm at 200 °C and 200 µm/min; b) fracture surface overview, delamination; c) starting crack fracture surface I; d) more detailied view on the starting crack.

Figure 5.27 provides a summary of R-curves of the 0.2 mm samples. There is no pronounced difference in R-curve behaviour between RT and 200 °C tested samples anymore, which indicates that the refined microstructure shifted the DBTT below RT. Figure 5.28 provides R-curves of 0.2 mm samples selected for easier comparability, where the bolts did not break during the test.

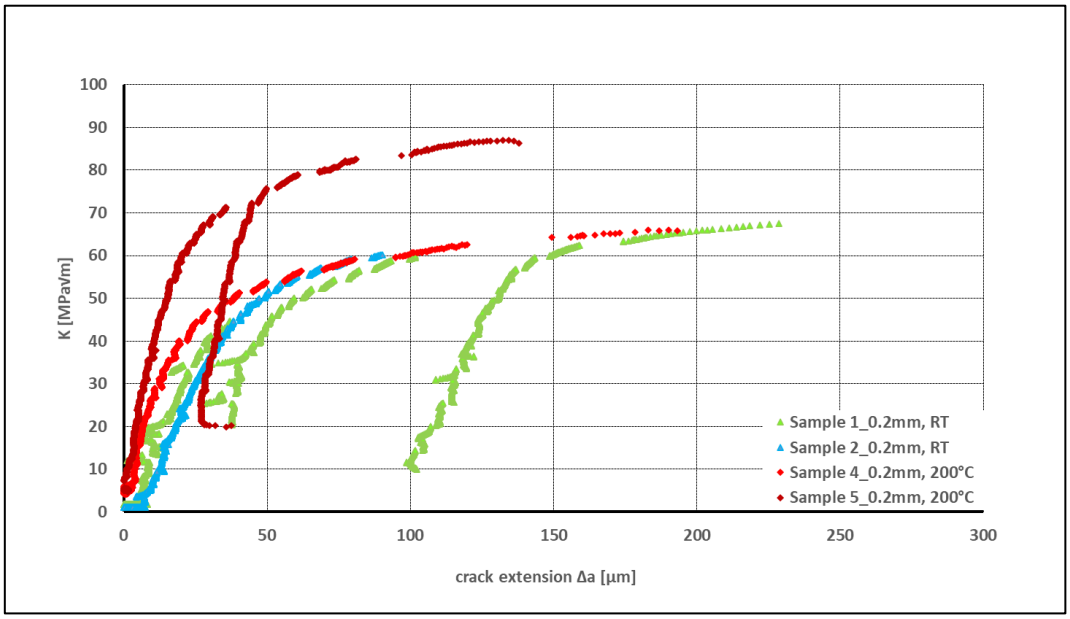

Figure 5.27: Presentation of the R-curves obtained, given for all samples of the 0.2 mm material.

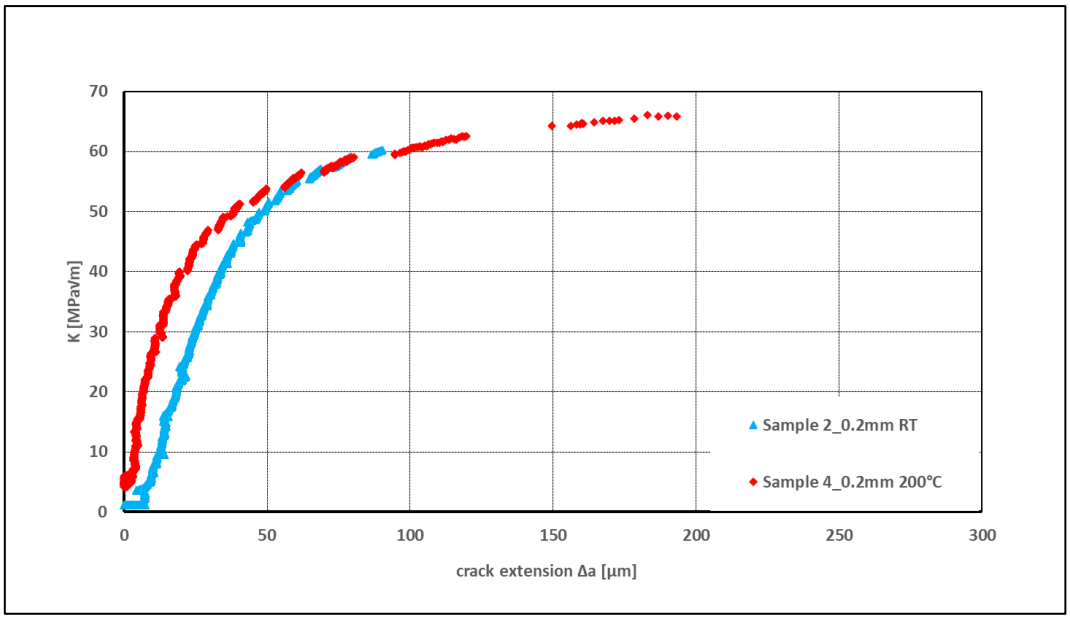

Figure 5.28: Presentation of the R-curves obtained, given for selected samples of the 0.2 mm material.

5.2.5. Results for the 0.1 mm samples

The 0.1 mm samples were tested along the lines of the 0.2 mm samples. The samples were soldered into steel sample holders, the current was applied through Ni-wires, the sample width W was 5 mm, and the nominal sample thickness B was 0.10 mm. In Table 5.6 all testing parameters, all data achieved and the corresponding testing results are listed.

Table 5.6: Testing parameters and data acquired for the 0.1 mm samples tested.

Sample	T [°C]	v [µm/min]	2λ [mm]	B [mm]	a [mm]	P [N]	Δa [µm]	Kq [MPa√m]
1_0.1mm	RT	200	2.4	0.10	1.101	302	297	50.5
3_0.1mm	RT	200	3.4	0.10	1.079	364	206	59.7
4_0.1mm	200	200	2.0	0.10	1.287	307	352	59.4
5_0.1mm	200	200	3.0	0.10	1.044	333	402	53.1

Independently of the testing temperature all 0.1 mm samples exhibited an R-curve behaviour and all the corresponding fracture surfaces were characterized by delamination over the whole fracture surface (figures 5.29 – 5.32). The fracture surface of each sample tested of the 0.1 mm material shows areas of delamination (figures 5.29d, 5.30c, 5.31c,d, 5.32a), the least pronounced in sample 3_0.1 mm and 5_0.1 mm. In these fracture surfaces cracks can be seen starting from the EDM notch, progressing through the FIB pre-crack, and ending in a region of very pronounced delamination. A pre-existing failure in the sample which expanded during the loading process could be the cause of this. It is possible as well that the samples were damaged during the preparation process (e.g. pre damaged due to delamination formation during the EDM cutting process, or a load too high applied to the sample during the notch refining step with the razor blade).

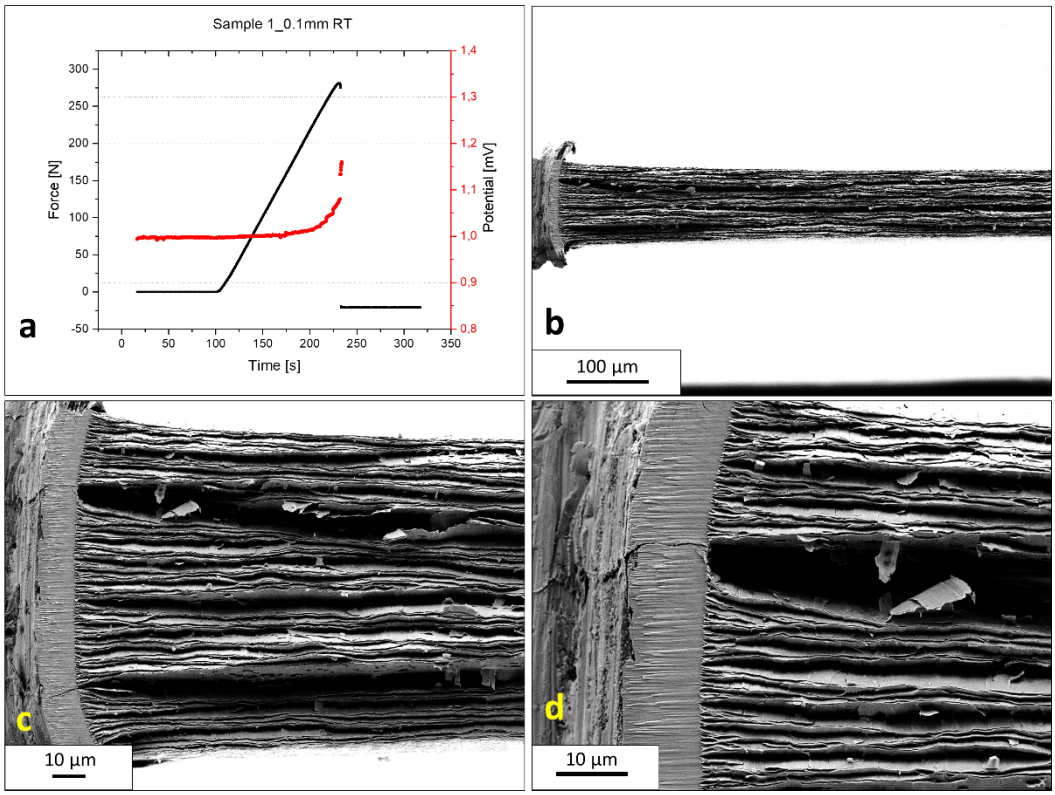

Figure 5.29: a) Load-potential curve of sample 1_0.1 mm tested RT with 200 µm/min; b) fracture surface overview, delaminaton; c) starting crack fracture surface, big gap, maybe due to pre-damaging the sample; d) more detailied view on the starting crack.

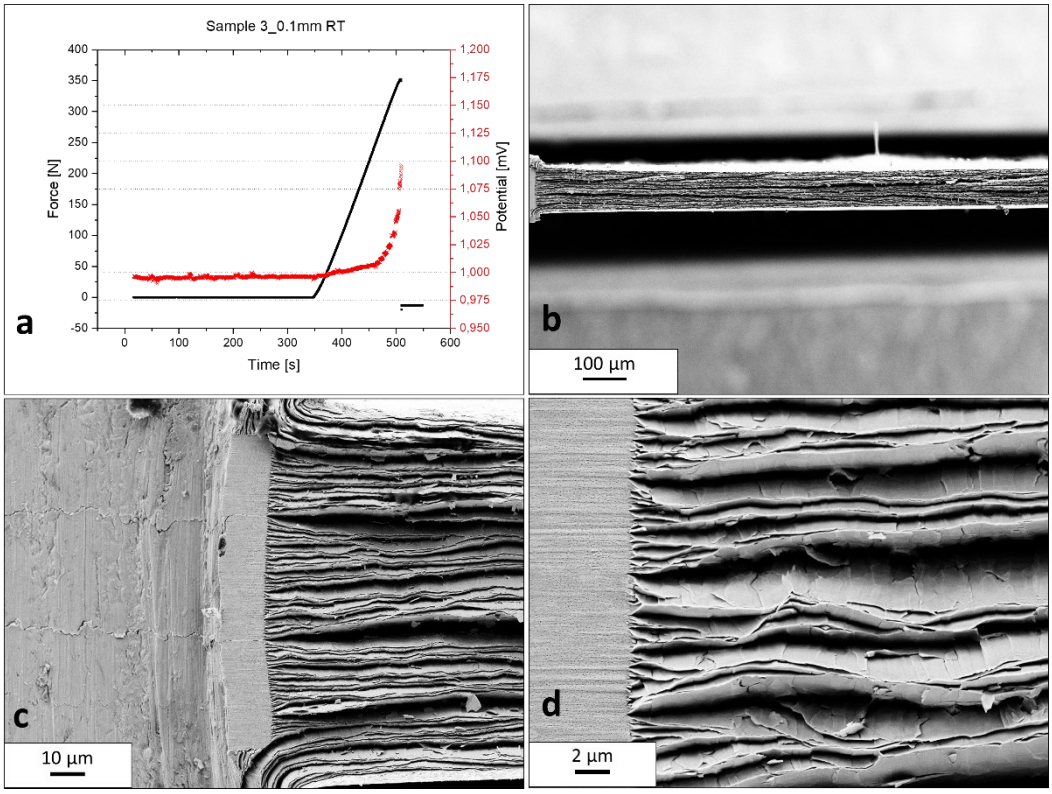

Figure 5.30: a) Load-potential curve of sample 3_0.1 mm tested at RT with 200 µm/min; b) fracture surface overview, delamination; c) starting crack fracture surface, again crack already starting in the pre-notch area through the whole sample; d) more detailied view on the starting crack.

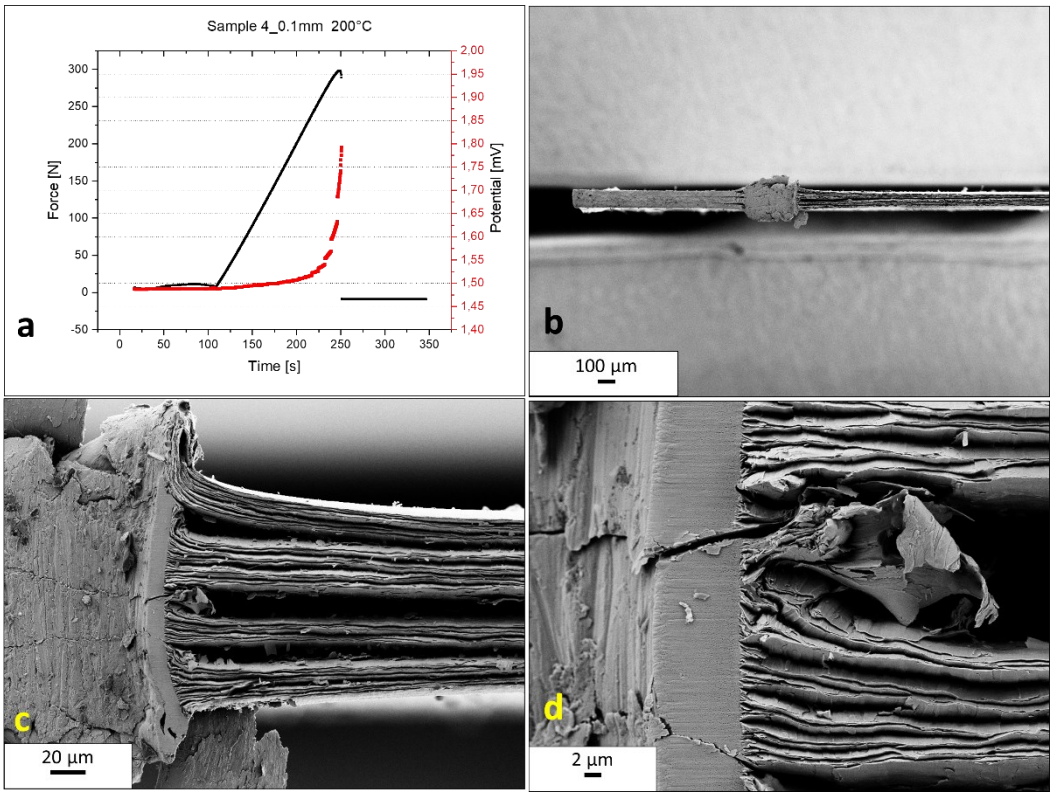

Figure 5.31: a) Load-potential curve of sample 4_0.1 mm tested at 200 °C with 200 µm/min; b) fracture surface overview, delamination; c) starting crack, again cracks can be seen in the pre-crack area, progressing through the notch and ending in large voids; d) more detailied view on one of these cracks.

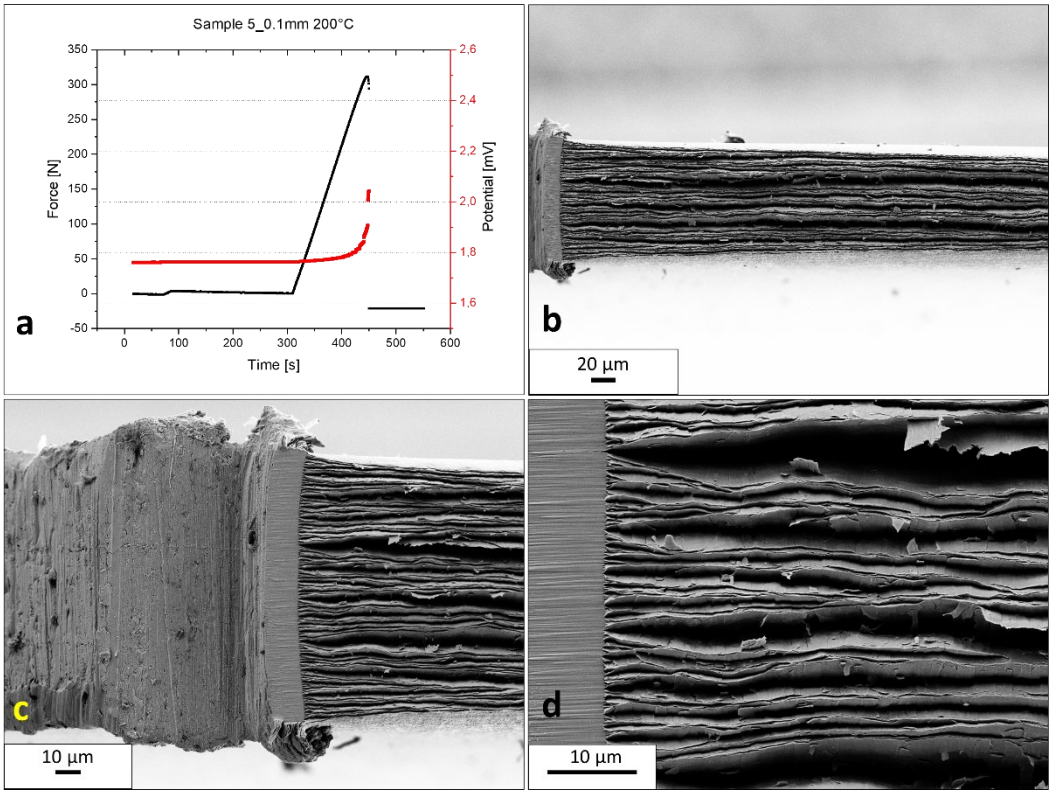

Figure 5.32: a) Load-potential curve of sample 5_0.1 mm tested at 200 °C and with 200 µm/min; b) fracture surface overview, delamination; c) starting crack fracture surface; d) more detailied view on the starting crack.

Figure 5.33 provides a summary of all R-curves obtained from 0.1 mm samples. Like the 0.2 mm samples, the 0.1 mm samples showed a significant crack extension, resulting in a pronounced R-curve even at RT.

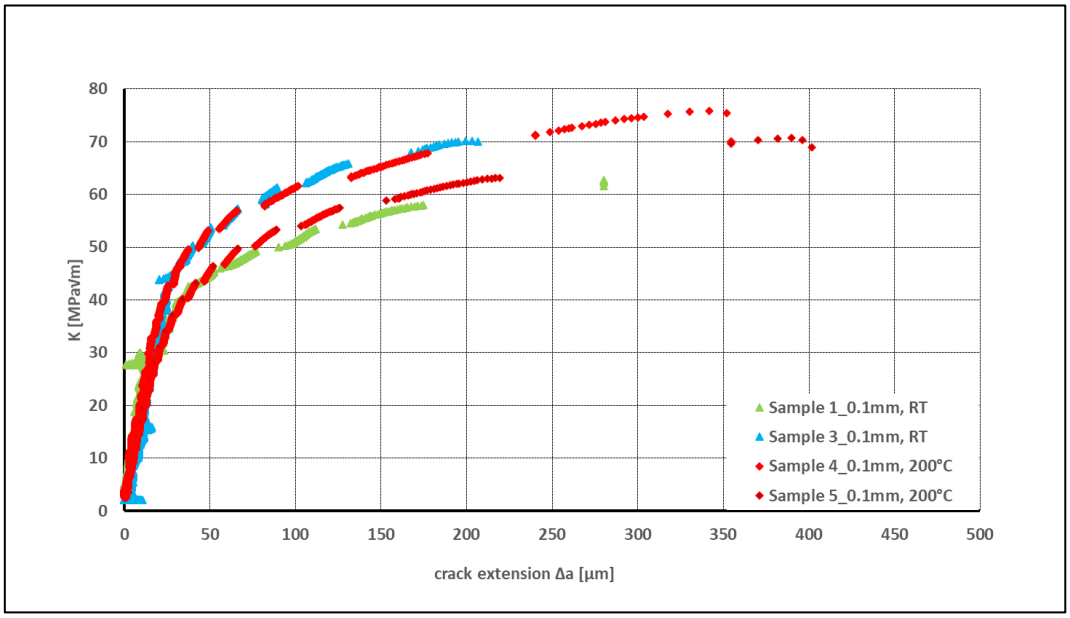

Figure 5.33: Presentation of the R-curves obtained, given for all samples of the 0.1 mm material tested.

5.2.6. Comparison of fracture and R-curve behaviour

To summarize the results of the fracture toughness and R-curve experiments, the two figures 5.34 and 5.35 for RT and for 200°C, respectively, display the development of the R-curve behaviour with regard to the thickness of the samples tested. For reason of clarity, only three materials and only one sample per material are represented in the graphs. There is a clear tendency regarding R-curve behaviour, ranging from showing no R-curve at all for the 2 mm material, a slight indication of an R-curve for the 0.5 mm, and up to a pronounced R-curve behaviour for the 0.1 mm material at RT.

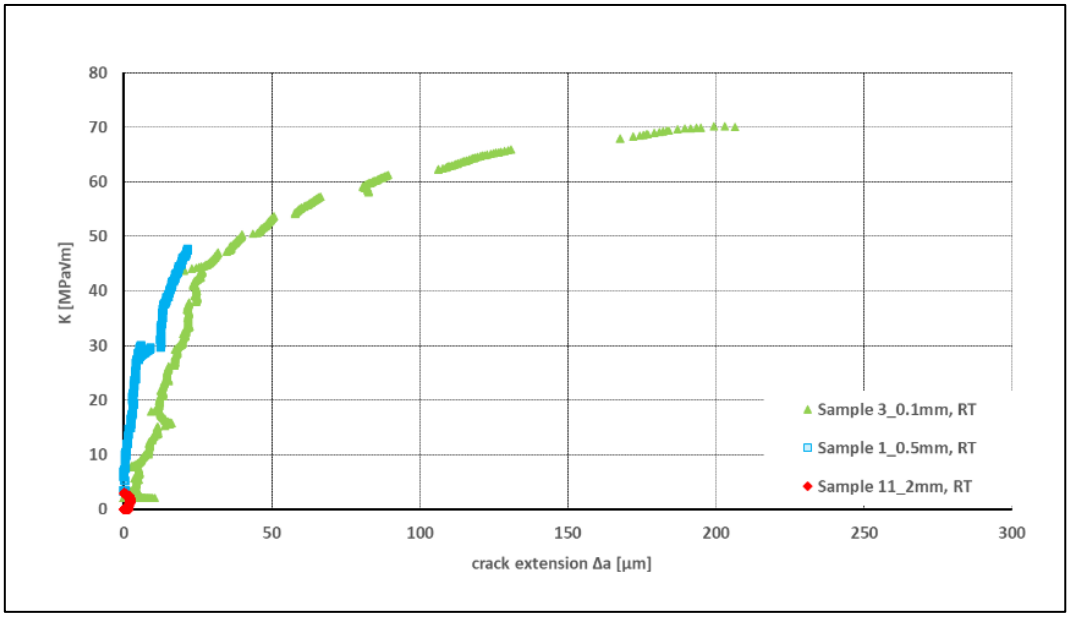

5.34: R-curve summary, displaying R-curves for selected samples at RT, featuring sample thicknesses from 0.1mm up to 2mm.

At a testing temperature of 200 °C all the materials even including the 2 mm material exhibited an R-curve behaviour, see figure 5.35.

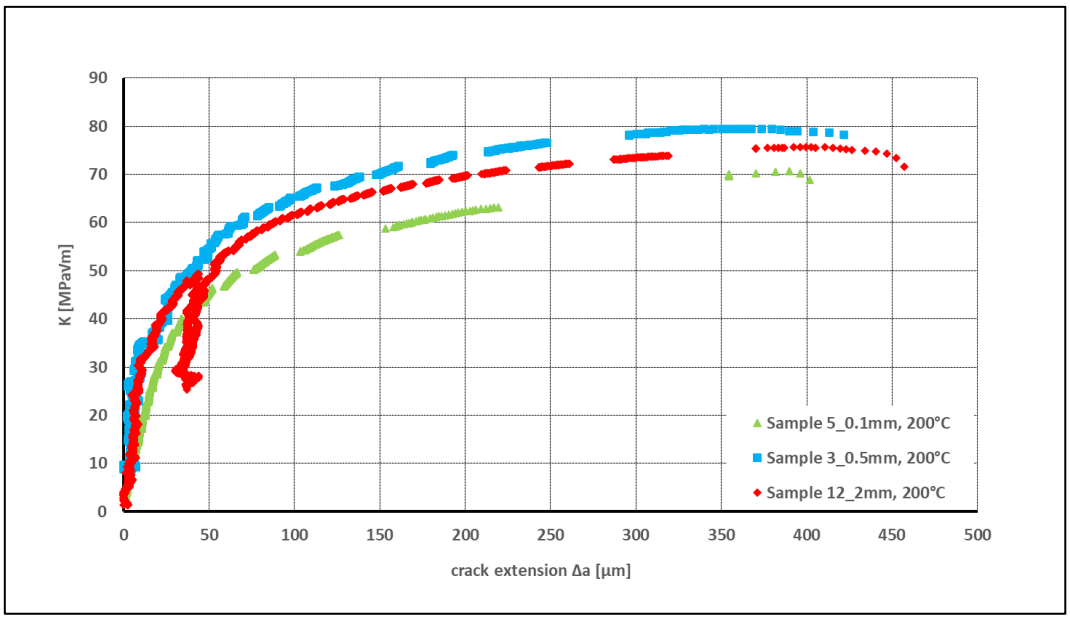

Figure 5.35: R-curve summary, displaying R-curves for selected samples at 200°C, featuring sample thicknesses from 0.1mm up to 2mm. The drop in the R-curve for sample 12_2 mm is caused by both bolts breaking during the experiment.

In the figures 5.36 and 5.37 the development of the conditional fracture toughness K_q and the crack growth Δa according to material thickness are presented. Important to note, the width W of the samples was halved from 10mm to 5 mm for the 0.2 mm and 0.1 mm samples compared to the thicker materials tested. This is important for comparison of crack lengths. A slight increase in fracture toughness K_q with decreasing sample thickness B was observed at RT and at 200 °C as well. A clear tendency of increased crack extension Δa with decreasing sample thickness B was observed at RT. At 200 °C the 1 mm sample showed a serrated behaviour with the highest crack extension of all materials. The 0.2 mm and 0.1 mm samples at 200 °C featured a similar trend as exhibited at RT. For a more precise statement more testing would be required.

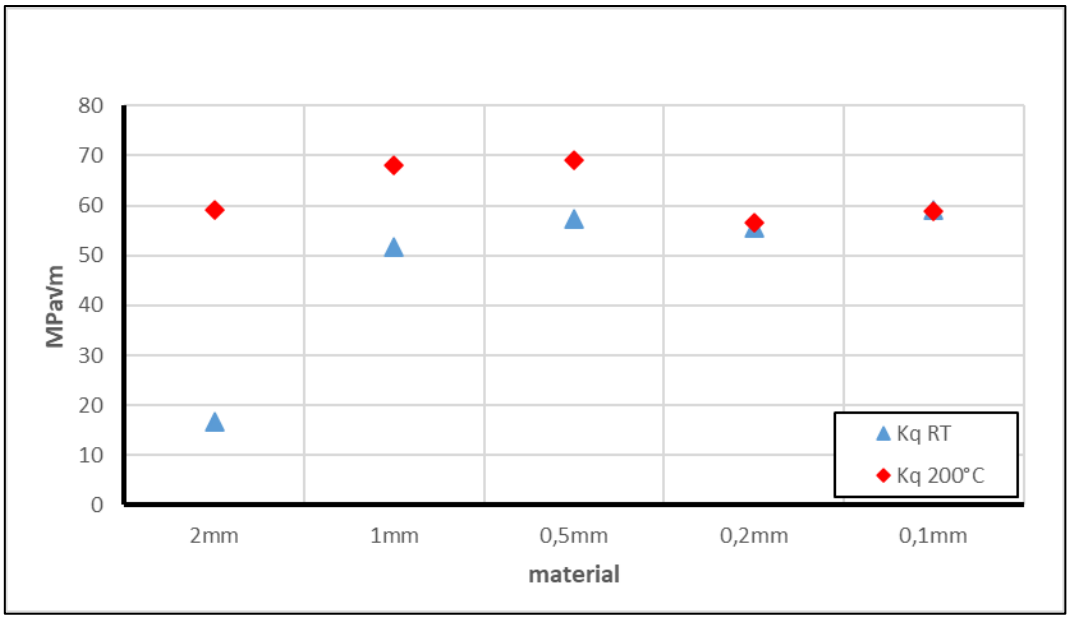

Figure 5.36: Development of the conditional fracture toughness K_q at RT and 200 °C, given as a function of material thickness.

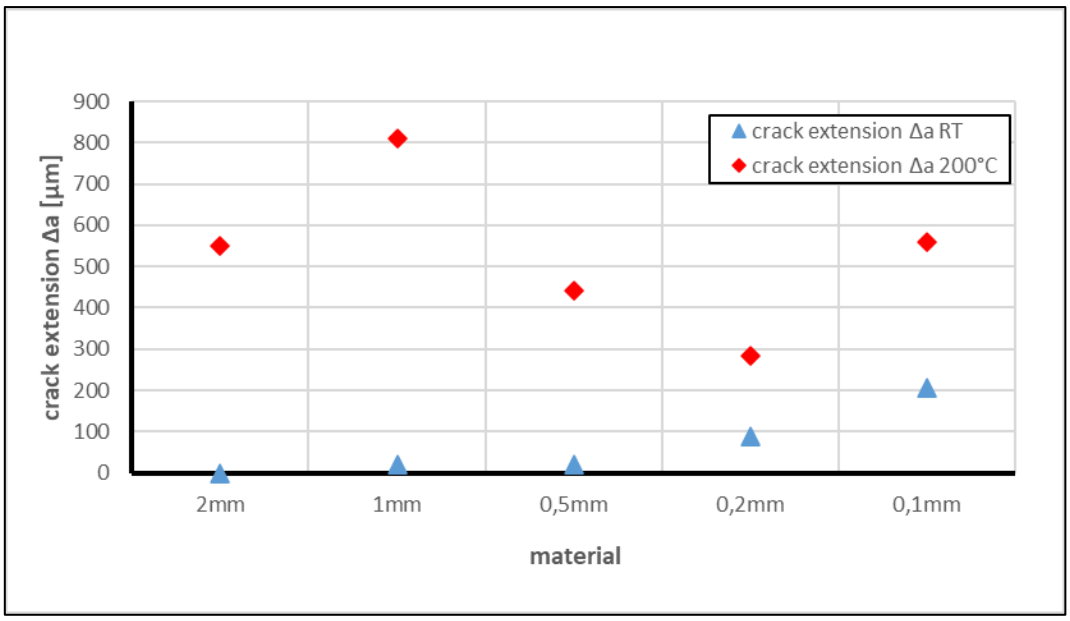

Figure 5.37: Development of the crack extension Δa at RT and 200 °C given as a function of material thickness.

The purpose of this thesis has been to investigate the influence of the microstructure on the fracture toughness and the R-curve behaviour. In order to get a clearer picture, definitely more samples need to be tested. Nevertheless, the trend of improved fracture behaviour with decreasing sample thickness – which goes hand in hand with a refined microstructure – is evident. For a convincing statistic or reliable values for both the conditional fracture toughness and crack extension more tests are required, especially tests with the same sample geometry.

5.3. Interrupted R-curve tests (fractography LN tests)

For the LN tests one sample of the 1 mm and the 0.5 mm material, was loaded at 200 °C to approximately 80 % to 90 % of the estimated fracture toughness. For the thinner materials (i.e. the 0.2 mm and the 0.1 mm material) the loading took place at RT, due both materials already exhibiting delamination at RT. When reaching the target load the test was stopped, the sample was cooled down and removed from the experimental set-up. Subsequently, the samples were broken in LN and the fracture surfaces were examined in the SEM. In the images (figure 5.38 – 5.41) given below, the fracture surfaces of the LN tests are presented for the 1 mm, the 0.5 mm, the 0.2 mm, and the 0.1 mm material. In all samples a small region of delamination can be seen, which originates for the thicker samples from the crack growth at 200 °. The adjacent fracture surface exhibits brittle fracture and large cracks ranging from the pre-crack deep into the brittle fracture area, resulting from the fracture in LN.

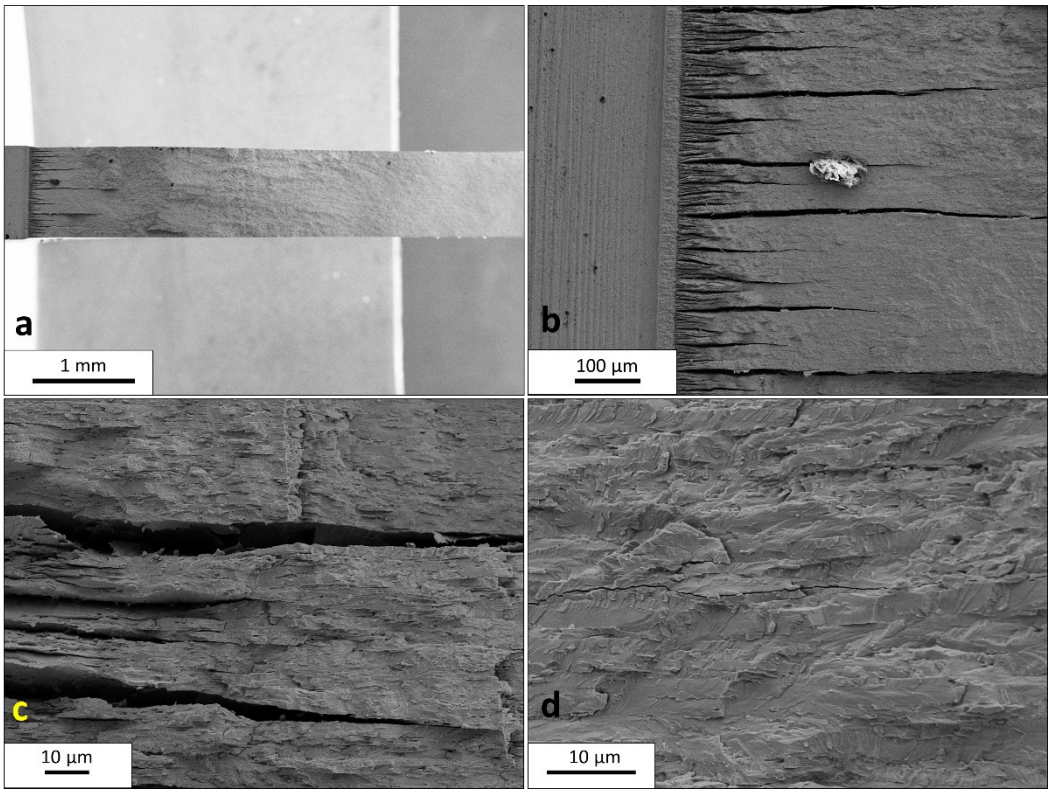

Figure 5.38: Fracture surfaces of a 1 mm sample loaded at 200 °C to K = 55 MPa√m and broken in LN.

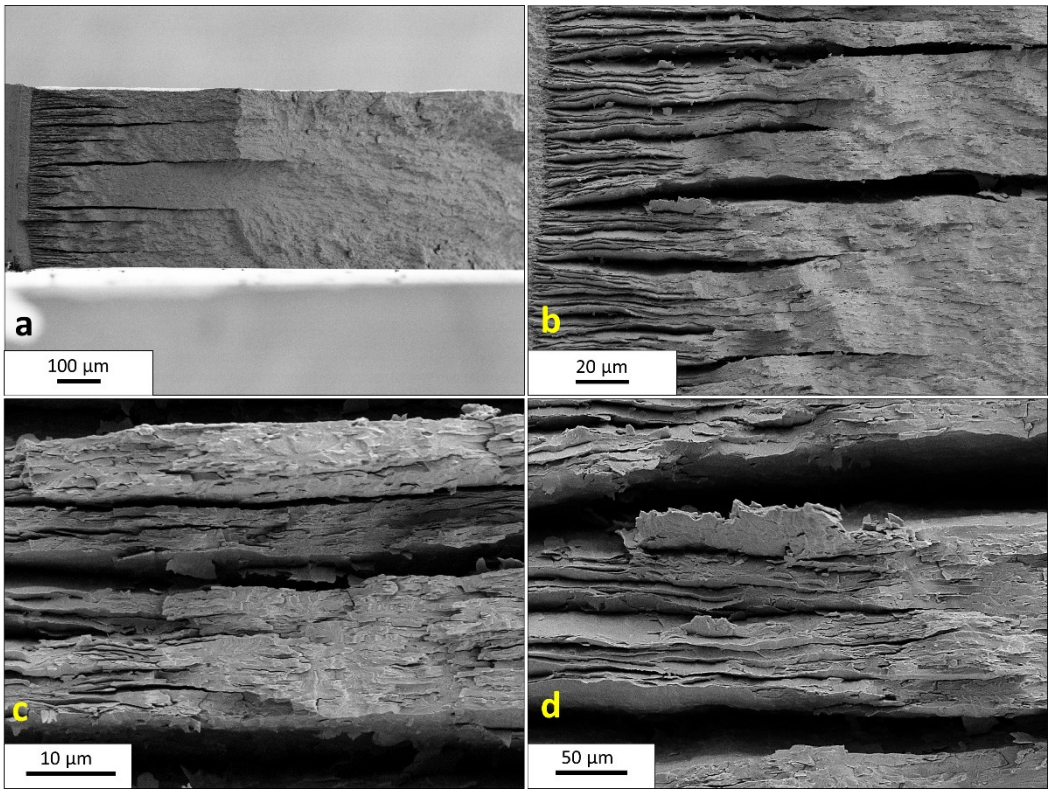

Figure 5.39: Fracture surfaces of a 0.5 mm sample loaded at 200 °C to K = 59 MPa√m and broken in LN.

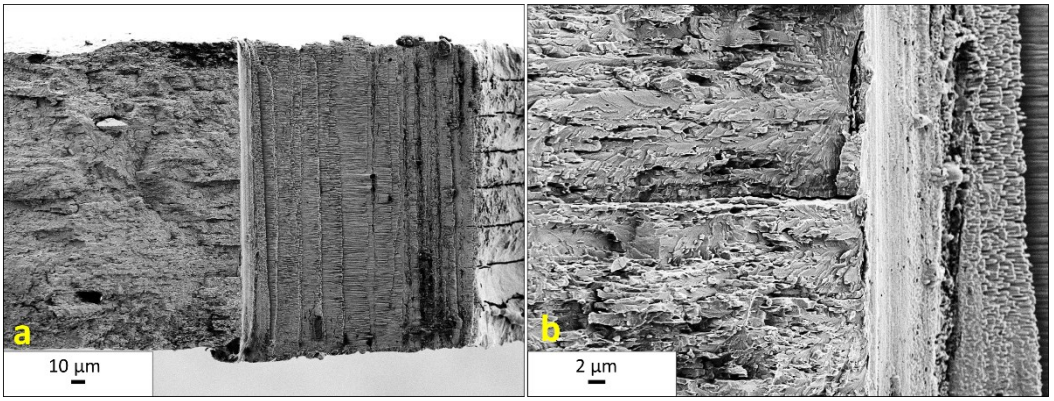

Figure 5.40: Fracture surfaces of a 0.2 mm sample loaded at RT to K = 41 MPa√m and broken in LN.

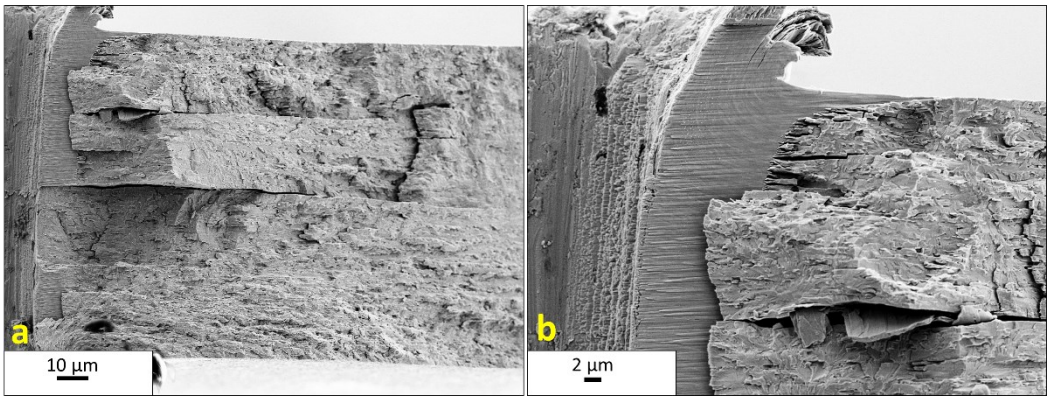

Figure 5.41: Fracture surfaces of a 0.1 mm sample loaded at RT to K = 42 MPa√m and broken in LN.

The 0.1 mm and 0.2 mm samples hardly show any delamination. This could be due to the force applied (80 % - 90 % of expected maximum force) being too low to induce crack growth. As can be seen in the load-potential curves in figures 5.32a, 5.31a, 5.30a, 5.29a, the increase in potential just before the moment of fracture is rather steep, and the delaminations evolve rather quickly. In case the force corresponding to this steep rise was missed by some ten newtons, hardly any delaminations have been seen.

6. Conclusion

The goal of this thesis was to investigate the influence of the microstructure on the fracture toughness and the R-curve behaviour of the fracture toughness. The respective microstructural features like grain size, grain orientation and texture were analysed by means of EBSD. The influence of the microstructure was investigated by measuring the fracture toughness and using the DCPM to determine the crack extension occurring. A pronounced, rising R-curve indicates stable crack growth and characterizes ductile fracture has occurred within the sample tested. Cause of a stable crack growth are dislocation movement and other toughening mechanisms (extrinsic toughening) like zone shielding or crack bridging.

Due to the thickness of the materials examined varying from plate (2 mm) down to a thin foil (0.1 mm) development of a suitable experimental set-up was required, which was able to deliver reliable results alike for all thicknesses. Moreover, procedures to prepare and wire the different samples had to be developed and optimized. The sample geometry chosen at first for the samples turned out not to be applicable for tests on the thinner samples, so the geometry of the samples tested had to be changed for the thinner materials. In order to be able at all to record the crack extension of quickly growing cracks the requirements regarding the loading rate given by the ASTM E399 were neglected and much lower loading rates were chosen. Because of the loading rates being too low, and as well because of restrictions due to sample size and insufficient sample thickness of materials examined, the requirements according to the ASTM E399 [19] for a valid fracture toughness test were not met and consequently all fracture toughness results achieved in this thesis are not to be specified as the fracture toughness K_{IC} but as conditional fracture toughness Kq for the respected sample thickness.

The results gathered indicate that a high degree of deformation achieved by rolling led to a microstructure beneficial regarding the fracture behaviour. In the course of rolling the grains form elongated pancake like shapes which are the cause of the delamination toughening. Source of delamination are the weak grain boundaries between the elongated grains.

In the course of testing materials of thicknesses diminishing and therefore of more refined microstructure, the fracture mechanisms changed from brittle fracture to ductile fracture by means of delamination. Due to this delamination the sample is split into a stack of several thinner samples, which leads to a major change in the stress state in front of the crack from plane strain to plane stress, which results in an increase of the fracture toughness. The tests with pre-cracking at 200 °C and final fracture in LN showed that the crack extension and delamination take place pretty close to the maximum of the bearable load, therefore no pronounced crack extension during the delamination could be detected in the 80 % tests.

To summarize a few of the observations obtained:
In figure 5.34 the influence of the microstructure on the R-curve behaviour of W can be recognized quite well. At RT the 2 mm material, the material with the least degree of deformation and the least pronounced texture examined, did not exhibit an R-curve behaviour. With the thickness of the materials decreasing, the samples exhibited an increasing degree of deformation and consequently a more pronounced texture and grain refinement. Concordant to this trend the 0.5 mm sample first of all samples tested at RT exhibited an R-curve behaviour. For all samples thinner than 0.5 mm pronounced R-curves could be obtained. Furthermore, the refinement of the microstructure shifted the DBTT from approximately 200°C for the 2 mm samples to ambient temperatures for the 0.5 mm samples. Due to the DBTT being close to the testing temperature (RT) an influence of the loading speed on fracture toughness and R-curve behaviour could be observed. Figure 5.22 presents the R-curves of the three 0.5 mm samples tested. The sample tested at RT at high testing speed (200 µm/min) barely exhibited any progress in crack extension, while the sample tested at low speed (20 µm/min) offered a crack extension four times longer approximately. The corresponding change in fracture mechanism can be recognized in the fracture surfaces (figures 5.18 and 5.19). In the 200 °C experiments all materials exhibited an R-curve behaviour, no dependency of the conditional fracture toughness Kq on the sample thickness was to be observed, this as well holding for the crack extension Δa observed.

For more detailed statements or conclusions clearly more tests are required, especially more tests with sample dimensions identical for all materials. It is still up for discussion and further

experiments whether the improved mechanical properties of the thinner materials tested in this thesis are merely a result of the improved microstructure, or whether other effects have to be considered too. Further experiments probably should include taking e.g. a 1 mm material, grind it down to a sheet of 0.5 mm or even thinner, and then perform the experiments described in this thesis on this sheet obtained. This would give some insight whether the improved mechanical properties are an effect of the improved microstructure or whether they are an effect of the sample thickness. Thinner samples have a higher proportion of the sample under plane strain conditions, resulting in a higher fracture toughness.

7. Literature

[1] Lassner E and Schubert W-D 1999 *Tungsten-Properties, Chemistry, Technology of the Element, Allyos and Chemical Compounds* (Vienna, Austria: Springer Science+Business Media, LLC)

[2] Rau G and Ströbel R 1999 *Die Metalle: Werkstoffkunde mit ihren chemischen und physikalischen Grundlagen* (Verlag Neuer Merkur GmbH)

[3] Hartmaier A and Gumbsch P 2005 Thermal activation of crack-tip plasticity: The brittle or ductile response of a stationary crack loaded to failure *Phys. Rev. B* **71** 024108

[4] Rieth M, Dudarev S L, Gonzalez de Vicente S M, Aktaa J, Ahlgren T, Antusch S, Armstrong D E J, Balden M, Baluc N, Barthe M-F, Basuki W W, Battabyal M, Becquart C S, Blagoeva D, Boldyryeva H, Brinkmann J, Celino M, Ciupinski L, Correia J B, De Backer A, Domain C, Gaganidze E, García-Rosales C, Gibson J, Gilbert M R, Giusepponi S, Gludovatz B, Greuner H, Heinola K, Höschen T, Hoffmann A, Holstein N, Koch F, Krauss W, Li H, Lindig S, Linke J, Linsmeier Ch, López-Ruiz P, Maier H, Matejicek J, Mishra T P, Muhammed M, Muñoz A, Muzyk M, Nordlund K, Nguyen-Manh D, Opschoor J, Ordás N, Palacios T, Pintsuk G, Pippan R, Reiser J, Riesch J, Roberts S G, Romaner L, Rosiński M, Sanchez M, Schulmeyer W, Traxler H, Ureña A, van der Laan J G, Veleva L, Wahlberg S, Walter M, Weber T, Weitkamp T, Wurster S, Yar M A, You J H and Zivelonghi A 2013 Recent progress in research on tungsten materials for nuclear fusion applications in Europe *Journal of Nuclear Materials* **432** 482–500

[5] Reiser J, Rieth M, Möslang A, Dafferner B, Hoffmann J, Mrotzek T, Hoffmann A, Armstrong D E J and Yi X 2013 Tungsten foil laminate for structural divertor applications – Joining of tungsten foils *Journal of Nuclear Materials* **436** 47–55

[6] Jasper B, Coenen J W, Riesch J, Höschen T, Bram M and Linsmeier C 2015 Powder Metallurgical Tungsten Fiber-Reinforced Tungsten *MSF* **825–826** 125–33

[7] Reiser J, Garrison L, Greuner H, Hoffmann J, Weingärtner T, Jäntsch U, Klimenkov M, Franke P, Bonk S, Bonnekoh C, Sickinger S, Baumgärtner S, Bolich D, Hoffmann M, Ziegler R, Konrad J, Hohe J, Hoffmann A, Mrotzek T, Seiss M, Rieth M and Möslang A 2017 Ductilisation of tungsten (W): Tungsten laminated composites *International Journal of Refractory Metals and Hard Materials* **69** 66–109

[8] Geach G A and Hughes J E 1955 The Alloys of Rhenium with Molybdenum or with Tungsten and Having Good High Temperature Properties *Proceedings of the 2nd Plansee Seminar, Reutte (1955)*

[9] Wurster S, Gludovatz B and Pippan R 2010 High temperature fracture experiments on tungsten–rhenium alloys *International Journal of Refractory Metals and Hard Materials* **28** 692–7

[10] Nikolić V, Wurster S, Firneis D and Pippan R 2018 Fracture toughness evaluation of UFG tungsten foil *International Journal of Refractory Metals and Hard Materials* **76** 214–25

[11] Bonk S, Reiser J, Hoffmann J and Hoffmann A 2016 Cold rolled tungsten (W) plates and foils: Evolution of the microstructure *International Journal of Refractory Metals and Hard Materials* **60** 92–8

[12] Bonk S, Hoffmann J, Hoffmann A and Reiser J 2018 Cold rolled tungsten (W) plates and foils: Evolution of the tensile properties and their indication towards deformation mechanisms *International Journal of Refractory Metals and Hard Materials* **70** 124–33

[13] Bonnekoh C, Hoffmann A and Reiser J 2018 The brittle-to-ductile transition in cold rolled tungsten: On the decrease of the brittle-to-ductile transition by 600 K to − 65 °C *International Journal of Refractory Metals and Hard Materials* **71** 181–9

[14] Kolednik O 2018 Vorlesungsskriptum WS 2018: Werkstoff und Bruchzähigkeit

[15] Anderson T L 2005 *Fracture mechanics: fundamentals and applications* (Boca Raton, FL: Taylor & Francis)

[16] Inglis C E 1913 Stresses in a plate due to the presence of cracks and sharp corners *Transactions of the Institute of Naval Architects* **55** 219–41

[17] Griffith A A 1920 The Phenomena of Rupture and Flow in Solids. *Philosophical Transactions* **S221** 163–98

[18] Irwin G R 1956 Onset of Fast Crack Propagation in High Strength Steel and Aluminum Alloys *Sagamore Research Conference Proceedings* vol 2 pp 289–305

[19] ASTM International 2013 *E399 - Test Method for Linear-Elastic Plane-Strain Fracture Toughness KIc of Metallic Materials*

[20] Gross D and Seelig T 2006 *Fracture mechanics: with an introduction to micromechanics* (Berlin ; New York: Springer)

[21] Gumbsch P 1998 Controlling Factors for the Brittle-to-Ductile Transition in Tungsten Single Crystals *Science* **282** 1293–5

[22] Johnson H H 1965 Calibrating the Electric Potential Method for Studying Slow Crack Growth *ASTM Materials Resarch and Standards* 442–5

[23] Ritchie R O 1999 Mechanisms of fatigue-crack propagation in ductile and brittle solids *International Journal of Fracture* **100** 55–83

[24] Ritchie R O 1988 Mechanisms of fatigue crack propagation in metals, ceramics and composites: Role of crack tip shielding *Materials Science and Engineering: A* **103** 15–28

[25] Schwarzer R 2018 Rückstreu-Kikuchi-Beugung im Raster-Elektronen-Mikroskop (“EBSD”, “BKD”, “ACOM/SEM”, “Orientation Microscopy”) *Rückstreu-Kikuchi-Beugung im Raster-Elektronen-Mikroskop (“EBSD”, “BKD”, “ACOM/SEM”, “Orientation Microscopy”)*

[26] Hohenwarter A, Wurster S and Kirchlechner C 2014 Vorlesungs Skriptum zu Metallkundliche Arbeitsverfahren

[27] Schwartz A J 2009 *Electron backscatter diffraction in materials science* (New York: Springer)

[28] Plansee SE 2015 PM-Mo/W Herstellungsweg

[29] Reiser J, Wurster S, Hoffmann J, Bonk S, Bonnekoh C, Kiener D, Pippan R, Hoffmann A and Rieth M 2016 Ductilisation of tungsten (W) through cold-rolling: R-curve behaviour *International Journal of Refractory Metals and Hard Materials* **58** 22–33

[30] Nikolić V, Wurster S, Firneis D and Pippan R 2016 Improved fracture behavior and microstructural characterization of thin tungsten foils *Nuclear Materials and Energy* **9** 181–8

[31] Gludovatz B 2010 Dissertation: *Fracture behavior of tungsten* (Leoben: Montanuniversität)

[32] Gludovatz B, Wurster S, Hoffmann A and Pippan R 2013 A study into the crack propagation resistance of pure tungsten *Engineering Fracture Mechanics* **100** 76–85

[33] Murakami Y 1987 *Stress intensity factors handbook* (Oxford [Oxfordshire] ; New York: Pergamon)

[34] Pippan R 1987 The Growth of Short Cracks Under Cyclic Compression *Fatigue & Fracture of Engineering Materials & Structures* **9** 319–28

[35] ASM International 2000 Ni-W Phasediagram ASM Handbook Volume 8: Mechanical Testing and Evaluation

[36] Anon Keithley 2182A Nanovoltmeter | TestEquity | 2182A Data Sheet 2019

[37] Cravero S and Ruggieri C 2007 Estimation procedure of J-resistance curves for SE(T) fracture specimens using unloading compliance *Engineering Fracture Mechanics* **74** 2735–57